GEOLOGICA ULTRAIECTINA

Mededelingen van de
Faculteit Geowetenschappen
Universiteit Utrecht

No. 284

Dynamics of subduction and continental collision: Influence of the nature of the plate contact

Roberta De Franco

Dynamics of subduction and continental collision: Influence of the nature of the plate contact

Dynamica van subductie en continentale collisie: Invloed van het karakter van het plaat-contact

(met een samenvatting in het Nederlands)

PROEFSCHRIFT

TER VERKRIJGING VAN DE GRAAD VAN DOCTOR
AAN DE UNIVERSITEIT UTRECHT
OP GEZAG VAN DE RECTOR MAGNIFICUS, PROF. DR. J. C. STOOF,
INGEVOLGE HET BESLUIT VAN HET COLLEGE VOOR PROMOTIES
IN HET OPENBAAR TE VERDEDIGEN
OP MAANDAG 4 FEBRUARI 2008 DES OCHTENDS TE 10.30 UUR

DOOR

Roberta De Franco

GEBOREN OP 24 NOVEMBER 1976, TE VERONA, ITALIE

Promotor: Prof. dr. M. J. R. Wortel
Co-promotor: Dr. R. Govers

This thesis was partially accomplished with financial support of the Netherlands Research Centre for Integrated Solid Earth Science (ISES).

ISBN/EAN: 978-90-5744-149-3

Contents

Chapter 1

Introduction

1.1 Motivation

Subduction zones are regions where convergence of lithospheric plates is accommodated. One plate, generally oceanic, slides underneath the other and moves downwards into the mantle, at rates on the order of a few centimeters per year. The cumulative length of these convergent margins is greater than 55.000 km and they represent the most active areas of our planet. From a global perspective subduction processes are characterized by common features such as a trench, a forebulge, a foredeep, a volcanic arc and an inclined array of earthquakes known as the Wadati-Benioff zone. However, their behavior might vary from site to site (e.g. different convergence velocity, intensity and frequency of earthquakes, geometry and age of the slab, sediment supply, state of stress in the back-arc region). Understanding the mechanics and dynamics of the subduction process in the light of these observed features represents a major challenge.

Since the advent of plate tectonics, scientists tried to understand the causes of similarities and differences characterizing subduction zones. Through analysis of surface observables, interpretation of seismic information and numerical experiments, there have been many attempts to classify subduction zones to have a general understanding of the process (e.g., Uyeda & Kanamori, 1979; Royden, 1993; Cloos & Shreve, 1996). One of the challenges was (and still is) to correctly establish the link between surface observations and dynamics of subduction at great depth. Over the last decades some parameters have been identified as more important than others (e.g. the dip angle, the interaction of the slab with the 660 km discontinuity, the age of the slab), and often correlations between different observables have been established, even though the physical meaning of such correlations is only partially understood.

Tackley (2000) drew attention to the fact that, for the operation of plate tectonics,

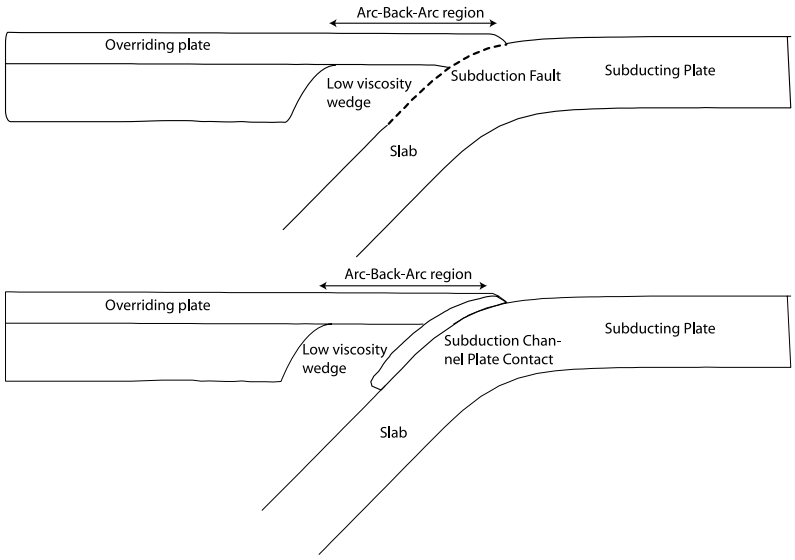

Figure 1.1: Top: Subduction zone with subduction fault plate contact (dashed line). Bottom: Subduction zone with channel plate contact.

a relatively low shear strength of the plate contact is a critical mechanical property. The effective friction at the plate contact has a first order effect on plate boundary topography and the plate-like motion (Zhong et al., 1998). On the scale of the entire lithosphere, quantitative models based on a single subduction fault have been used to investigate how the fault properties influence the stress distribution and plate boundary forces associated with subduction (Bott et al., 1989; Whittaker et al., 1992; Giunchi et al., 1996). However, several seismic investigations have shown the actual existence of inter-plate sedimentary channel-like units of about 1-8 km thickness (Eberhart-Phillips & Martin, 1999; Oncken et al., 2003; Abers, 2005; Tsuru et al., 2002). Through inversion of arrival times from local earthquakes, these scientists found a low velocity anomalous zone at the interface between the plates. The arrival-time inversion, however, can not resolve the thickness and the character of the layer independently. This means that a thick channel width a weak material fill can be equivalent to a thinner channel with a stronger velocity anomaly. Upon further decreasing channel with, a fault will represent the plate contact. As a consequence it is possible to identify two end members of plate contacts (see Fig. 1.1): a fault and a subduction channel, representing two different physical states of the subduction plate contact and characterized by different properties. A subduction plate contact may evolve from one state to another through a varying sediment supply. Along

strike variations in the physical state of the plate contact nature of a single subduction zone are also possible. Conder (2005) compared different parameterizations of the plate contact and concluded that formulations such as weak nodes (comparable to our subduction channel) at the plates interface or geometrically defined rigid plates (comparable to our fault model) produce similar results, but can still differ in important details. This study, however, does not point out the physical meaning of the two approaches. Since the properties of the actual plate contact are important for the overall dynamics it is fundamental to answer some questions concerning the actual role played by this parameter:
1) What is the influence of the two end members (fault vs. channel) on the general response of subduction zones?
2) What are the differences in surface effects caused by variation in plate contact nature and inversely, is it possible to link surface observations with the nature of the plate contact?
3) In the special case of continental collision following oceanic subduction, is the nature of the plate contact affecting the continental collision processes?
Answering these questions will contribute to a better understanding of subduction processes.

1.2 Continental subduction

Continental collision, following oceanic lithospheric subduction, is fundamental in connecting plate motion and orogenic events. Due to its thick and light crust, continental lithosphere is positively buoyant and resists subduction, whereas cold and dense subducted oceanic lithosphere results in a large downward force (slab pull). Consequently, most oceanic crust is subducted easily at an oceanic trench, whereas continental crust is subducted with difficulty, if at all.
In a subduction process, continental collision may progress in different ways. In nature, there is ample proof that continental crust may have been exposed to pressure of about 30-35 kbar. Ultra-high pressure metamorphic minerals (e.g., coesite, diamond) show that subducted continental crust may reach mantle depth and subsequently exhumes (e.g. Chopin, 2001; Smith, 1984; Liou et al., 2000; Yang et al., 2003).
The whole crust, or part of it, may separate from the lithospheric mantle and remain at the surface (Cloos, 1993; Kerr & Tarney, 2005; Vos et al., 2007). For instance in the Colorado Plateau (Bird, 1979), progressive separation of the lithospheric mantle from the buoyant continental crust has been proposed to explain its tectonic evolution. Another possibility is that the incoming continental material may lock the trench, possibly resulting in break-off of the slab if the slab is not sufficiently strong (Davies & von Blanckenburg, 1995; Wong A Tong & Wortel, 1997; Wortel & Spakman, 2000;

Boutelier et al., 2004; Faccenna et al., 2006).
Already some very early studies suggested that the gaps in seismic activity as a function of depth might be explained by the existence of detached slabs (Isacks & Molnar, 1971; Barazangi et al., 1973). Subsequently, seismic tomography provides strong evidence to recognize real gaps in slab structure (e.g., Spakman, 1990). In many regions, e.g. the Mediterranean-Carpathian region, the New Hebrides, Turkey, slab break-off (or detachment) has been used to explain the upper mantle structure and tectonic deformation (Chatelain et al., 1992; Wortel & Spakman, 1992, 2000; Parlak et al., 2006; Lei & Zhao, 2007). Understanding the factors controlling the three different modes of continental collision is important for unraveling the tectonic evolution of convergent plate boundary regimes. During the initial phase of this process, the geometry and the strength of the incoming continental sliver and the property of the plate contact may represent discriminating factors. While the role of buoyancy, rheology and subduction rate during continental collision have been largely investigated (van den Beukel, 1992; Davies & von Blanckenburg, 1995; Wong A Tong & Wortel, 1997; Sobouti & Arkani-Hamed, 2002; Ranalli et al., 2000; Toussaint et al., 2004), the function played by the geometry (in combination with the strength) of the incoming continental sliver and by the property of the plate contact is still unknown.

1.3 Erosive and accretionary convergent margins

Convergent margins are part of one of two categories, accretionary or erosive margins. Soon after the development of the plate tectonic theory, it was recognized that some margins have with thick sequences of oceanic and trench rocks that have been off-scraped from the subducting plate during convergence (e.g., Seely et al., 1974; Hamilton, 1969; Karig & Sharman, 1975). Contemporaneously it was discovered that at other margins the sediments were subducted along with fragments of the crust removed from the overriding plate (e.g., Scholl et al., 1977; Hilde, 1983).
In the 80s and 90s, seismic surveying, the Deep Sea Drilling Project (DSDP) and the Ocean Drilling Program (ODP), showed that sediment accretion was just one of the processes characterizing convergent margins. Von Huene & Lallemand (1990) revealed that the land-ward retreat of the Peru and the Japan trenches was caused by tectonic erosion of the overriding plate. Hilde (1983) explained erosion as a consequence of abrasion of the upper plate due to horsts. Lallemand et al. (1994) classified erosion in two types, frontal and basal tectonic erosion. The former takes place near the trench and is due to the subduction of oceanic features within grabens or close to ridges and seamounts. The latter occurs at the base of the overriding plate and might be due to a fast convergence rate that results in hydrofracturing of the base of the upper plate material by overpressuring. In general accretion appears to occur where the

thickness of the sediment layer at the trench exceeds 500 m to 1 km and it is favored at low subduction rate. Subduction erosion is defined as the process that causes a net loss of material from the hanging wall.
Since the nature of the converging margin (erosive or accretionary) influences the amount of sediment present at the plate contact, it is an important problem to understand its relation with the nature of the plate contact itself. One of the aims of this thesis is to find differences and similarities between these two main categories and to relate them to the nature of the plate contact.

1.4 Modeling

By repeated observations, we establish regularities which are included in models (numerical and analytical). This is a process which generates models of increasing generality and power. It is important pointing out that a model can be general and sophisticated, but it is never real. A model that is ”perfect” in the sense of being identical to the real natural phenomena will be of limited use. It will obscure the insights that a simple but effective model can often provide. Models must therefore be simple and clear. However, models must not be simpler than they have to be. It therefore follows that a task equally important as the development of a model is the identification of its limitations, in a qualitative and, if possible, quantitative way.
In this thesis, we use numerical modeling to investigate some aspects of the subduction process and to interpret geophysical and geological data. Surface data are used a posteriori (chapter 5) to determine whether the concept that is the basis of the numerical model pertains to specific regions or not. The finite element code (G-Tecton) used for this study is a further development of the original version by Melosh & Raefsky (1980) made by Govers & Wortel (1993, 1995) and Buiter et al. (2001).

1.5 Thesis outline

Chapter 2 represents a technical part of the thesis, in which I give a back-ground on the theory of the numerical remeshing procedure implemented for this study. To test the validity of the method, experiments concerning the sedimentation of a cylinder are shown. This chapter includes **Appendix A** that provides a simple introduction to the finite element method.
To address the considerations and questions discussed in the previous sections, I first (**Chapter 3**) study the influence of the nature of the plate contact on the response of oceanic subduction processes. I determine the specific signatures of both states of subduction zones plate contact, i.e., a subduction fault and a subduction channel.

Through numerical modeling I evaluate overriding plate velocities, stress field in the back-arc region and topography for both types. By using a single finite element program for both types of models, the results are internally consistent and, therefore, well suited for comparison. This chapter includes two appendixes: **Appendix B** extends the results to the land-locked basin setting; **Appendix C** provides the finite element equations for diffusion-advection equation.

In **Chapter 4**, I further expand the idea developed in Chapter 3, by investigating the effect of the different nature of the plate contact when a continental terrane arrives at the trench and collides with a continental plate. **Appendix D** extends the results given in this chapter to the land-locked basin setting.

In the last part of the thesis (**Chapter 5**), I present a new global classification of subduction zones using observed back arc strain, nature of the convergent margin (erosive or accretionary) and maximum seismic moment magnitude. We shed new light on the geodynamics of subduction, based on the physical insights from our previous numerical experiments in combination with a re-analysis of published observations. We highlight the nature of the plate contact as an important physical feature of subduction zones and find that it is significantly correlated to the back-arc state of stress/strain as well as to the maximum seismic moment magnitude.

Chapters 3, 4 and 5 and their appendixes are structured as (published) papers or (submitted) manuscripts.

Chapter 2

The remeshing procedure

In this chapter we present a technique to solve the problem of large deformation of rock material. The method consists of updating the connectivity between the nodes of the mesh in order to replace the distorted mesh by a more regular one. Because it requires a Lagrangian method in which the numerical grid is advected with the deformation, this method is suited to track material boundaries and to represent free surface. To illustrate the validity of the method, we will show the experiment of sedimentation of a cylinder in a viscoelastic material.

2.1 Introduction

In the finite element method (FEM) (see Appendix A) two equivalent approaches are used: the Eulerian, where finite element equations are solved in a fixed reference system, and the Lagrangian, in which the reference system is attached to the flowing material particles. When the material deforms, the mesh deforms accordingly.
The Eulerian approach, where the grid does not deform, is used to solve fluid problems in which deformations are big and well characterized by velocity vectors.This method has many disadvantages:
1) It is very difficult to analyze the time history of field variables at a fix point in the material, because the movement of the material cannot be tracked using a fixed mesh. One can have only the time history of field variables at a fixed-in-space Eulerian grid.
2) It is not so easy to treat the irregular and complicated geometries of a medium.
3) Since the Eulerian methods track the mass, momentum and energy flux across the mesh cell boundaries, the position of free surfaces, deformable boundaries and moving material interfaces are difficult to be determined accurately.
Our finite element code is based on a Lagrangian approach. Since each node follows the path of the material at the grid point, the relative movement of the connecting

nodes may result in expansion, compression and deformation of a mesh cell. Mass, momentum and energy are transported with the movement of the elements. Because the mass within each element remains fixed, no mass flux crosses the element boundaries. The Lagrangian methods have several advantages:
1) Since the grid is fixed on the moving particles, the entire time history of all the field variables at the material point can be easily tracked.
2) Irregular and complicated geometries can be conveniently treated by using an irregular grid.
3) Grid nodes can be placed along boundaries and material interfaces, in this way boundary conditions at free surface, moving boundaries and material interfaces are automatically imposed, tracked and determined simply by the movement of these grid nodes.
However, Lagrangian methods are difficult to apply for cases with an extremely distorted mesh, because their formulation is always based on a mesh. When the elements strongly deform, the approximation of spatial derivatives and integrals becomes unreliable, and so does the solution of the equations. The elements will finally overlap or flip over. No large deformation can be obtained with this model without solving these problems. In general, tectonic processes are accompanied by large deformations of the lithosphere and of the mantle. This means that considerable deformations of the grid domain are required. A possible option to enhance the Lagrangian computation is to remesh the problem domain. This means that periodically the deformed grid is replaced by a new grid in which the elements are less deformed, and the value of different parameters are mapped from the old to the new grid.
There are several ways to remesh the model domain. One can either choose new material particles and interpolate the various variables (e.g., Poliakov and Podladchikov, 1992) or keep the material particles and renew the links (the element sides) between the nodes (e.g. Braun & Sambridge, 1994).
In the first method, the new mesh has to be conformable to the old one just along the boundaries to ensure that these are properly tracked during the process. The drawback of this method is that interpolations are needed from the old mesh to the new one for all the quantities stored in the nodes (velocity, displacement, temperature, etc.) and in the elements (stress, strain). This method is therefore affected by the inaccuracy of the interpolation.
The second method does not require interpolation of the quantities stored in the nodes, since the same material particles are used to define the mesh. The drawback of this method is that the clustering of nodes in some region is not handled. However, in the process we will model in the next chapters, the grid will not be deformed to the extent that such a problem arises. For this reason the second remeshing method is chosen here.

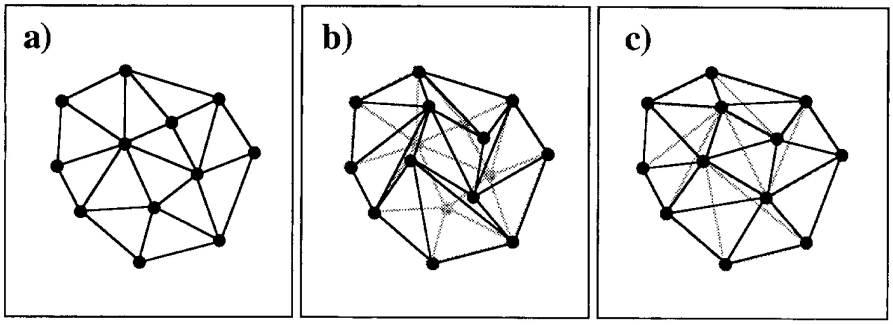

Figure 2.1: The initial undeformed grid a) becomes deformed b), leading to numerical inaccuracy, that can be avoided trough the reconnection of the nodes c). The nodes are always the same material points.

2.2 The remeshing procedure

2.2.1 Construction of the new mesh

Now we will illustrate the basic principle of our remeshing technique. The finite element mesh in Figure 2.1 is distorted from configuration a) to configuration b). The mesh is so distorted that the integrals and the derivatives needed in the finite element equations cannot be properly approximated. If we reconnect the nodes in such a way that the elements are well shaped (Fig 2.1 , configuration c)), the new grid will allow for a better approximation of the necessary integrals and derivatives. The new mesh is based on the original Lagrangian material nodes. The idea of the method used is therefore to keep the same material properties to build the finite element mesh, but to allow the connectivity between the nodes to change in time, accommodating in this way the ongoing deformations.
For the problems that are handled in this thesis, it is very important that the topography of the boundaries between the different layers is maintained throughout the remeshing procedure. So when defining the new mesh, these boundaries are preserved. The new numerical mesh has the same boundary as the old one, so that the new and old mesh are adequate discretizations of the same material regions. The numbers of nodes and elements are the same before and after the remeshing is performed. The new mesh is designed with the program *Triangle* (VERSION 1.6). *Triangle* is a C program for two-dimensional mesh generation and construction of Delaunay triangulations, constrained Delaunay triangulations, and Voronoi diagrams. A

Delaunay triangulation of a vertex set is a triangulation of the vertex set with the property that no vertex in the vertex set falls in the interior of the circumcircle (circle that passes through all three vertices) of any triangle in the triangulation. *Triangle* is fast, memory-efficient, and robust; it computes Delaunay triangulations and constrained Delaunay triangulations exactly. Guaranteed-quality meshes (having no small angles) are generated using Ruppert's Delaunay refinement algorithm. *Triangle* is freely available on the web at http://www.cs.cmu.edu/ quake/triangle.html and from Netlib.

2.2.2 The mapping procedure

The scalar values attached to the nodes (such as temperature, velocity, displacement) do not need to be interpolated from one grid to the other, because the new triangles are constructed with the same material points as the nodes in which the old triangles were constructed. The values that are attached to the elements, such as the stress tensor, have to be mapped from the old to new grid. In order to do this the closest neighbors are chosen. The distances between the center of the old elements and each new element are calculated. When the closest couple is found the tensor will be mapped from the old to the new element. This can easily be done because the central coordinates of the new and old elements are known.
In using this procedure the nodal forces are only approximatively balanced by internal stresses. After the mapping, to improve and correct the stress values some iterations with static grid are performed (the grid is not deforming) using the new connectivity. This procedure is performed to ensure that a force balance is reached at the end of those iterations. The nodal force will correct the total stress distribution but it will not change the displacement. After the remeshing the finite element equations (A-1), (A-2), (A-3) become:

$$\boldsymbol{K}\delta\boldsymbol{u} = \boldsymbol{Q}, \tag{2.1}$$

$$\boldsymbol{K} = \int_{\Omega^{new}} \boldsymbol{B^T D B} d\Omega^{new}, \tag{2.2}$$

$$\boldsymbol{Q} = \overline{\boldsymbol{Q}} - \int_{\Omega^{new}} d\boldsymbol{N^T X} d\Omega^{new} - \int_{\partial\Omega^{new}} d\boldsymbol{N^T T} dS^{new}, \tag{2.3}$$

where *new* indicates the new connectivity. An explanation of the above equations is given in Appendix A

2.3 Testing the remeshing

In order to test the remeshing procedure we consider the transient acceleration from rest of a cylinder of density ρ_c and radius a as it settles under gravity along a centerline of a plane channel of radius R containing a viscoelastic Maxwell material.
Generally, the axis-symmetric problem with a sphere settling in a cylinder has been selected as a numerical benchmark problem for comparison of results from different steady and time-dependent computational algorithms (e.g. Bodart & Crochet, 1994; Becker et al., 1994). We can not compare in a quantitative way our planar case with the axis-symmetric case, but we can use those experiments to indicate that our results are qualitatively reasonable. We have found few examples in literature that treat the same problem for a cylinder. We compare our results with the ones of Feng et al. (1996), but we have to take in consideration that while we use a Maxwell model to describe viscoelasticity, they use an Oldroyd-B fluid. The Oldroyd-B fluid is a combination of Maxwell and Newtonian material and it is characterized by two viscosity values. Finite element calculations of the trajectory of the cylinder are compared in models with and without remeshing.

2.3.1 Model setup

The mechanics of the process is governed by the momentum equation:

$$\bigtriangledown \cdot \sigma + \rho g = 0 \tag{2.4}$$

with the corresponding boundary conditions.
We solve this partial differential equation for instantaneous velocities and stresses using the plane strain approximation. We use the G-TECTON finite element code (Govers & Wortel, 1993), which was developed from TECTON version 1.3 (Melosh & Raefsky, 1983), to solve the momentum equation. Constitutive laws in the model represent Maxwell visco-elastic deformation. Viscoelasticity describes materials that exhibit both viscous and elastic characteristics. The Maxwell model can be represented by a dashpot that is a purely viscous damper and a purely elastic spring connected in series. The model represents a liquid (able to have irreversible deformations) with some additional reversible (elastic) deformations. If put under a constant strain, the stresses gradually relax. When a material is put under a constant stress, the strain has two components. First, an elastic component occurs instantaneously, corresponding to the spring, and relaxes immediately upon release of the stress. The second is a viscous component that grows with time as long as the stress is applied.

In the experiments a cylinder with a radius of 0.25 cm is released in a plane channel of radius 0.5 cm. The total length of the channel is 5 cm. The cylinder is at rest and

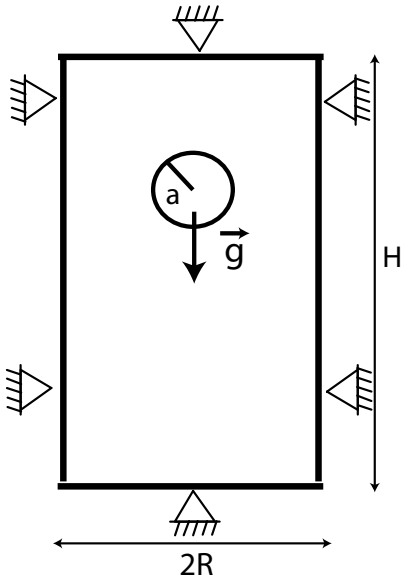

Figure 2.2: Sketch of the physical system. The horizontally placed cylinder with radius a is driven by gravity. Boundary conditions: Along the boundary of the box no displacement is allowed.

is horizontally placed (see Fig. 2.2). The distance between the center of the cylinder and the top surface is 1.75 cm, and between the center of the cylinder and the bottom it is 3.25 cm. The position of the cylinder is chosen far enough from the bottom in order not to influence the settling velocity.
The numerical grid used in the experiments consists of 3922 nodal points and 7540 triangles. We tested the convergence of the experiments for the selected grid. The settling of a sphere or of a cylinder in a tube or plane channel filled with viscous material is determined by the following dimensionless numbers:

$$Re = \frac{\rho_f U_t a}{\eta}, \quad De = \frac{U_t \lambda}{a}, \quad f(a/R) = \frac{U_t(a/R)}{U_{inf}}, \quad \alpha = \frac{a}{R}, \quad \frac{\rho_f}{\rho_c} = 26.7. \tag{2.5}$$

Where *Re* is the Reynolds number, *De* the Deborah number, *f(a/R)* the wall correction factor. U_{inf} is the characteristic or terminal velocity as the steady state velocity that a cylinder of density ρ_c and radius *a* would settle in an unbounded geometry in purely viscous fluid of density ρ_f and viscosity η. The expression of the U_{inf} for a cylinder is given by:

$$\frac{U_{inf}}{ln(3.7\frac{\eta}{\rho_f U_{inf} a})} = \frac{1}{4}\frac{\rho_s - \rho_f}{\eta} g a^2. \tag{2.6}$$

This is an implicit formula which can only be solved numerically. For our set of parameters the velocity obtained from equation(2.6) is about 25 cm/yr. Following Ristov (1996) we correct this value to 1.75 cm/s through the wall correction factor expressed in the following formula:

$$f(a/R) \approx 1 - 1.86\frac{a}{R}. \tag{2.7}$$

When the material in which the cylinder sinks is viscoelastic the wall correction factor decreases below the value obtained for a Newtonian fluid of identical viscosity and so does the terminal velocity. Therefore, the value of the terminal velocity will be lower than 1.75 cm/s. There is not an analytical expression for such a viscoelastic wall correction factor.
The parameters used in the experiments are listed in Table 2.1. In our calculation the values of the dimensionless numbers listed before are: *Re* $= 0.00255$, *De* $= 0.0039$, *f(a/R)* $= 0.0232$, $\alpha = 0.5$.
We impose no-slip boundary conditions along the walls of the box (Fig.2.2). No velocity boundary conditions are imposed on the cylinder. The only force acting on the system is gravity.

material type	η viscosity	E Young modulus	ν Poison ratio	ρ density
fluid	1.64 Pa s	$3.5{\cdot}10^{2}$ Pa	0.25	289 kg/m^3
cylinder	$1.64{\cdot}10^{20}$ Pa s	$3.5{\cdot}10^{13}$ Pa	0.25	7450 kg/m^3

Table 2.1: Material properties

We use three types of models: one without remeshing (MODEL), one in which the remeshing procedure is performed every 20 time-steps (MODEL20) and one in which the remeshing procedure is performed every 50 time-steps (MODEL50).

2.3.2 Results

Figure 2.3 and Figure 2.4 display the evolution of the velocity distribution of the settling cylinder for the case without remeshing and with remeshing every 50 time-steps, respectively. In Figure 2.3 , the cylinder starts to sink, when the mesh becomes too distorted (374 τ) the settling velocity decreases, until the cylinder stops (4204 τ). In Figure 2.4, it is shown that the remeshing of the grid allowed the cylinder to sink with a constant velocity until it reaches the bottom of the box (4204 τ) .

In order to study the velocity evolution in more detail, we examine in Figure 2.5 the time-dependent axial curves obtained for the three models. The settling velocity of the cylinder along the centerline of the channel is plotted. The velocity values are divided by the terminal velocity $U_t \approx 0.5$ cm/yr and the time is expressed in seconds. The light grey curve represents MODEL, the black curve represents MODEL20, the dark grey curve represents MODEL50. The initial behavior is similar for the three models, the results show that the velocity instantly reaches its maximum value and after it rapidly decreases. In MODEL, the velocity does not reach a steady state behavior, it continuously decreases to zero far before reaching the bottom of the box. MODEL20 and MODEL50 are characterized by a very different response: the velocity in both cases reaches the same steady state value. The main difference between MODEL20 and MODEL50 is that the last one oscillates around the terminal velocity value, while the first one is more stable. This is due to the fact that when the remeshing is used more often the inaccuracy due to the mapping procedure is reduced. In MODEL20 the amount of residual force due to the remeshing is about 4 $\%$ less than in MODEL50.

In order to establish if the remeshing gives reasonable results, we compare our experiments with the ones in literature. As mentioned before, most of similar numerical

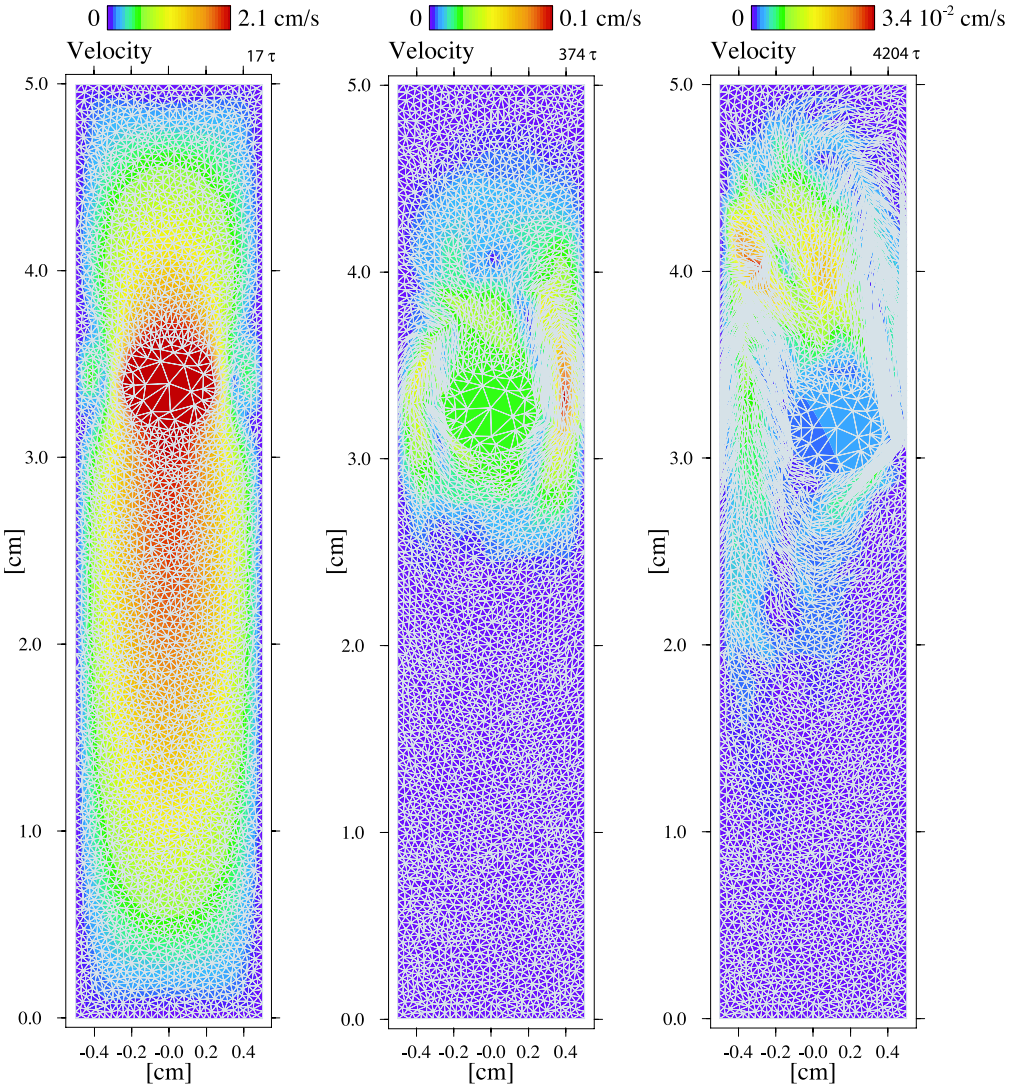

Figure 2.3: Velocity distribution for the model without remeshing (MODEL). On the left the velocity after 17 Maxwell times (17 τ), in the middle after 374 τ, on the right after 4204 τ.

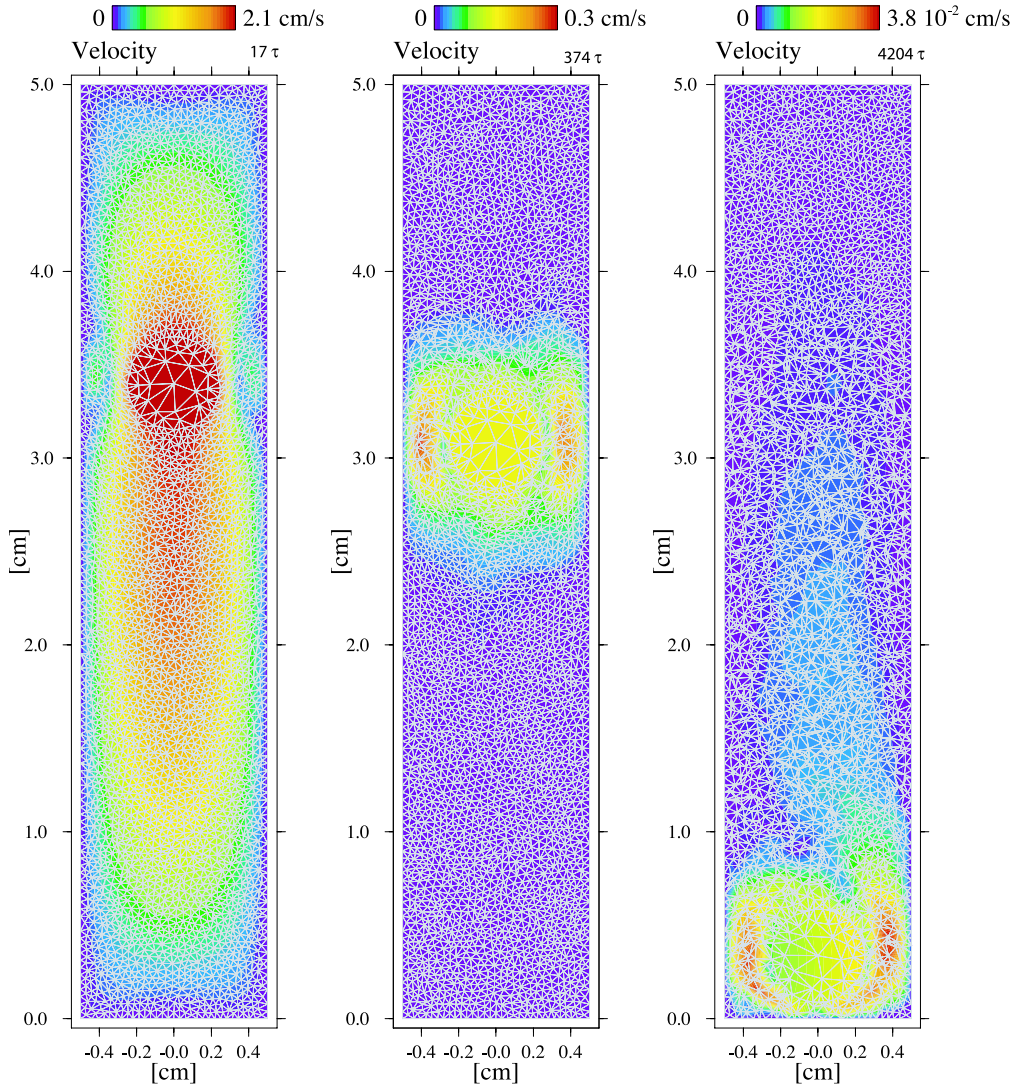

Figure 2.4: Velocity distribution for the model with remeshing (MODEL50). On the left the velocity after 17 Maxwell times (17 τ), in the middle after 374 τ, on the right after 4204 τ.

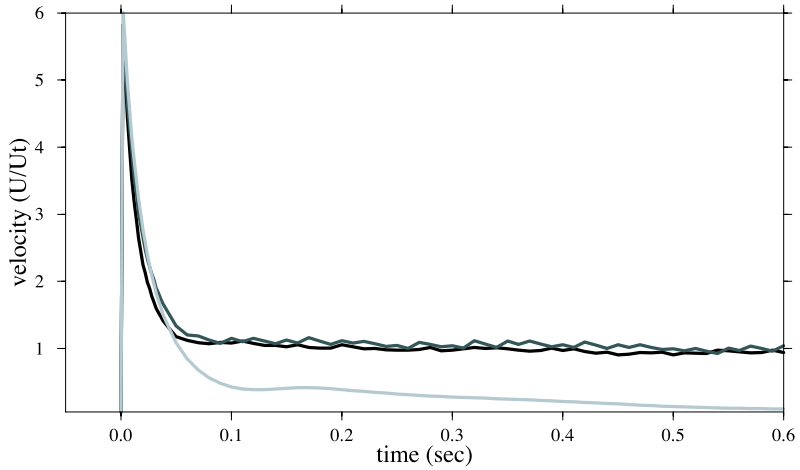

Figure 2.5: Velocity of the cylinder in time. The model without remeshing is plotted with a light grey curve, the model with remeshing every 50 time steps is plotted with a dark grey curve, the model with remeshing every 20 time steps is plotted with a black curve.

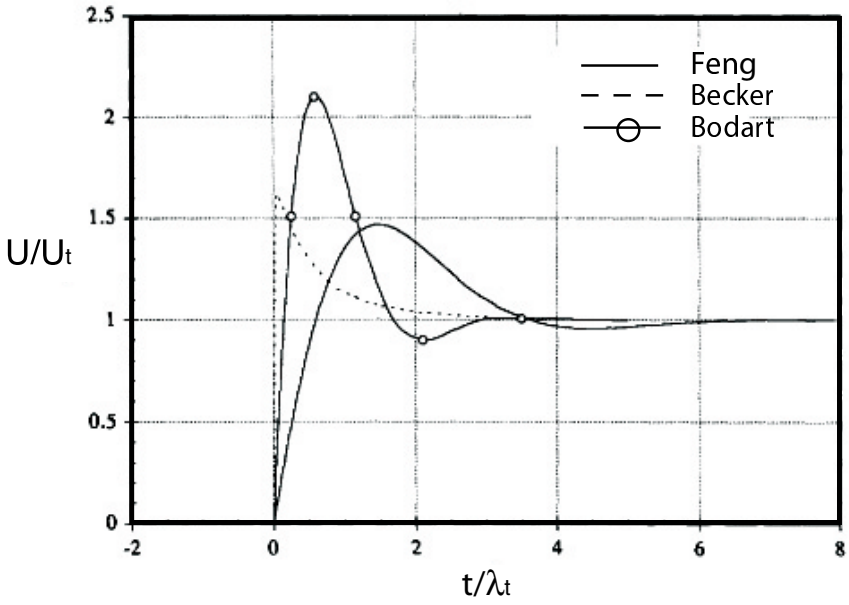

Figure 2.6: Settling velocity in three studies. Feng et al. (1996) $Re = 0.02255$, $De = 0.2255$, $\alpha = 0.5$, $\rho_s/\rho_f = 26.74$. Bodart & Crochet (1994) $Re = 0.6468$, $De = 1.986$, $\alpha = 0.5$, $\rho_s/\rho_f = 7.162$. Becker et al. (1994) $Re = 5.27 \times 10^{-3}$, $De = 0.402$, $\alpha = 0.243$.

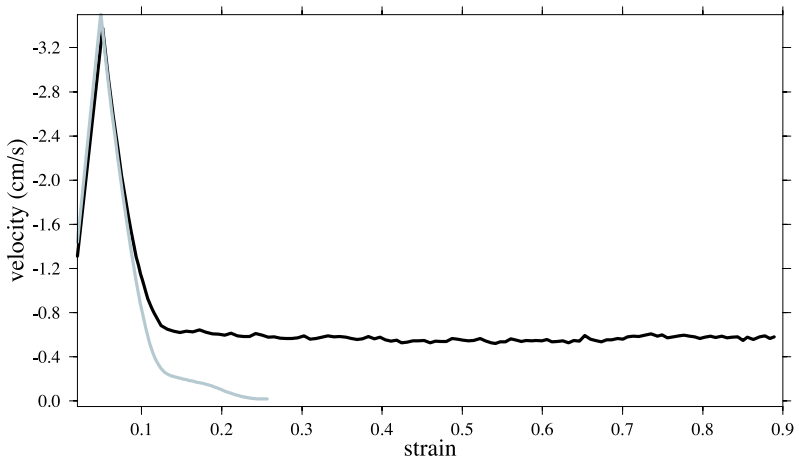

Figure 2.7: Velocity of the cylinder in function of strain. The model without remeshing is plotted with a light grey curve, the model with remeshing every 20 time steps is plotted with a black curve.

experiments are made for a sinking sphere. Therefore, while comparing our planar case with axis-symmetric cases, it is obviously impossible to match the dimensionless quantities introduced in the previous paragraph. We compare our model with a planar case as well but even in this case it is not possible to match the dimensionless quantities, since they solve the Navier-Stokes equation coupled with a Oldroyd-B fluid. This means that they have different material equations. Thus, a meaningful quantitative comparisons cannot be made. Figure 2.6 shows the variation of the settling velocity obtained with two axis-symmetric calculations for a sphere (Bodart & Crochet, 1994; Becker et al., 1994) and with one for a sinking cylinder (Feng et al., 1996). The result of Becker et al. (1994) is the most similar to ours. They used a Lagrangian finite element method. In all three computations - as well as in our models - a large overshoot in the falling speed is obtained, consistent with the experimental observation of Walters & Tanner (1992) and Becker et al. (1994). The terminal velocity is approached through a damped oscillation. This result is in agreement with our MODEL20 and MODEL50. MODEL does not reproduce such behavior.
The above comparisons indicate that our remeshing procedure gives qualitatively reasonable results for the test problem, while the model without remeshing completely fails to reproduce the same result. The accuracy of the results cannot be assessed at present owing the lack of comparable data.

In Figure 2.7, the velocity of MODEL20 and MODEL is plotted as a function of the

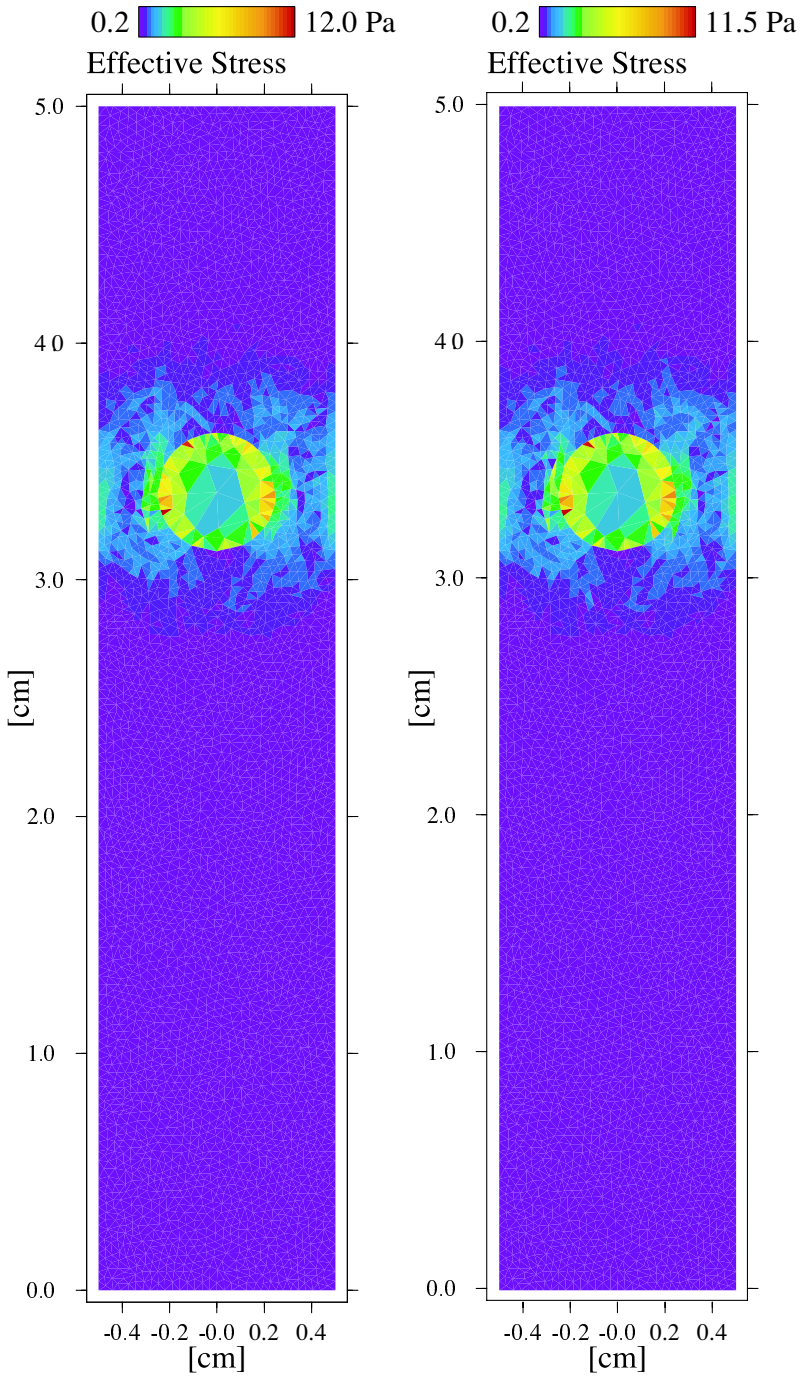

Figure 2.8: Stress distribution for MODEL20. Right side: effective stress distribution before the remeshing. Left side: effective stress distribution after the remeshing.

strain. In MODEL20 the velocity reaches steady state at increasing strain, while in MODEL where no remeshing is applied the velocity becomes zero. This strongly indicates that, thanks to the remeshing procedure, large deformation problems can be handled.
Figure 2.8 shows the stress distribution for MODEL20, before (left side) and immediately after remeshing (right side). We see that the stresses do not change drastically after the remeshing. This comparison is done in order to show that the mapping procedure from the new to the old stress field does not cause an unrealistic stress distribution.
In a processor Intel Pentium III CPU family 1133MHz we computed that applying the remeshing 5 times over 100 time-steps makes the process 50% slower.

2.4 Conclusion

The numerical experiments we performed illustrate the ability of our remeshing procedure to handle large deformation. We showed the remeshing procedure produces a physically meaningful behavior of a cylinder settling in a viscoelastic material: the sinking cylinder reaches a steady state velocity. Without remeshing steady state is not reached: the cylinder velocity becomes zero far before reaching the bottom of the box, therefore the process is not correctly reproduced. Our results are consistent with the experiments obtained by other numerical and experimental models for similar problems.

2.5 APPENDIX A: The finite element method (FEM)

In this appendix we will provide a simple introduction to the finite element method (FEM).
The study of rock deformation is a complex, non linear problem that it is often not possible to describe through an analytical mathematical formulation. An analytical solution is a mathematical expression that gives the value of the desired unknown quantity at any location in a body. Analytical solution can be obtained only for certain simplified situations. For problems involving complex material properties and boundary conditions, numerical methods are required. In most numerical methods, the solution gives the unknown quantities only at a discrete number of points in the body. The discretization is the process of selecting only a certain number of points. One way to discretize a body is to divide it into a system of smaller bodies. The assemblage of such units represents the original body. Instead of solving the problem for the entire body in one operation, the solutions are found for each unit and combined together to obtain the solution for the original body. The FEM is based on such an idea.
The description of the FEM can be summarized in a step by step procedure. This sequence of steps describes the process that is followed in setting up and solving any equilibrium problem. The following six steps summarize the FEM analysis procedure:
1) *Discretization of the continuum.* The continuum is the physical body. Discretization is the process in which the body is divided in an equivalent system of finite elements. For a two dimensional continuum the finite elements may be triangles or quadrilaterals. Every finite element is constituted by nodes connected to each other by segments.
2) *Selection of the displacement models.* Simple functions are chosen to approximate the distribution of displacements over each element. The assumed displacement function only approximately represents the exact distribution of the displacements.
Three factors influence the selection of the displacement model. First, the type and degree of displacement model must be chosen. Second, the particular displacement magnitudes must be selected. These are usually the displacements of the nodal point, but they may also include the derivatives of the displacements at some or all the nodes. Third, the model should satisfy certain requirements which ensure that the numerical results approach the correct solution.
3) *Derivation of the element stiffness matrix using a variational principle.* The stiffness matrix consists of the coefficients of the equilibrium equations derived from the material and geometric properties of an element and obtained using the principle of minimum potential energy. The potential energy of a loaded body is given by the

sum of internal energy stored as result of the deformation and the potential energy of the external load. This energy is a minimum if the body is at equilibrium. The stiffness relates the displacements at the nodal points to the applied force at the nodal points. The distributed forces applied to the structure are converted into equivalent concentrated forces at the nodal points. The equilibrium relation between the stiffness matrix $\boldsymbol{K}$, displacement increment vector $\delta\boldsymbol{u}$, nodal force vector or load $\boldsymbol{Q}$ is expressed as a set of equations:

$$\boldsymbol{K}\delta\boldsymbol{u} = \boldsymbol{Q} \tag{A-1}$$

$$\boldsymbol{K} = \int_{\Omega} \boldsymbol{B^T D B} d\Omega \tag{A-2}$$

$$\boldsymbol{Q} = \overline{\boldsymbol{Q}} - \int_{\Omega} d\boldsymbol{N^T X} d\Omega - \int_{\partial\Omega} d\boldsymbol{N^T T} dS \tag{A-3}$$

where $\boldsymbol{D}$ is the constitutive matrix, $\boldsymbol{B}$ is the strain displacement matrix, $\overline{\boldsymbol{Q}}$ is the nodal force vector, $\boldsymbol{N}$ is the interpolation matrix, $\boldsymbol{X}$ is the body force vector and $\boldsymbol{T}$ the traction. In equation A-1 the external force is given by the concentrated forces, the distributed load and the surface traction respectively.

4) *Assembly of the algebraic equations for the overall discretized continuum.* This process includes the assembly of the global stiffness matrix for the entire body from the individual stiffness matrices, and the global force vector from the nodal force vectors. In general, an assembly method requires the displacement at the node to be the same for all the elements adjacent to that node (continuity of the displacement). An overall equilibrium equation can be written, with a total stiffness matrix, a total force vector and a nodal displacement vector for the entire body. To solve the new equations, boundary conditions must be applied.

5) *Solution for the unknown displacement.* The algebraic equations assembled in the previous step are solved for the unknown displacements. For non linear problems the solutions are obtained by a sequence of steps, each step involving the modification of the stiffness matrix and/or load vector.

6) *Computation of the element strains and stresses from the nodal displacements.* Often after the displacement is calculated, other quantities, such strain and stress, must be computed. In general, strain and stress are proportional to the derivatives of the displacement.

Chapter 3

Numerical comparison of different convergent plate contacts: subduction channel and subduction fault

At convergent plate boundaries, the properties of the actual plate contact are important for the overall dynamics. Convergent plate boundaries both mechanically decouple and link tectonic plates and accommodate large amounts of strain. We investigate two fundamental physical states of the subduction contact: one based on a fault and the other based on a subduction channel. Using a finite element method, we determine the specific signatures of both states of the subduction contact. We pay particular attention to the overriding plate. In a tectonic setting of converging plates, where the subducting plate is freely moving, the subduction channel reduces compression relative to the fault model. In a land-locked basin setting, where the relative motion between the far field of the plates is zero, the subduction channel model produces tensile stress regime in the overriding plate, even though the amount of slab roll-back is small. The fault model shows a stronger development of slab roll-back and a compressive stress regime in the upper plate. Based on a consistent comparison of fault and channel numerical models, we find that the nature of the plate contact is one of the controlling factors in developing or not the back-arc extension. We conclude that the type of plate contact plays a decisive role in controlling the back-arc

Published as: R. De Franco, R. Govers and R. Wortel, Numerical comparison of different convergent plate contacts: subduction channel and subduction fault, *Geophysical Journal International* 271, 435-450, 2007, with the changes indicated where appropriate

state of stress. To obtain back-arc extension, roll-back is required as an underling geodynamical process, but it is not always a sufficient condition.

3.1 Introduction

Whereas several correlations between observed parameters in subduction zones have been established, the physical meaning of such correlations is only partially understood. In convergent plate boundaries, the properties of the actual plate contact are important for the overall dynamics. For the operation of plate tectonics a relatively low shear strength is a critical mechanical property of plate contacts (Tackley, 2000). The effective friction at a subduction zone has a first order control on plate boundary topography and the plate-liken motion (Zhong et al., 1998). In the most simple representation the plate contact is a single fault, and the friction coefficient controls the jump in fault parallel velocities across the fault, i.e., the level of decoupling. Plate contacts between oceanic plates come closest to such single fault representation, but even there closer examination consistently shows that strain is distributed.
In the late seventies and early eighties two-dimensional models were introduced with a weak subduction contact zone of few hundred kilometers wide (Kapitzke, 1979; Schmeling & Jacoby, 1981; Jacoby & Schmeling, 1982). The weak zones were used to localize deformation and to mimic rheological stress weakening. The limitation of such formulation was that the deformation was distributed over the entire weak zone which conflicted with seismic observations. Shreve & Cloos (1986) proposed that the descending plate carries a layer of sediments down into a relatively thin subduction channel (0.3 to 5.3 km) beneath the overriding block. These sediments were proposed to act as a lubricating layer. The transmission of velocity and stress between plates was regulated by the dimension, the pressure distribution and the rheology of the channel (Shreve & Cloos, 1986).
More observational support for channels of a few kilometers has been collected since. All over the world, seismic studies have shown the presence of inter-plate sedimentary channel-like units of about 1-8 km (Eberhart-Phillips & Martin, 1999; Oncken et al., 2003; Abers, 2005; Tsuru et al., 2002). More indirect evidence for a subduction channel comes from the observation of high-pressure and ultra-high-pressure metamorphic minerals in relicts of continental crust, which document pressures in excess of 3 GPa (corresponding to a depth of about 100 km) at relatively low temperatures. The common interpretation of these observations is that the sediments were subducted and subsequently exhumed very rapidly (Smith, 1984; Chopin, 2001). A subduction channel was invoked to explain this process and it was quantitatively modeled by Gerya et al. (2002).
There are two reasons why the sediment channel cannot be a good description of

all subduction zones. First, great subduction earthquakes attest to the fact that the subduction interface cannot be weak everywhere (Davies & Brune, 1971; Kanamori, 1977; Ruff & Kanamori, 1983; Tichelaar & Ruff, 1993). Most inter-plate seismicity occurs at depth range of 0-50 km (Tichelaar & Ruff, 1993), meaning that at least the shallow part of the subduction zone has a finite shear strength. Second, sediment supply varies widely from site to site as indicated by accretionary wedge dimensions and erosive margin observations. This means that when the amount of sediments is small, the subduction channel becomes so thin that a more appropriate description of the plate contact is by one or several faults. Fault normal velocities and tractions are continuous, and plates are fully coupled in this direction.

On the scale of the entire lithosphere, quantitative models based on a single through-going subduction fault have been used to investigate how the fault properties influence the stress distribution and plate boundary forces associated with subduction (Bott et al., 1989; Whittaker et al., 1992; Giunchi et al., 1996). Zhong & Gurnis (1994, 1994b), and Zhong et al. (1998) pointed out that a subducting slab with a fault produces plate like behavior, trench and fore bulge topography and principal stresses consistent with observations.

Thus, there is support for both types of contact zones. The fault and the subduction channel represent two physical different states of the subduction plate contact. A subduction zone may evolve from one state to another through a varying sediment supply. Along strike variations in the physical state of a single subduction zone are also conceivable.

Another fundamental aspect governing the response of subduction is the tectonic setting of the plates. In subduction zones, the range of tectonic settings is wide; for instance, the overriding plate can be driven towards or away from the trench or be stationary; the subducting plate can be actively driven into the subduction zone, or not. Another possibility is that collision effectively hampers further subduction. Clearly, the stress and the velocity distribution of the area are affected by these factors. Here we focus on tectonic settings where motions are driven entirely within the model domain: 1) the setting in which the overriding plate is stationary in the far field and the oceanic subducting plate is freely moving (free subduction), 2) a land-locked basin setting where there is no net convergence between the surface plates, so that subduction must occur through roll-back (e.g., Mediterranean basin).

The aim of our study is to determine the specific signatures of both states of subduction zones, i.e., a subduction fault and a subduction channel, in these tectonic settings. Through numerical modeling we evaluate overriding plate velocities, stress field in the back-arc region and topography for both types. By using a single finite element program for both types of models, the results are internally consistent and, therefore, well suited for comparison.

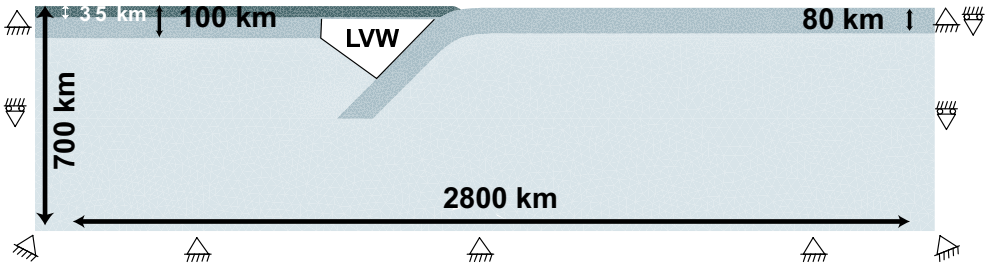

Figure 3.1: Model setup. On the left the continental plate with on top the continental crust, on the right the oceanic plate. Boundary conditions: on the bottom no displacement; on the left: the lithosphere is locked, in the mantle horizontal displacement is allowed; on the right: the lithosphere is locked, in the mantle horizontal displacement is allowed.

3.2 Numerical method and model setup

For the purpose of this study we focus on a generic subduction zone, i.e., we do not focus on any particular convergent plate boundary. In such a generalized subduction zone we choose to omit some of the geometric details that have been documented by the recent compilation by Lallemand et al. (2005). While important for making accurate predictions for any real subduction zone, these details do not affect the principal functioning of the subduction zone and would merely add complexity that clouds our understanding of the physical process. One major simplification we make for this very same reason is that the subduction zone is well represented by a two dimensional cross section (Fig.3.1).

The long term mechanics of the lithosphere and upper mantle is governed by the momentum equation. We solve this partial differential equation for instantaneous velocities and stresses using the plain strain approximation. We use the G-TECTON finite element code (Govers & Wortel, 1993), which was developed from TECTON version 1.3 (Melosh & Raefsky, 1983), to solve the momentum equation. Constitutive laws in the model represent elastic, viscous and plastic deformation.

Viscosity is taken to be strongly temperature dependent, in accordance with rock mechanical experiments in both the powerlaw and diffusion creep regime (e.g., Kohlsteldt & Zimmerman, 1996). Density also depends on temperature and we adopt a linear equation of state in our model. These dependences make it necessary to also solve for model temperature.

The initial temperature field is computed with a new finite element solver in G-TECTON for the steady state diffusion-advection equation. This solver is based on a streamline upwind Petrov-Galerkin (SUPG) formulation (see Appendix B). A unique

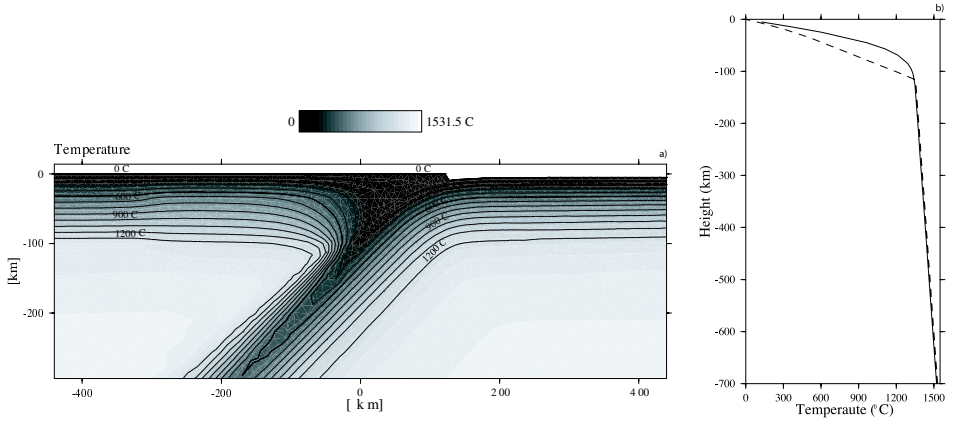

Figure 3.2: a). Total temperature distribution. b). Geotherm at the sides of the model domain. Solid curve: temperature boundary condition at the right side of the model; dashed curve: temperature boundary condition at the left side of the model.

feature of our implementation is that we facilitate discontinuities in the velocity field (at faults) via a split node technique. The temperature solutions were verified to be identical to those resulting from integrating the time-dependent conduction equation for a long time (finite difference code of van de Zedde & Wortel (2001)). As the mechanical models of this paper focus on short time scales, relative to a thermal diffusion time scale, we ignore the temporal evolution of conduction. We do account for advective heat transport through the Lagrangian motion of the numerical grid.

We assume the surface oceanic lithosphere has an age of 33 My at the right hand model boundary. Here the initial geotherm is defined using a half space cooling model. Using a convergence velocity of 4 cm/yr, which in our models corresponds to the spreading rate of the oceanic lithosphere, the oceanic age at the trench is of 70 My. Temperatures in the continental overriding plate are based on a representative steady state geotherm with a surface heat flow of 65 mW/m^2 (Table 3.1). We use a adiabatic gradient of 0.3 K per km. Temperature boundary conditions at the top and bottom of the model domain are 0 ^{o}C and 1531 ^{o}C. The initial temperature field is displayed in Figure 3.2a). Temperatures at the right and left side of the model correspond to the two geotherms plotted in Figure 3.2 b).

The velocity field to compute the initial temperatures has a uniform velocity of 4 cm/yr for both the surface oceanic plate and the slab. Velocity directions are everywhere parallel to the local mid-plane orientation to avoid deviations from incompress-

ible flow. In the temperature calculations, the velocity of the continental lithosphere is uniformly set to zero. The velocity field in the arc corner is calculated using an analytical corner flow solution, which depends on the subduction velocity and on the angle of subduction.

Our model domain is 700 km deep and 2800 km wide (Fig.3.1). The subducting oceanic plate is on the right, the overriding plate on the left. The shape of the curved slab is defined by an error function (Govers and Wortel, 2005); we adopt a radius of curvature R of $1.6L$ (L being the thickness of the oceanic lithosphere, i.e., 80 km) and final dip angle θ of 45 ^{o}. The slab initially extends to 350 km depth. The overriding plate is 100 km thick, and has a crustal thickness of 35 km.

The rheology of our model is elastic, viscous, or plastic and depends on composition, temperature, pressure and stress (Table 3.1). The viscosity η of steady state flow can be written as:

$$\eta = \frac{1}{2A} exp\Big(\frac{Q + pV}{RT}\Big)\sigma_E^{-(n-1)}, \tag{3.1}$$

where A is the pre-exponent, Q the activation energy, p pressure, V activation volume, R universal gas constant, T temperature, and $\sigma_E \equiv \sqrt{\frac{1}{2}\sigma'_{ij}\sigma'_{ij}}$ the effective stress.

Model viscosities follow from either steady state dislocation creep or diffusion creep. We choose model parameters following Karato & Wu (1993) for the mantle, (intermediate between their wet and dry values (van Thienen et al., 2003)) and following Freed & Burgmann (2004) for the continental crust (see Table 3.1). If $n > 1$, the viscosity is stress dependent as a result of dislocation creep. Steady state diffusion creep results in a viscosity which is independent of stress ($n = 1$) and depends on grain size. This grain size dependence is not apparent in equation(3.1) because we assume a uniform grain size of 1 mm and grain size exponent of 2.5 to correct the pre-exponential term. Dislocation creep is assumed to prevail to a depth of 350 km, and diffusion creep in the transition zone (Karato & Wu, 1993).

We use a low viscosity mantle wedge (LVW) in order to reduce the down-warping of the overriding plate in the arc/back-arc region (Billen & Gurnis, 2001). The mantle wedge is the region of the mantle lithosphere and asthenosphere above the subducting slab (Fig.3.1). In our model, we assume a uniform viscosity of $1 \cdot 10^{19}$ Pa·s in the mantle wedge.

We use an isotropic Von Mises criterion to limit deviatoric stresses in accordance with Byerlee's law (Byerlee, 1978) with hydrostatic fluid pressure and horizontal compression. Yield strength increases linearly with pressure and it is expressed by the equation:

$$Y = \frac{\sqrt{3}}{2}(R - 1)(1 - \lambda)p, \tag{3.2}$$

Thermal properties	k conductivity	H heat production	C_p specific heat	
continental crust	3.2 $W\ m^{-1}K^{-1}$	$6.81 \cdot 10^{-7}\ W\ m^{-3}$	$1 \cdot 10^3\ J\ kg^{-1}\ K^{-1}$	
lithosphere	3.2 $W\ m^{-1}K^{-1}$	0	$1 \cdot 10^3\ J\ kg^{-1}K^{-1}$	
mantle	5.1 $W\ m^{-1}K^{-1}$	0	$1 \cdot 10^3\ J\ kg^{-1}K^{-1}$	
Elastic properties	*E Young's modulus*	*ν Poisson's modulus*		
continental crust	$5 \cdot 10^{10}$ Pa	0.3		
lithosphere	$5 \cdot 10^{10}$ Pa	0.3		
mantle	$1 \cdot 10^{11}$ Pa	0.3		
Creep properties	*A pre-exponent*	*Q activation energy*	*V activation volume*	*n*
continental crust	$3.3 \cdot 10^{-21}\ Pa^{-n}\ s^{-1}$	163 $kJ\ mole^{-1}$	$17 \cdot 10^{-6}\ m^3\ mole^{-1}$	3
mantle $<$ 350 km	$1.317 \cdot 10^{-14}\ Pa^{-n}\ s^{-1}$	485 $kJ\ mole^{-1}$	$25 \cdot 10^{-6}\ m^3\ mole^{-1}$	3
mantle $>$ 350 km	$1.54 \cdot 10^{-11}\ Pa^{-n}\ s^{-1}$	270 $kJ\ mole^{-1}$	$6 \cdot 10^{-6}\ m^3\ mole^{-1}$	1

Table 3.1: Thermal and mechanical model parameters. n is the stress power exponent.

where *Y* is the yield strength, *R* depends on the friction coefficient, λ is the pore fluid pressure, *p* is the pressure. Visco-plastic flow results in permanent deformation in case deviatoric stresses exceed the yield strength. The resulting relaxation brings stresses back to the yield strength level.

We adopt two models for the active plate contact: a subduction fault and a subduction channel, with the following characteristics:
1) A deformable subduction fault is described via updated slippery nodes, in which the fault slip is locally kept parallel to the fault (Buiter et al., 2001). In most models, fault friction is negligible. We name this class of models FNF (fault no friction). We will also present models with a frictional fault (FF).
2) A subduction channel separates the subducting and the overriding plate. The channel width is assumed to be approximately 6 km (Shreve & Cloos, 1986; Beaumont et al., 1999). Channel viscosity is taken to be Newtonian, ranging from $7{\cdot}10^{17}$ Pa·s in our "low viscosity channel" (LVC) models (Shreve & Cloos, 1986; England & Holland, 1979) to 10^{21} Pa·s in the "high viscosity channel" (HVC) models (Renner et al., 2001; Stockhert, 2002; Gerya et al., 2002).

Following Govers & Wortel (2005), we separate model densities into a 1D reference density profile and the remaining density anomalies. Reference densities are used to initialize hydrostatic pressures and which initially do not contribute to the forcing. The remaining density anomalies (i.e., slab pull forces) are used to drive model deformation and are instantaneously applied at the beginning of the model calculation. The initial bending stresses are not included since we assumed a pre-existing subducted slab geometry. The influence of the ridge push is excluded in order to isolate the subduction effect (Bott et al., 1989). In general we do not apply velocities as a forcing, except for one experiment in which we impose a velocity boundary condition

of 7 cm/yr to drive the slab.
We concentrate first on models where the subducting plate is free to move in a horizontal direction. Then we study models for a land-locked basin setting (Le Pichon, 1982), an example of which is the Mediterranean; a very small relative motion between continents that surround an oceanic basin has as a consequence that basin-internal subduction needs to be accompanied by back-arc extension. Our boundary conditions on the lithosphere thus do not allow relative motion between the far field plates.
Our focus on the subduction zone has the consequence that we choose to ignore convective motions beneath the lithosphere which are not driven by the sinking slab or plate motions. We assume that such convection would cause similar imprints on both the subduction fault model and the subduction channel model. For comparing the two types of subduction zones, we thus consider plate-excited mantle flow only. This has one immediate consequence for the boundary conditions acting on the sublithospheric part of side boundaries: these boundaries are far enough from the central down-welling region to result in horizontal in- and outflow only beneath the lithosphere. Because viscous flow is incompressible in our formulation, this constraint has the additional consequence of requiring continuity of horizontal flow beyond our model domain. Consistent with Mitrovica & Forte (1997), we assume a significantly higher viscosity in the lower mantle beneath the lower domain boundary; in our model this is represented by no slip boundary conditions.

3.3 Results

3.3.1 Free subduction

In this setup the upper plate on the left end side is locked via a boundary condition and the subducting plate is free to move horizontally. Figure 3.3a shows the velocity distribution for the frictionless subduction FNF after 250 Kyr (representing about 3100 asthenospheric Maxwell times). This time was chosen on the basis of longer running preliminary experiments which showed that model spin-up signatures had vanished and that the velocity field had reached steady state for the considered time window of about 60 Kyr [1].
Slab pull forces drive a primarily vertical down-welling close to the slab. Eddies are created at the two end sides of the slab. In the oceanic lithosphere, motions are mostly horizontally directed towards the plate contact region. Horizontal return flow dominates in the deeper mantle beneath the slab. Velocity patterns of the different subduction zone models are very similar in most of our model domain, except near

[1] The last part of this sentence has been added after publication

the plate contact zone where there are important differences. Therefore, we will subsequently zoom in on this region.

Frictionless fault subduction zone model (FNF)

Figure 3.3b is a blow up of the subduction region of Figure 3.3a. The subduction fault is defined along the plate interface from the trench to a depth of 100 km. Velocities are oriented towards the trench in the surface oceanic plate, and the magnitude is about 3 cm/yr. The overriding plate moves in the same direction as the subducting plate and the velocities are small, ranging from 0 and 3 mm/yr. In the slab velocities have a slab perpendicular component. Slab sinking induces higher velocities in the wedge than in the oceanic plate.
In Figure 3.4a), the solid line displays the horizontal velocity of the free surface for the entire model domain. For description purposes, the overriding plate is divided into region A, from the trench to the vertically projected tip of the slab, and region B beyond this. The trench is visible as a step velocity change at horizontal coordinate 100 km. The solid curve in Figure 3.4b shows the total vertical displacement of the free surface. The trench is the deepest point of the curve (2 km). A 1-1.2 km depression has developed on the overriding plate in region A. Dynamic uplift of the outer bulge in the oceanic plate is approximately 500 m.
Figure 3.5a shows principal stresses directions as arrows and effective stress as grey contours. In the overriding plate, close to plate contact, the stresses are small. Further to the left the stresses are horizontally compressive. Horizontal tensile stresses dominate the shallow surface oceanic plate. Zero friction at the plate contact can be seen as principal stresses oriented perpendicular to the interface. Stresses are negligible along the shallowest portion of the plate contact and slightly compressive at the interface with the deepest portion of the overriding crust. Significant fault normal stress develops in the slab near the downward tip of the subduction fault. Stresses within the slab do not show the typical signature of elastic bending, i.e., tensile slab parallel stresses in the most shallow part and compressive stresses deeper down. Such stresses do not develop in our setup where we assumed a pre-existing subduction geometry. Our model stresses should be considered as changes due to subduction zone dynamics with respect to these typical initial flexure stresses. In the slab below 40 km depth, the compressive stresses are oriented approximately perpendicular to the slab. Stresses are low in the low-viscosity mantle wedge and beneath the oceanic surface plate.
The solid curve in Figure 3.6 shows the horizontal stress of the free surface for the entire model domain. Tensile stresses dominate in the overriding plate close to the fault, and in the far field on the left side (region B). A strong compression of about 150 MPa develops in region A .

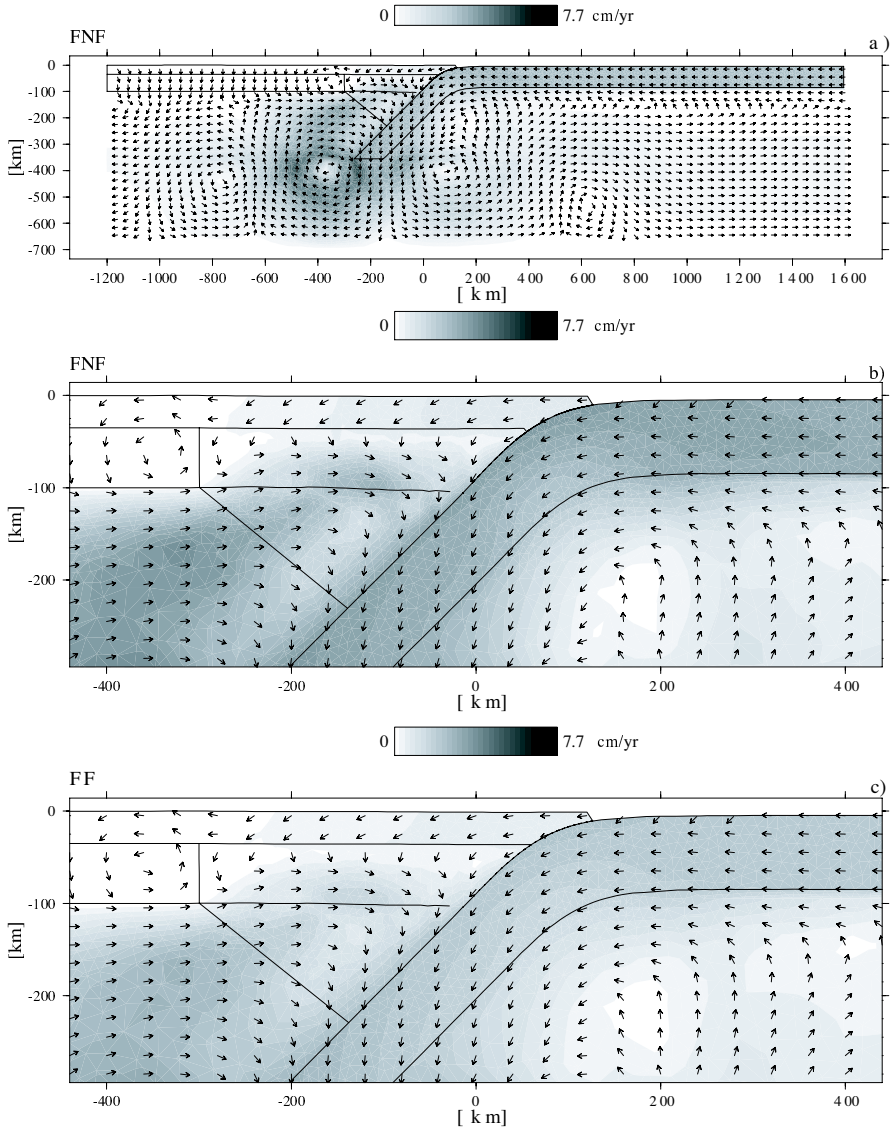

Figure 3.3: Steady state velocity field for free subduction boundary conditions. a) Frictionless fault model (FNF) total view of the model domain, b) FNF enlarged from a), c) Fault model with friction (FF). Note that arrows indicate directions only; arrows are not scaled by velocity magnitude. Velocity magnitude is indicated by the gray scale contours. The solid lines outline the overriding, subducting plate and the LVW.

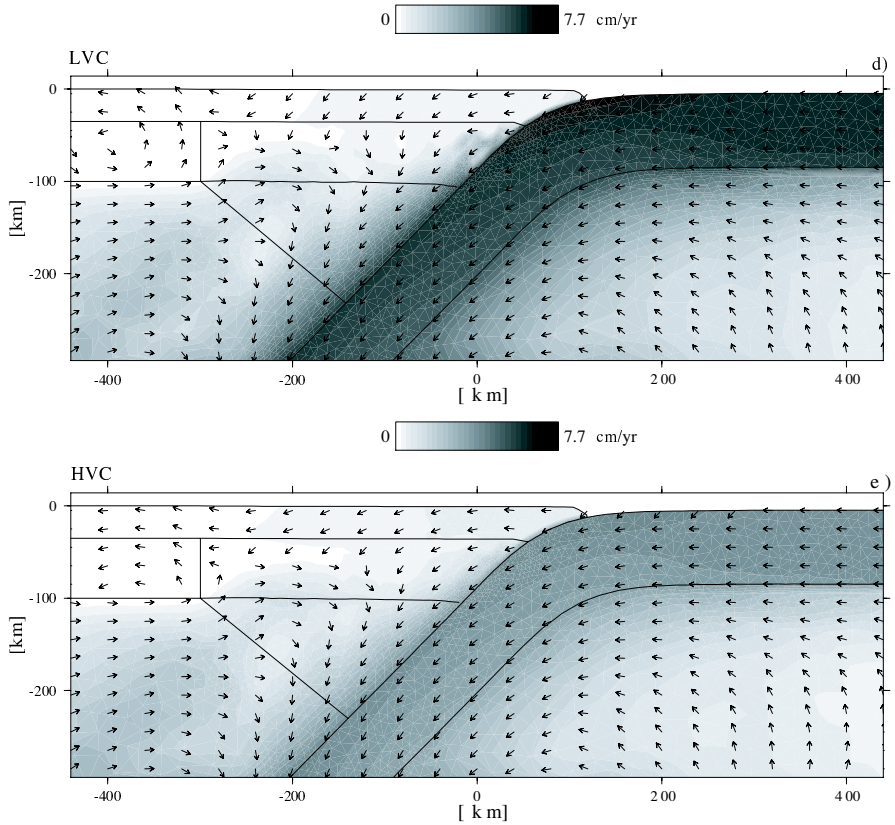

Figure 3.3: (Continued). Steady state velocity filed for free subduction boundary conditions. d) Low viscosity channel model (LVC) $\eta = 7 \cdot 10^{17}$ enlarged from Figure 3.3a. e) High viscosity channel model (HVC) $\eta = 10^{20}$. Note that arrows indicate directions only; arrows are not scaled by velocity magnitude. Velocity magnitude is indicated by the gray scale contours. The solid lines outline the overriding, subducting plate and the LVW.

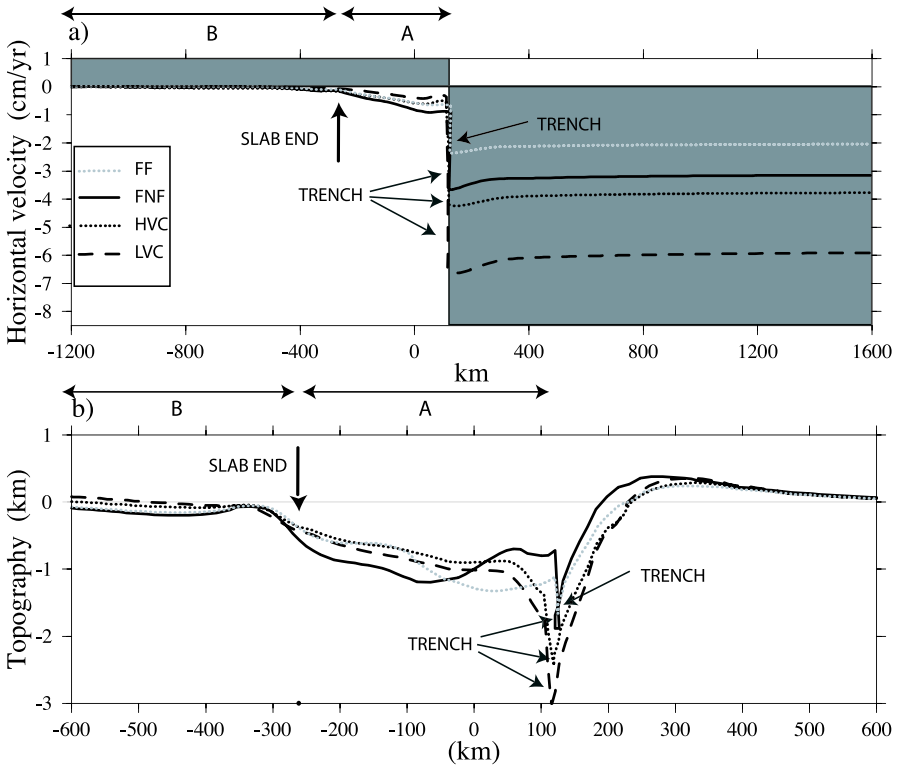

Figure 3.4: Surface expression for models with free subduction boundary conditions. a) Horizontal velocity at the surface of the model for the entire domain: solid curve represents frictionless fault model (FNF), grey dotted curve fault model with friction (FF), black dashed curve low viscosity channel (LVC) model $\eta = 7 \cdot 10^{17}$, black dotted curve high viscosity channel (HVC) model $\eta = 10^{20}$. Velocities in the grey area are directed towards the trench. b) Total vertical displacement of the surface of the model. The vertical black arrow indicates the vertically projected tip of the slab. The overriding plate is divided into region A and region B.

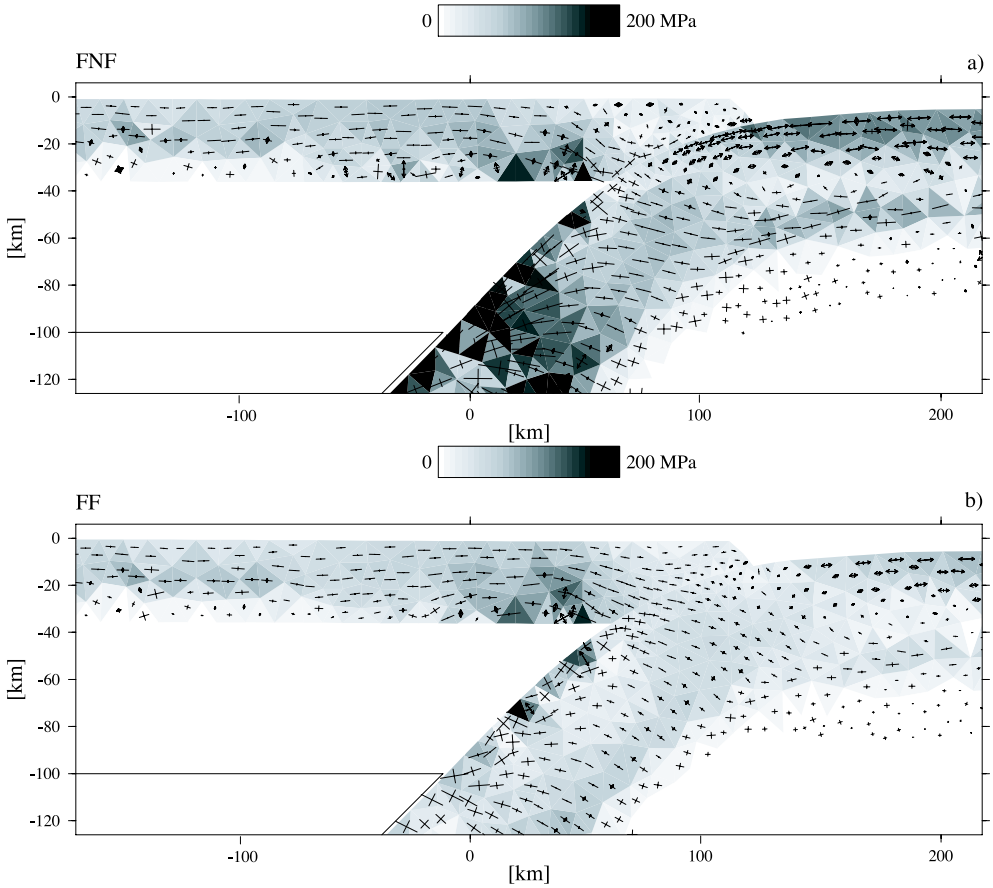

Figure 3.5: Effective stress magnitude and principal deviatoric stresses for models with free subduction boundary conditions after 250 Kyr. Tensile stresses are indicated by arrows, compressive stresses by lines. a) Frictionless fault model (FNF). b) Fault model with friction applied at the fault (FF). The black solid line indicates the initial position of the slab.

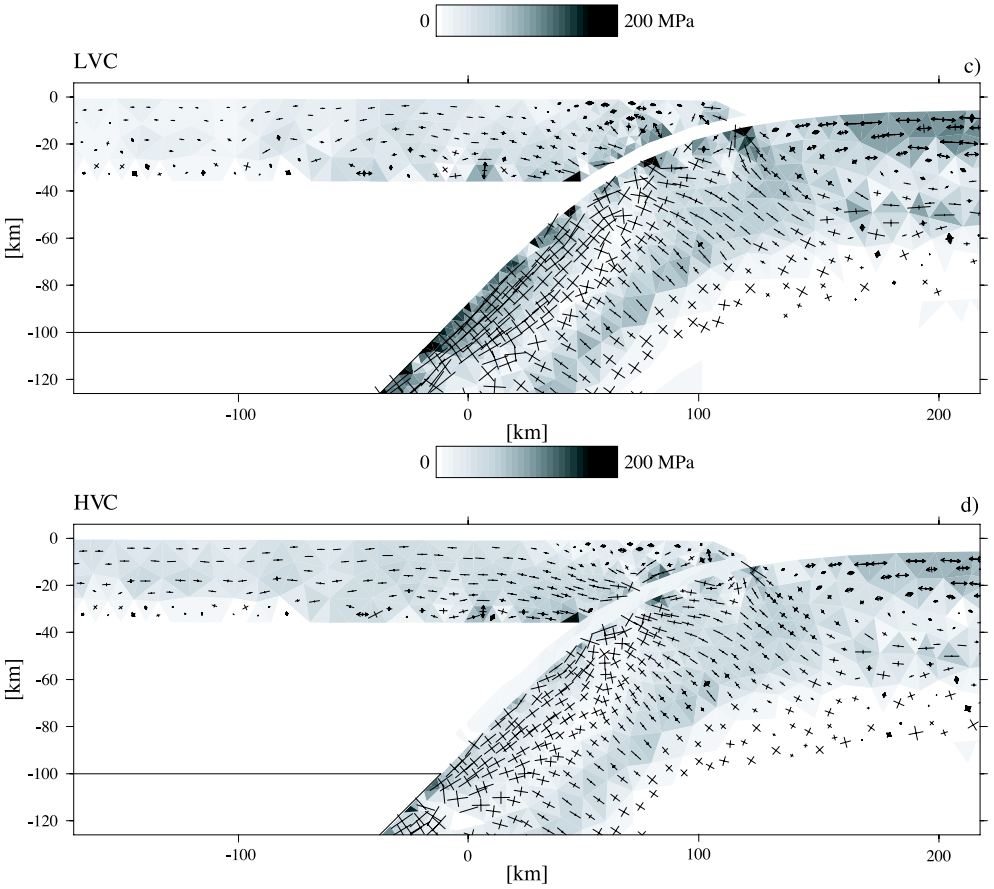

Figure 3.5: (Continued). Effective stress magnitude and principal deviatoric stresses for models with free subduction boundary conditions after 250 Kyr. Tensile stresses are indicated by arrows, compressive stresses by lines. c) Low viscosity channel model (LVC) $\eta = 7 \cdot 10^{17}$. d) High viscosity channel model (HVC) $\eta = 10^{20}$. The black solid line indicates the initial position of the slab.

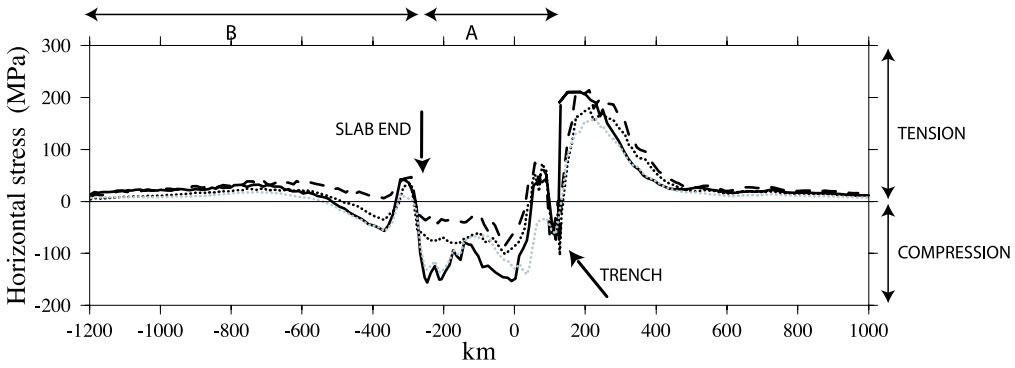

Figure 3.6: Horizontal stress at the free surface of free subduction the models for the entire domain after 250 Kyr. Compression is negative. Solid line represents frictionless fault model (FNF), grey dotted line fault model with friction (FF), black dashed line low viscosity model (LVC), black dotted line high viscosity model (HVC). The arrows indicate the vertical surface projection of the slab end and of the plate contact location. The overriding plate is divided into region A and region B.

Frictional fault subduction zone model (FF)

In our next model we impose a uniform frictional stress of 20 MPa along the fault. The increased coupling results in a reduction of the relative velocity across the subduction zone to 2 cm/yr (Fig. 3.3c). The region close to the plate contact subsides more strongly and region A subsides less (grey dotted line) than in the FNF model (Fig. 3.4b). Relative to the FNF model, velocities in the mantle wedge are reduced. The main difference in the stress field is at the plate contact where compression develops, while the compressive stress in region A decreases (Fig. 3.5b, Fig. 3.6).

Low viscosity subduction channel model (LVC)

In this model we represent the plate contact of the subduction zone by a low viscosity channel ($\eta = 7 \cdot 10^{17}$ Pa·s). The subduction channel is defined along the plate interface from the trench to a depth of 100 km. The convergence velocity is about 7 cm/yr, which is approximately 3 cm/yr higher than in the FNF (Fig. 3.3d and Fig. 3.4a). Velocities in the slab are uniformly plate parallel thus showing a plate like behavior. The velocity in the overriding plate is almost uniformly zero except in the area from the trench to the projected tip of the slab (region A) where the velocity, directed to the left, implies that the trench advances with a velocity of 0.1 mm/yr. Vertical deformation is mostly less than for the FNF model. The trench has deepened to more than 4 km, and is wider. The fore-bulge is less pronounced than in the FNF

model. High velocities are excited in the asthenosphere below the overriding plate. The flow excited in the wedge below the overriding plate is lower than in the FNF model and the subducting plate moves faster than the mantle. Return flow velocities in the asthenosphere under the surface oceanic plate are lower than those in the oceanic plate itself.
In the overriding plate stresses are generally lower than in the FNF, with tension in the region close to the plate contact (see Fig. 3.5c) and a weaker horizontal compression in region A (Fig. 3.6, dashed curve). Tensile stress prevails in the upper plate far field region B (Fig.3.6). Compressive stresses in region A are reduced by 2 orders of magnitude with respect to the FNF model. Horizontal tensile stresses dominate in the surface oceanic plate. The most shallow part of the subduction channel is visible as a zero stress layer between the oceanic slab and the continental crust. Deeper within the slab slab-parallel compression dominates. In Figure 3.6 horizontal stresses are displayed with the dashed curve.

High viscosity subduction channel model (HVC)

The Newtonian viscosity of the subduction channel in this model is $1{\cdot}10^{20}$ Pa·s. The overall response of this model is similar to the LVC model, but there are some differences. The velocity of the subducting plate is reduced to about 4 cm/yr in Figure 3.4a. The vertical displacement is reduced as well relative to the LVC in Figure 3.4b. The trench depth is about 2 km.
The most substantial change occurs in the horizontal stress in the overriding plate (Fig.3.5d and Fig.3.6, region A), which is more compressive. Still, however, stress levels are low compared to the FNF and the FF models.

3.3.2 Land-locked basin subduction

Next we present models with land-locked basin boundary conditions, i.e., where the relative motion between the left and right lithospheric boundaries of the models is zero. Velocity and stress patterns of this models are very similar to the free subduction models in most of our model domain, the main differences are visible at the surface. Therefore, we will subsequently only show the surface expression of horizontal velocity, topography and horizontal stress in Figure 3.7 and Figure 3.8 (more extensive results of these models are presented in the Appendix C).

Frictionless fault subduction zone model (FNF)

As in the previous models the subduction fault is defined along the plate interface from the trench to a depth of 100 km. The solid line in Figure 3.7a displays the

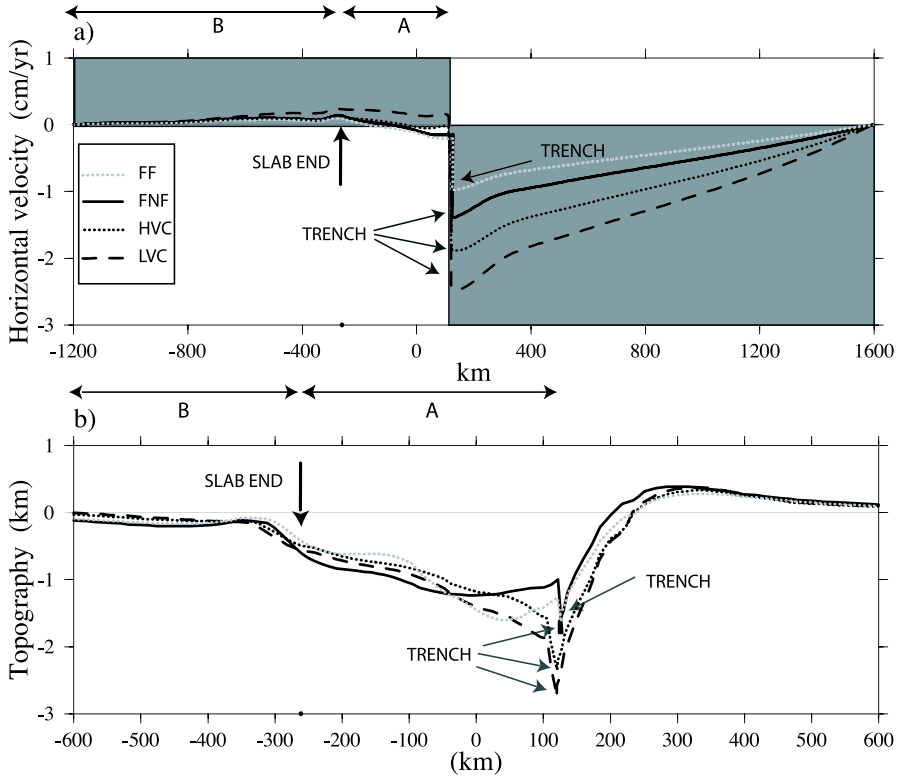

Figure 3.7: Surface expressions for models with land-locked basin boundary conditions. a) Horizontal velocity at the surface of the model for the entire domain: solid curve represents frictionless fault model (FNF), grey dotted curve fault model with friction (FF), black dashed curve low viscosity channel (LVC) model $\eta = 7 \cdot 10^{17}$, black dotted curve high viscosity channel (HVC) model $\eta = 10^{20}$. Velocities in the grey area are directed towards the trench. b) Total vertical displacement at the surface of the model. The vertical arrow indicates the vertically projected tip of the slab. The overriding plate is divided into region A and region B.

horizontal velocity of the free surface for the entire model domain. The trench is visible as a step change at horizontal coordinate 100 km. The velocity of the oceanic plate increases linearly towards the trench. The solid curve in Figure 3.7b shows the total vertical displacement of the free surface. The trench is the deepest point of the curve (2.1 km). A 1 km deep depression has developed on the overriding plate region A. Dynamic uplift of the outer bulge on the oceanic plate is approximately 300 m.

In Figure 3.8, the black line displays the horizontal stress at the free surface for the entire domain. The tensional stresses in the subducting plate (right side) are higher

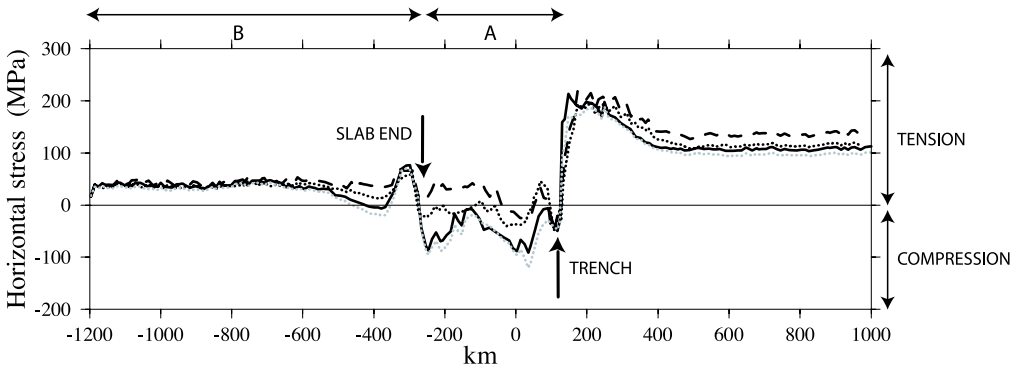

Figure 3.8: Horizontal stress at the free surface of the land-locked subduction models for the entire domain after 250 Kry. Compression is negative. Solid line represents frictionless fault model (FNF), grey dotted line fault model with friction (FF), black dashed line low viscosity model (LVC), black dotted line high viscosity model (HVC). The vertical arrows indicate the vertically projected tip of the slab and of the plate contact location. The upper plate is divided into region A and region B.

than in the previous model (free subduction FNF model). Compression affects region A of the upper plate, but the magnitude of compression is reduced to about half of the value characterizing the free subduction FNF model, with a value of about 50 MPa.

Frictional fault subduction zone model (FF)

In our next model we impose a uniform frictional shear stress of 20 MPa on the fault. The increased coupling results in a reduction of the relative velocity across the subduction zone (Fig.3.7a, grey dotted line). The region of the overriding plate immediately close to trench subsides more strongly than in the FNF model (Fig.3.7b, grey dotted line). The trench has deepened by 1.5 km. Relative to the FNF model, velocities are reduced.
The grey dotted curve in Figure 3.8 shows the horizontal stress at the surface. The stress at the surface, is similar to the one of the FNF model, with compression in region A of the overriding plate. Relative to the FNF model, the overriding plate shows significantly stronger horizontal compression close to the plate contact. Similar to the FNF model, the surface oceanic plate is in horizontal tension.

Low viscosity subduction channel model (LVC)

As in the previous set of models we represent the subduction zone by a low viscosity channel ($\eta = 7 \cdot 10^{17}$ Pa·s). The convergence velocity is higher by approximately

Model name	Plate contact
FNF	frictionless fault model
FF	frictional fault model
LVC	low viscosity channel model
HVC	high viscosity channel model

Table 3.2: Summary of the models used in this study

1 cm/yr than in the FNF model (Fig.3.7a, dashed curve). In the overriding plate the velocity increases moving towards the trench with a maximum velocity in the area from 260 km to the plate contact (region A) of about 3 mm/yr. Subsidence is less than in the FNF model (Fig.3.7b). The trench has deepened to less than 3 km, and is wider.
Stresses in the LVC model are generally different from the FNF and FF models in the overriding plate, in that weak horizontal tension prevails for nearly the entire overriding plate (Fig.3.8, black dashed line regions A and B). Horizontal tensile stresses dominate in the surface oceanic plate with higher stress in the far field region than in the FNF and FF models.

High viscosity subduction channel model (HVC)

The Newtonian viscosity of the subduction channel in this model is $1{\cdot}10^{20}$ Pa·s. The overall response of this model is similar to the LVC model. The velocity of the subducting plate is less than in the LVC but higher than in the FNF and FF models (Fig.3.7a, black dotted line). The most relevant change occurs in the horizontal stress in the overriding plate (Fig.3.8, black dotted line region A), which is slightly compressive rather than tensile as in the LVC. Still, however, stress levels are low in comparison to the FNF and FF. Table 3.2 summarizes all the models used in the previous experiments [2].

3.4 Model analysis

Comparing FNF, FF, LVC and HVC models for free subduction boundary conditions, we notice that the velocity in region A of the overriding plate is oriented in the same direction as in the subducting plate for all models. For the FNF model the magnitude of this velocity is higher than for all the other models. In the land-locked basin

[2] This table has been inserted after publication

FNF model, the upper plate moves away from the trench, while in the LVC model the displacement direction is towards the trench. The FF and HVC models have an intermediate behavior. When the overriding plate moves in the same direction as the subducting plate, a compressional regime develops in region A (e.g., Fig.3.6). On the other hand, when the velocity is directed towards the plate contact, in the LVC land-locked basin setting, the regime in region A becomes tensional. This was also found by Heuret & Lallemand (2005). The fact that they fix the subduction hinge with respect to the upper plate edge does not change the relevance of their result. Our results indicate that the different velocity distributions, arising from different states of the plate contact, cause different stresses in FNF, FF, LVC and HVC. The question is why the velocity changes from one model to the other. In the setup of our experiments, the negative buoyancy of the subducted lithosphere with respect to the surrounding mantle is the primary driving force. This holds for all models. The secondary forces which play a role are the suction force, which acts at the plate interface and makes the plates interdependent (Bott et al., 1989; Whittaker et al., 1992), the force due to the bending of the lithosphere and, frictional force in the models where friction is present (Fig.3.9). These forces result in a state of stress in the lithosphere, which we characterize by the Response Force that we define as the difference between horizontal and vertical stress integrated with depth through the lithosphere. We calculate it at the left edge of the continental plate. The boundary conditions, applied at this edge (locked: zero horizontal displacement), do not affect the overall response of the model because they are far enough from the trench. This is proven by the fact that tension develops in the far field of the plate even though compression dominates in region A (e.g., Fig.3.8). Now we consider just the two end members of our models, the FNF model and the LVC models. LVC is characterized by a stronger Response Force than the FNF model. The force magnitude increases from $2.2 \cdot 10^{12}$ N/m in the FNF to $2.9 \cdot 10^{12}$ N/m for LVC, respectively.

In the FNF model, the suction force is intrinsic in the fault description, since the normal stress and velocity are continuous at the fault and the two plates are fully coupled in that direction. The normal components of the forces, which act at the fault are transmitted from one plate to the other. The Response Force is the result of such normal continuity. When the fault is frictional (FF model) the overall response of the model is the same. The presence of friction develops compressive stresses along the plate contact and a compressive forearc region; clearly, the speed of subduction is reduced.

In the LVC model - and in general in any channel model (also in HVC model) - the nature of the Response Force is different. The channel, with its weak material, reduces the transmission of stresses between the plates, e.g., the bending stress. Moreover, the low coupling between the plates increases the net downward force acting on the

subducting plate. Shemenda (1993) showed that the interplate pressure is inversely proportional to the slab pull. As a consequence, the increase of slab pull decreases such a pressure. Shemenda (1993) and Chemenda et al. (2000)[3] proved that a low interplate pressure reduces compression of the overriding plate or it produces extension. In Figure 3.9 the main forces in the process are summarized.
Several aspects in the dynamic response of the models are worth noticing. First, in the free subduction LVC and HVC the velocity magnitude of the overriding plate is reduced relative to the FNF and FF models. In the FNF and FF models the forces are fully transmitted at the plate contact pushing the overriding plate towards the left. In the LVC and HVC the lower transmission of forces through the plate interface reduces such a push and as a consequence the compressive regime. Second, the velocity of the slab is faster in the LVC and HVC than in the FNF and FF models. Third, the velocity field in the slab is more slab parallel in the LVC and HVC models than in the FNF and FF models. In the land-locked basin LVC subduction model the roll-back of the slab, in addition to the stronger net slab pull, makes the overriding plate advance. A higher channel viscosity (HVC) reduces the trench-ward velocity of the overriding plate and increases the compressive stress in the fore-arc region. This is a direct consequence of the increase of friction and transmission of stress from one plate to the other, and of the increase of the interplate pressure.
As the subduction velocity is generally lower in the FNF model than in the LVC model, it is understandable that the magnitude of the excited Response Force is less. To show that the plate boundary type, rather than the subduction velocity, determines the stress field and the amount of subsidence of the overriding plate, we consider two new models involving a FNF and a LVC type of plate contact. Now, the subducting plate is driven by velocity boundary conditions which are applied on the slab and on the right boundary of the oceanic lithosphere. The continental plate is again fixed on the left end side. In Figure 3.10) at the top, the horizontal velocity at the surface of the model is displayed. The FNF model (solid line) is characterized by a retreating upper plate, while in the LVC model (dashed line) the plate is close to stationary. In Figure 3.10, the central panel shows the total vertical displacement. Subsidence is stronger on the overriding plate of the FNF model (solid line) than the LVC model (dashed curve). At the bottom, the horizontal stresses are displayed: in region B of the upper plate both models show the same amount of compression; in part of region A of the FNF model compression is dominant, whereas in the LVC model the compressive stresses are reduced by about 70%.
In the FNF model, the only force perpendicular to the fault is caused by the bending of the slab, the stresses generated are completely transmitted to the overriding plate at the shallow part of the fault, causing the retreat of the upper plate. In the channel

[3]This reference has been added after publication

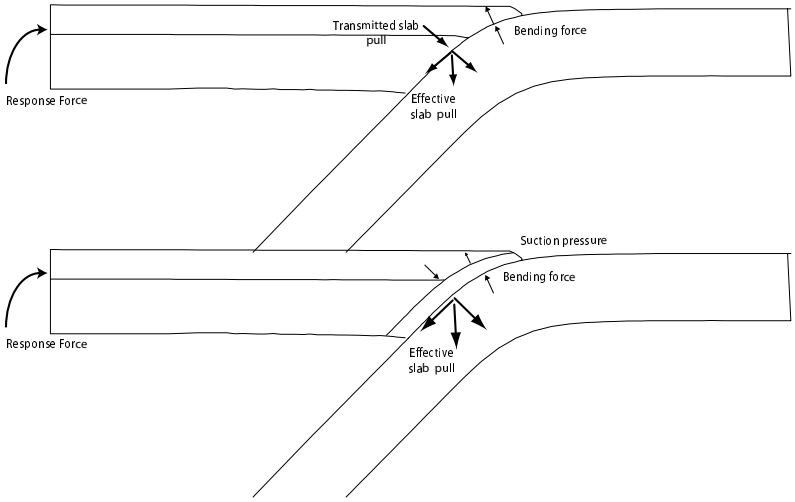

Figure 3.9: Top. Schematic sketch of forces acting at the fault, with the traction felt by the overriding plate as response to the bending stress and the traction due to the normal component of the gravitational force. The arrows represent the forces that are equal at both sides of the fault. Bottom. Forces acting in the channel model. The tractions are less transmitted, the net slab pull acting on the subducting plate is more than in the FNF model. On the left side it is indicated where the Response Force is measured.

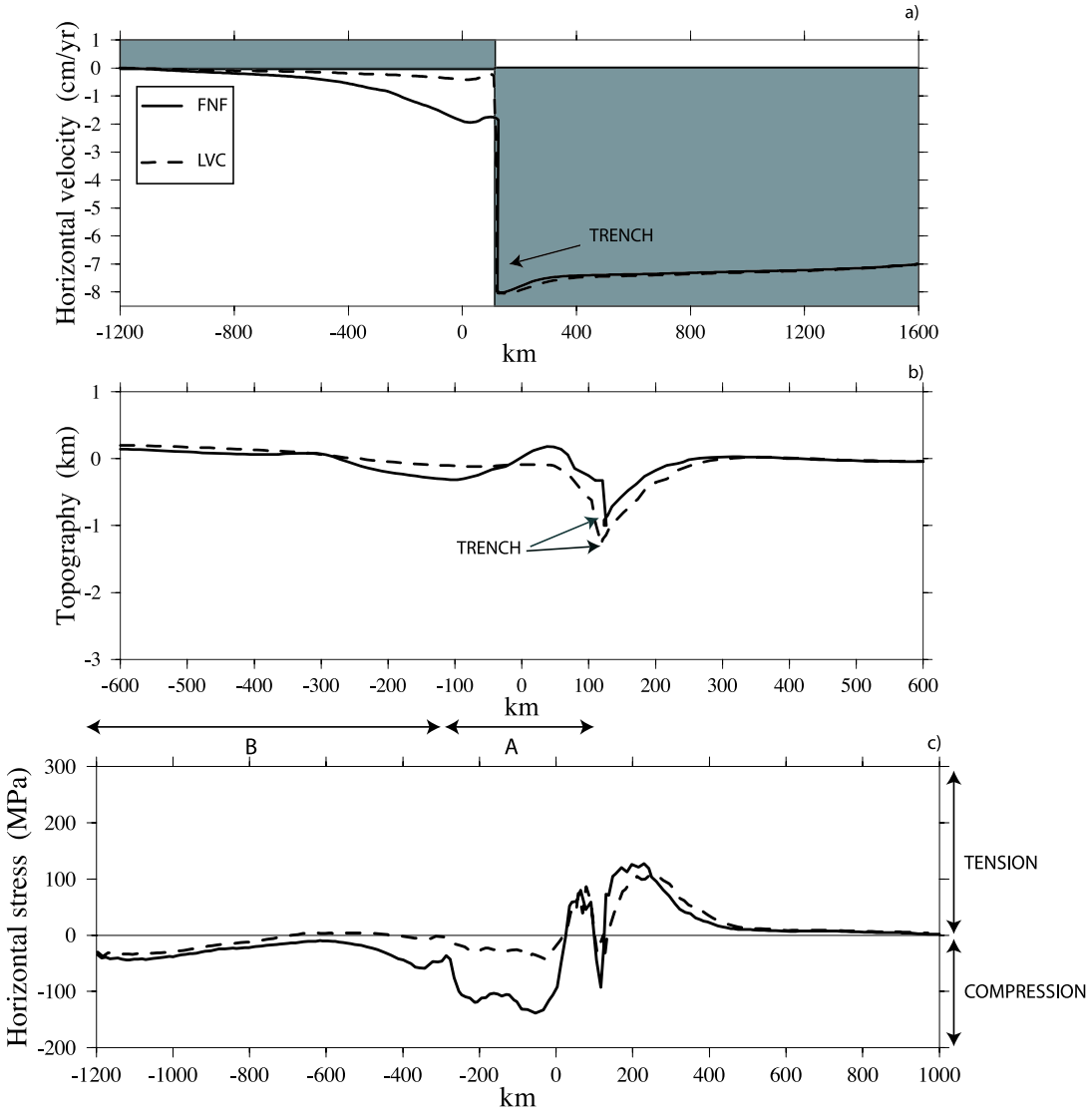

Figure 3.10: Surface expression of velocity driven models at the free surface. Solid curve represents the frictionless fault model (FNF) and the dashed curve the low viscosity channel model (LVC). a) Horizontal velocities. Velocity in the grey area are directed towards the trench. b) Total vertical displacement. The deepest point is the trench location. c) Horizontal stress. Compression is negative.

models, the reduced transmission of the bending stresses and of the slab pull result in less subsidence close to the plate, less retreat, less down-welling and lower compressive stress. In the land-locked basin FNF model the compression in the overriding plate above the dipping slab outweighs the tension produced by slab roll-back so that a net compressive stress persists into the back-arc region. The horizontal compressive stresses and the down-welling are due to the fact that the overriding plate retreats.

The land-locked basin LVC produces tension in region A, even though the amount of slab roll-back is less than in the FNF model (see Appendix C Fig3.12a and Fig.3.12c). In the free subduction setup the compressive regime is reduced relative to the FNF model as well as the down-welling.

On the basis of our numerical models, we conclude that the nature of the plate contact is a primary controlling factor in developing or not developing back-arc extension. The type of plate contact controls the dynamic response of the upper plate, drives the displacement of the overriding plate and as a consequence the stress distribution. Comparing fault and channel models, we conclude that the subduction channel reduces the compression in the region of the overriding plate above the slab, in a convergent tectonic setting (e.g., free subduction and kinematically driven model). The subduction channel - if the rheology is weak enough (e.g., LVC) - produces tension in a land-locked basin setting. The fault model, however, results in a compressive regime, even with a larger amount of slab roll-back than in the channel model.

Many numerical studies have been carried out on subduction process behavior (e.g., van Hunen et al. (2000), Kincaid & Hall (2003), Funiciello et al. (2003), Hampel & Pfiffner (2006)). In this section we compare our models with the ones that are more closely related to our study, and we investigate, in a similar set-up, the same kind of observed parameters. Whittaker et al. (1992) used both locked and unlocked fault plate contact. The model with a locked fault showed results similar to our frictional model: compression was developed in the overriding plate close to the trench and in the back-arc region and the displacement displayed a broad down flexure at the surface above the slab. However, their unlocked model showed a different behavior compared to our FNF model. They obtained tension in the overriding plate. We can trace two reasons. First, the fault extends until the end of the slab (in our model the fault is just at the contact between the two plates); in this way less asthenosphere was dragged down, reducing the down-welling of the lithosphere. Second, the continental crust in their model was 400 kg/m^3 lighter than the surrounding mantle, which resulted in tensile stress regime of the overriding plate. So, their continental crust contributed to the forcing.

Comparing our model with the model of Giunchi et al. (1996) in which the fault is located just along the plate contact (their Locked model), we find both similarities and

differences. The horizontal velocities showed the same pattern: the overriding plate retreated in the region close to the plate contact, but the magnitude in the subducting plate was lower in their model. This is due to the boundary conditions that are farther from the trench in our models. The vertical velocity showed a pattern comparable to our vertical displacement. The total velocity distribution displayed similar features, with the overriding plate moving in vertical direction and a strong near horizontal flow in the mantle. Their stress distribution, with the overriding plate in compression and very small stresses close to the plate contact, is also comparable to ours. It is interesting to notice that as soon as they unlocked the fault down to the end of the slab, the overriding plate started to move towards the trench and the horizontal compressive stresses became negligible. Overriding plate tension in their model was caused by two factors; the zero friction along the entire slab top surface reduced the drag of the asthenosphere and of the above lithosphere, and the dip angle which is 70^0 in their model. This steep angle leads to a stronger suction force causing tension in the overriding plate. Zhong et al. (1998) found that, when a curved fault of 100 km depth and a dip angle of about 45^0 was introduced at the contact between overriding and subducting plate, the upper plate was affected by horizontal compression. This is in agreement with our FNF results.

3.5 Discussion

In previous studies, different hypotheses have been proposed in order to explain what governs the stress regime in the upper plate. Some classical theories are: 1) back-arc extension driven by roll-back caused by negative buoyancy of the slab which is a function of the age of the slab (Elsasser, 1971; Molnar & Atwater, 1978; England & Wortel, 1980; Faccenna et al., 2001; Hall et al., 2003; Schellart et al., 2003); 2) back-arc extension driven by absolute motion of the overriding plate (Chase, 1978; Scholz & Campos, 1995). Observed evidence does not support any of the hypotheses completely (Lallemand et al., 2005; Sdrolias & Muller, 2006). For the tectonic settings under investigation, our models show that the velocity of the upper plate and the stress distribution of part of the upper plate are driven by the dynamic response of the subduction zone to the combination of suction force, transmission of bending stress and gravity. The dynamic response was measured at the edge of the upper plate, resulting in what we called Response Force. The LVC increases the magnitude of Response Force and produces tension even with a small amount of slab roll-back. As a consequence, although roll-back is required as a underling mechanical process, there is not a one-to-one relationship between roll-back and stress regime. The type of plate contact plays a decisive role in controlling back-arc state of stress. These findings give a new insight in the mechanisms controlling the stress regime of the

overriding plate.

This study has taken a step in the direction of defining the relations between plate contact type and stress regime of the overriding plate. However, there are some left problems to be addressed in relation to the subduction channel. As pointed out by Eberhart-Phillips & Martin (1999), large thrusting events have been recorded near the plate interface where LVC are present, e.g., subduction of the Hikurangi Plateau. How to explain these events arising from the presence of the LVC, that is characterized by a weak rheology? We think that, during evolution of a subduction zone, the interface can change from a plate contact like channel to a fault and vice-versa. A very critical factor, as pointed out by Cloos & Shreve (1988) is the sediment supply; if the channel is thick, or has a very low viscosity, the average shear stress is relatively low. Then thrust earthquakes are more likely to occur when the channel is so thin that it mechanically acts like a fault. Another possibility is that asperities in the channel, such a sea-mounts, may be sites of concentrated seismic activity (Ruff & Kanamori, 1983).

One limitation of our model is that the slab hangs from the top implying that the most of the slab weight is supported by the plates. We expect to obtain different results using a slab that is largely supported from below, i.e., a slab reaching the 670 km discontinuity.

In this study, the numerical experiments are limited to free subduction and land-locked basin subduction, in both cases the overriding plate is locked. This derives from our starting point only to consider the cases where the forcing occurs within our model domain. As a consequence, however, our models do not encompass the entire range of tectonic settings; for instance, we did not consider the case of an overriding plate that is actively driven towards the trench by forces outside the model domain. Surely, our conclusions about the stress regime in the overriding plate will be affected by such boundary push or pull. For instance, if the overriding plate is actively driven towards the trench, it may mask the signature of back-arc extension. We did not investigate the influence of the slab age; this is based on the fact that the age-dependent slab pull force contributes either slightly or not at all to slab roll-back that could explain back-arc extension (Lallemand et al., 2005). We need to point out that in our dynamic models we neglect domain-internal ridge push in order to isolate the subduction effect. This force is present in most of the edge plates and could influence the stress distribution within the plates. In the kinematically driven model, where we imposed ridge push through velocity boundary conditions, compression affects the entire overriding plate for both FNF and LVC. However, the amount of compression is strongly reduced by the presence of the LVC. Thus, we argue that, even in a convergent tectonic setting, the different response due to presence of the LVC is well recognized.

The LVW above the slab reduces the link between the overriding plate and the sinking slab. This feature makes it difficult to distinguish, in the surface response, between the contribution of such weak region and the flow generated by the eddies in the mantle. However, this does not affect our conclusions, in which we want to establish the differences due to the two types of plate contact using the same type of tectonic setting and forces.
Another limitation is that we did not investigate alternate subduction geometries; the influence of slab dip or different radius of curvature of the plate contact. We speculate that these parameters do not change our general conclusions, because, even though the results may be affected by them - e.g., the dip angle is correlated to the stress regime of the overriding plate - the response of the subduction process is intrinsically related with the type of plate boundary. Thus, comparing FNF and LVC for different kinds of geometry or rheology, we will anyway observe different signatures. This is due to the fact that FNF and LVC represent different physical states of the subduction plate contact.

3.6 Conclusions

Based on a consistent comparison of fault and channel numerical models, we conclude that the nature of the plate contact is one of the controlling factors in developing or not developing back-arc extension. Our results indicate that the different dynamic response in the overriding and subducting plate, arising from the state of the plate contact, causes different velocities and stresses in fault models and channel models as summarized below:

1. if the subducting plate is free to move in horizontal direction (i.e., free subduction), the fault models are characterized by: 1) subsidence of the overriding plate above the slab; 2) imperfect plate like behavior of the subducting plate; 3) motion of the overriding plate away from the trench; 4) compression of the back-arc region ranging between the trench and the vertically projected tip of the slab. Specifically, when friction is present at the fault, subduction velocities are reduced, and subsidence of the overriding plate region close to the plate contact is more developed.

   Relative to the fault models, the channel models are characterized by: 1) less vertical deformation, therefore the subsidence is reduced; 2) faster subduction and a more plate like motion; 3) less motion of the overriding plate away from the trench, due to the combination of suction force and the low transmission of stress between the plates; 4) lower compressive stresses in the overriding plate region ranging between the trench and the vertically projected tip of the slab.

2. If no relative motion between the far field of the two plates is allowed (i.e., land-locked basin setting), the fault models are characterized by: 1) subsidence of the overriding plate; 2) motion of the overriding plate away from the trench; 3) back-arc compression of the upper plate in the region between the trench and the vertical projected tip of the slab. Slab roll-back does not produce tension in this region, but tension is generated in the far field region of the overriding plate.

   Again relative to the fault models, the channel models are characterized by: 1) reduced subsidence of the upper plate; 2) faster subduction velocity; 3) upper plate moving towards the trench; 4) tension in the entire upper plate for low viscosity channel model and lower compression in the region of the overriding plate above the slab for high viscosity channel model. This shows that even though slab roll-back is less developed than in the fault model, tension may result in the entire overriding plate of our model

We conclude that, the type of plate contact plays a decisive role in controlling the back-arc state of stress. To obtain back-arc extension, roll-back is required as an underlying geodynamical process, but it is not always a sufficient condition.

3.7 APPENDIX B: Finite element equation for diffusion-advection equation

The partial differential equation (PDE) for the convection-diffusion problem including the sources is:

$$\nabla\cdot(k\nabla T) + g - \rho C_p \mathbf{v}\cdot\nabla T = 0, \tag{B-1}$$

where *k* denotes the diffusivity, *T* denotes the temperature, *g* denotes the heat production, ρ denotes the density, C_p denotes the specific heat at constant pressure, $\mathbf{v}$ denotes the given velocity vector.
We rewrite the equation above through the finite element formulation in the Standard Galerkin Approach (SGA). The SGA is based on the weak formulation of equation(B-1). This formulation arises by multiplication of the differential equation by the test function, which in our case is the shape function and afterwards integration over the domain. The equation(B-1) becomes:

$$\int_{V^{(e)}} N_i \left[\frac{\partial}{\partial x}\left(k_x\frac{\partial T^{(e)}}{\partial x}\right) + \frac{\partial}{\partial y}\left(k_y\frac{\partial T^{(e)}}{\partial y}\right) + \frac{\partial}{\partial z}\left(k_z\frac{\partial T^{(e)}}{\partial z}\right)\right] dV \tag{B-2}$$

$$+\int_{V^{(e)}} N_i g dV - \int_{V^{(e)}} \rho C_p N_i \left[v_x^{(e)}\frac{\partial T^{(e)}}{\partial x} + v_y^{(e)}\frac{\partial T^{(e)}}{\partial y} + v_z^{(e)}\frac{\partial T^{(e)}}{\partial z}\right] dV = 0 \tag{B-3}$$

where $V^{(e)}$ is the element volume, and $T^{(e)} = \sum_{j=1}^{NEN} N_j T_j$ is temperature in the element, NEN is the nodes element numbers. N_j are shape functions prescribed in terms of independent variables and all or some of the parameters T_j are unknown. Element velocities derive from the same interpolation function, i.e., $v_x^{(e)} = \sum_{j=1}^{NEN} N_j v_j^x$ and so on, where $\hat{\mathbf{v}}_j = (v_j^x, v_j^y, v_j^z)$ is the velocity vector at node j. In a concise form equation (A2) is:

$$\mathbf{KT} = \mathbf{P}, \tag{B-4}$$

where $\mathbf{K}$ is the stiffness matrix and $\mathbf{P}$ is the right-hand side vector. Following partial integration (i.e., using Gauss' divergence theorem) and ignoring surface integral - surface integral of neighboring elements are assumed to cancel after assembly- we obtain the expression for the stiffness matrix:

$$K_{ij}^{(e)} = \int_{V^{(e)}} \left(k_x\frac{\partial N_i}{\partial x}\frac{\partial N_j}{\partial x} + k_y\frac{\partial N_i}{\partial y}\frac{\partial N_j}{\partial y} + k_z\frac{\partial N_i}{\partial z}\frac{\partial N_j}{\partial z}\right) dV \tag{B-5}$$

$$+\int_{V^{(e)}} \rho C_p N_i \left(v_x^{(e)}\frac{\partial N_j}{\partial x} + v_y^{(e)}\frac{\partial N_j}{\partial y} + v_z^{(e)}\frac{\partial N_j}{\partial z}\right) dV$$

3.7.1 Streamline upwind Petrov-Galerkin method

The above SGA behaves like a central difference scheme. For large Peclet numbers, central differences behave notoriously poor (e.g., Patankar (1980). In the finite difference and finite volume literature, upwind techniques have successfully been employed to remedy this. Segal (1993), based mostly on the work of Brooks & Hughes (1982), summarizes the streamline upwind Petrov-Galerkin (SUPG) method for finite elements. As in SGA, SUPG uses the weak formulation, with the difference that the weighting functions are chosen differently:

$$M = N + Q, \tag{B-6}$$

where *N* is the classical shape function, and *Q* is a correction that takes care of the upwinding part. *N* is a continuous function while *Q* is allowed to be discontinuous over element boundaries. For this reason the Gauss divergence theorem can be applied just to *N* part.
A common choice for the function *Q* is inspired by the one-dimensional stationary convection-diffusion equation without source terms:

$$\rho C_p \mathbf{v} \cdot \nabla T = \nabla \cdot (\mathbf{k} \nabla T) \tag{B-7}$$

The standard first order finite difference upwind scheme for the equation above may be considered as the central difference scheme corresponding to the equation

$$\rho C_p \mathbf{v} \cdot \nabla T = \nabla \cdot ((k + \hat{k}) \nabla T), \tag{B-8}$$

where $\hat{k}$ is called the artificial diffusion tensor. In the streamline-upwind method, In order to avoid inaccuracies, artificial diffusion acts only in the direction of the flow. To that end, $\hat{k}$ is parameterized as

$$\hat{k}_{ij} = \bar{k} \hat{v}_i \hat{v}_j \qquad \hat{v}_i \equiv \frac{v_i}{||v||} \qquad \hat{v}_j \equiv \frac{v_j}{||v||} \qquad ||v||^2 \equiv v_i v_i.$$

The value of $\bar{k}$ follows from summing the convective central difference term and the artificial diffusion term and assuming that this sum corresponds to the difference upwind scheme of the convective term.
The next step is to construct a function Q such that an artificial diffusion term is created, in order to do that is sufficient to choose the component Q_i equal to

$$Q_i \equiv \frac{\bar{k}}{\rho C_p ||v||^2} \hat{v}_m \frac{\partial N_i}{\partial x_m}. \tag{B-9}$$

Classical, or pure, upwinding in more dimensions results in

$$Q_i = \bar{D}\,(v \cdot \nabla N_i) \qquad \bar{D} \equiv \frac{h_m |v_m|}{2||v||^2},$$

h_x, h_y and h_z are element sizes in the x, y and z-direction, respectively. However, pure upwind results in overly diffusive solutions. Therefore a optimizing contributions of (underdiffusive) central differences and (overdiffusive) upwind differences is used (Brooks & Hughes, 1982). Introducing directional weighing functions ξ_x, ξ_y and ξ_z, Q_i is modified w.r.t. the above definition;

$$\bar{D} \equiv \frac{h_m |v_m| \xi_m}{2||v||^2}. \tag{B-10}$$

In G-TECTON the Mizukami scheme is used that is an extension of the above formulation for triangles (Mizukami, 1985). Weighting functions are functions of directional Peclet numbers

$$(\xi_x, \xi_y, \xi_z) = (f\left(\frac{v_x h_x}{2\kappa}\right), f\left(\frac{v_y h_y}{2\kappa}\right), f\left(\frac{v_z h_z}{2\kappa}\right)), \tag{B-11}$$

where κ is the thermal diffusivity. The following choices of $f(\alpha)$ are commonly proposed:

Classical upwind scheme f(α) = sign(α)
Optimal upwind scheme f(α) = coth (α) - $1/\alpha$

$$\text{Double asymptotic approximation f}(\alpha) = \begin{cases} \alpha/3 & -3 \le \alpha \le 3 \\ \text{sign}(\alpha) & \alpha > 3 \end{cases}$$

$$\text{Critical approximation scheme f}(\alpha) = \begin{cases} -1 - 1/\alpha & \alpha \le -1 \\ 0 & -1 \le \alpha \le 1 \\ 1 - 1/\alpha & \alpha \ge 1 \end{cases}$$

SUPG results in a modified stiffness matrix

$$K_{ij}^{(e)} = \int_{V^{(e)}} \left(k_x \frac{\partial N_i}{\partial x}\frac{\partial N_j}{\partial x} + k_y \frac{\partial N_i}{\partial y}\frac{\partial N_j}{\partial y} + k_z \frac{\partial N_i}{\partial z}\frac{\partial N_j}{\partial z}\right) dV \tag{B-12}$$
$$+ \int_{V^{(e)}} \rho C_p \left(N_i + Q_i\right) \left(v_x^{(e)} \frac{\partial N_j}{\partial x} + v_y^{(e)} \frac{\partial N_j}{\partial y} + v_z^{(e)} \frac{\partial N_j}{\partial z}\right) dV$$

The second term destroys the typical symmetry of the stiffness matrix, and necessitates us to use a different solver. Here we choose the generalized minimum residual

Krylov subspace method as implemented in the PETSc package (Balay et al., 2002; http://www-unix.mcs.anl.gov/petsc).
The resulting element load vector

$$P_i^{(e)} = \int_{V^{(e)}} g\left(N_i + Q_i\right) dV - \int_{S^{(e)}} q_n N_i dS \tag{B-13}$$

Extensive testing of the implementation showed that the it performs very well for incompressible flow fields. One particularly tough and successful test (more difficult than probably ever encountered in earth science applications) is the high Peclet number circular rotation test (Brooks & Hughes, 1982).

3.8 APPENDIX C: Land-locked basin setting

In this section we present the complete results for the land-locked basin models. We show the total velocity and stress distribution. Figure 3.11a shows the velocity distribution for the frictionless subduction FNF model. Slab pull forces drive a primarily vertical down-welling close to the slab. Eddies are created at the two end sides of the slab. In the oceanic lithosphere, motions are mostly horizontally directed towards the plate contact region. Horizontal return flow dominates in the deeper mantle beneath the slab. Velocity patterns of the different subduction zone models are very similar in most of our model domain, except near the plate contact zone where there are important differences. Therefore, we will subsequently zoom in on this region.

Figure 3.11b is a blow-up of the subduction zone region of Figure 3.11a. Velocities are oriented towards the trench in the surface oceanic plate, reaching a maximum of about 1.5 cm/yr near the trench. Velocities in the slab are oriented towards the direction perpendicular to the slab. In the overriding plate, velocities are small (2 mm/yr maximum) and are directed towards the trench on the left side of the figure (from -260 km). Closer to the plate contact (and to the down-welling), velocities in the crust of the overriding plate are small also, but near-vertical. Slab sinking excites the highest velocities in the mantle wedge. The magnitude of return flow beneath the oceanic plate is similar to the near-trench velocity of the oceanic plate itself.

Figure 3.12a shows principal stresses as arrows and effective stress magnitudes as grey contour. In the overriding plate, horizontal stress is compressive in the crust.

Horizontal tensile stresses dominate in the shallow surface oceanic plate. Deeper down, horizontal stresses are slightly compressive. Zero friction at the plate contact can be seen from principal stresses that are oriented perpendicular and parallel to the interface. Fault normal stresses are negligible along the shallowest portion of the plate subduction zone, and slightly compressive at the interface with the deepest portion of the overriding crust. Significant fault normal compressive stresses develop in the slab near the tip of the subduction fault. As discussed earlier for the free subduction models, stresses within the slab do not show the typical signature of elastic bending, i.e., tensile slab parallel stresses in the shallowest part and compressive stresses deeper down. Small down-dip tensional stresses are visible in the slab. Stresses are low in the low-viscosity mantle wedge and beneath the oceanic surface plate. The solid line in Figure 3.12a shows the initial position of the slab. The dip angle steepens by about 4^o.

In the FF model, velocities in the (deeper) slab are somewhat affected, showing both a deceleration and a rotation towards more slab perpendicular motion (see Fig.3.11b). Relative to the FNF model, velocities, in particularly the mantle wedge, are reduced. Return flow velocities are higher beneath the surface oceanic plate than within it.

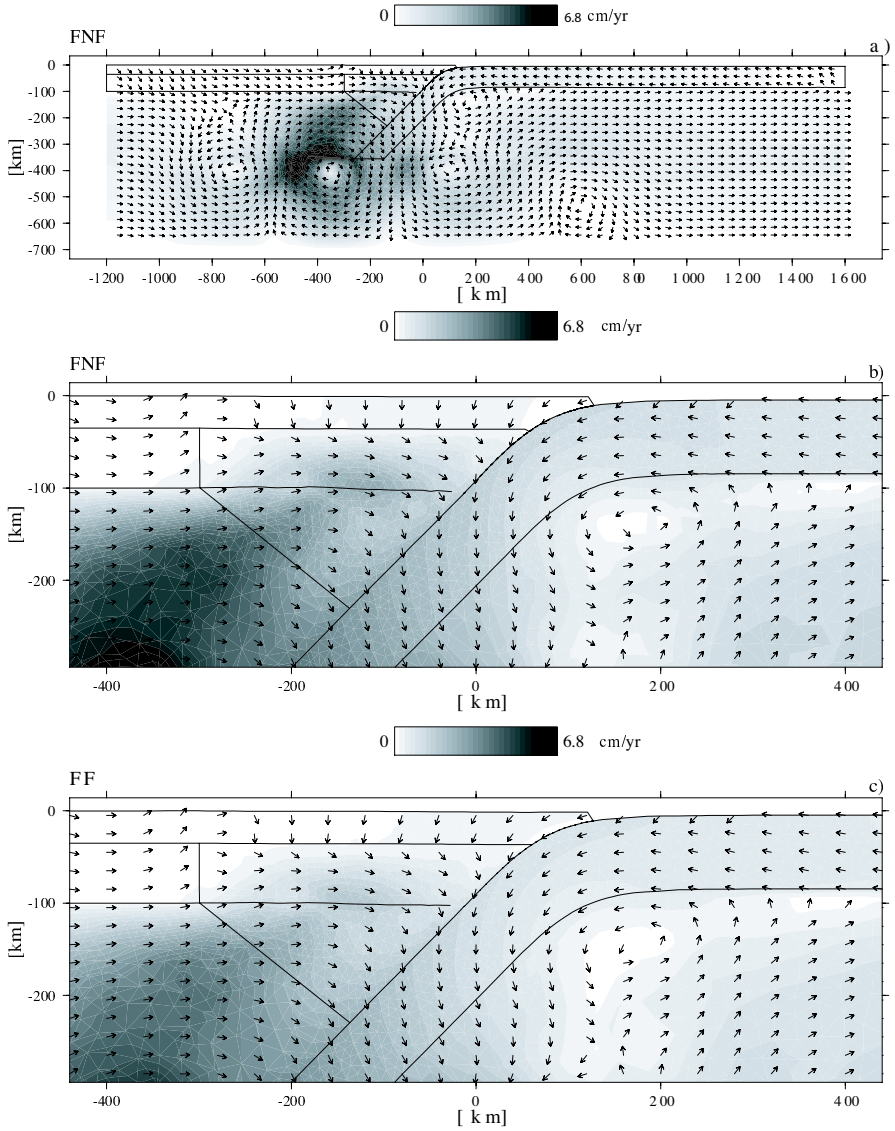

Figure 3.11: Velocity field for land-locked basin models. a) Frictionless fault model (FNF) total view of the model domain, b) FNF enlarged from a), c) fault model with friction (FF). Note that arrows indicate directions only; arrows are not scaled by velocity magnitude. Velocity magnitude is indicated with the gray scale contours. The solid lines outline the overriding, subducting plate and the LVW.

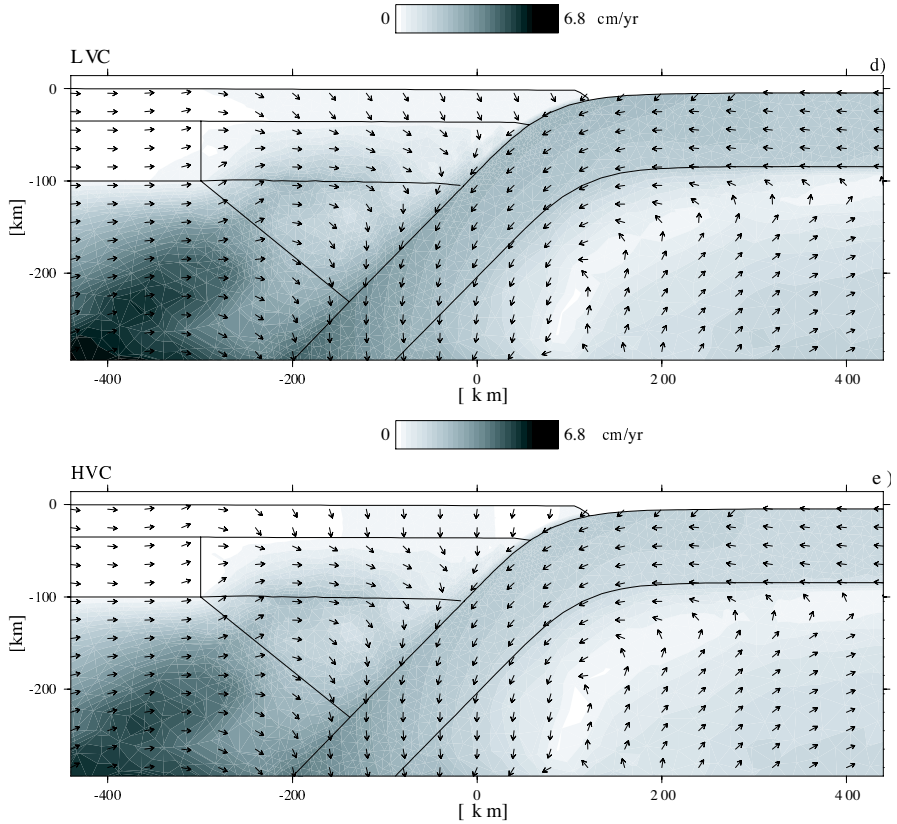

Figure 3.11: (Continued). Velocity field for land-locked basin models. d) Low viscosity channel model (LVC) $\eta = 7 \cdot 10^{17}$. e) High viscosity channel model (HVC) $\eta = 10^{20}$. Note that arrows indicate directions only; arrows are not scaled by velocity magnitude. Velocity magnitude is indicated with the gray scale contours. The solid lines outline the overriding, subducting plate and the LVW.

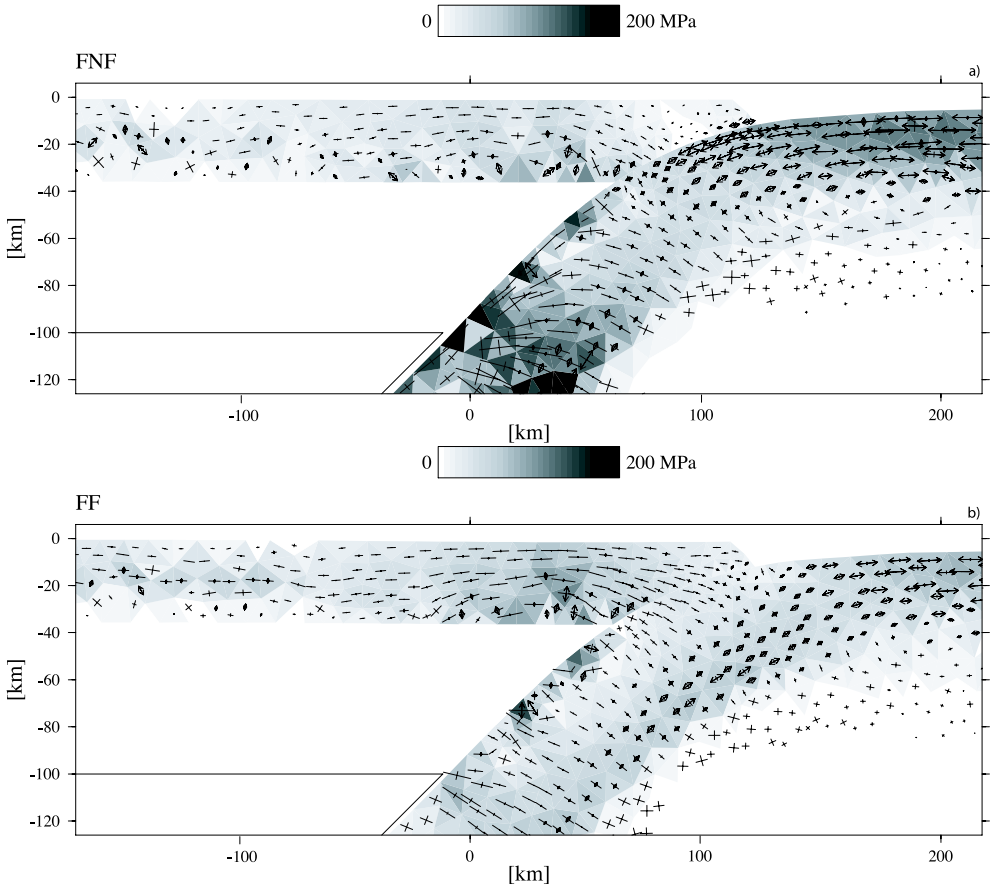

Figure 3.12: Effective stress magnitude and principal deviatoric stresses for the land-locked basin model. Tensile stresses are indicated by arrows, compressive stresses by lines. a) Frictionless fault model (FNF). b) Fault model with friction applied at the fault (FF). The solid line indicates the initial geometry

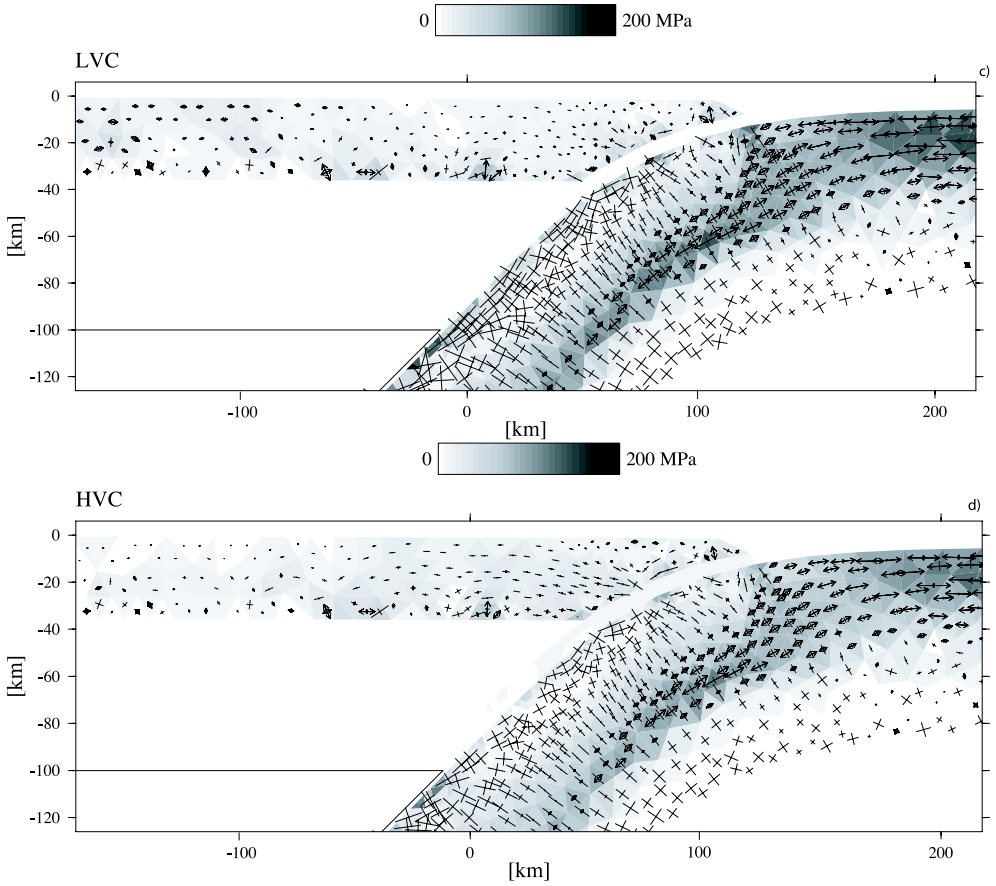

Figure 3.12: (Continued). Effective stress magnitude and principal deviatoric stresses for the land-locked basin model. Tensile stresses are indicated by arrows, compressive stresses by lines. c) Low viscosity channel model (LVC) $\eta = 7 \cdot 10^{17}$. d) High viscosity channel model (HVC) $\eta = 10^{20}$. The solid line indicates the initial geometry

Figure 3.12b shows deviatoric stresses for the FF model. Relative to the FNF model, the overriding plate shows significantly stronger horizontal compression close to the plate contact. At the plate contact the principal stresses are rotated with respect to the fault. Similar to the FNF model, the surface oceanic plate is in horizontal tension. Down-dip tensile stresses occur deeper down in the curved portion of the slab.
In the LVC model, velocities are more plate parallel in the curved portion of the slab than in the FNF and FF models, and near-vertical in the deeper part (see Fig.3.11c) The highest velocities are excited in the asthenosphere below the overriding plate. Flow velocities in the mantle region below the overriding plate, are lower than in the FNF model. Return flow velocities in the asthenosphere under the surface oceanic plate are lower than in the oceanic plate itself.
The shallowest part of the subduction channel is visible as a zero stress layer between the oceanic slab and the continental crust. Compressive stresses in the slab are roughly parallel to its top surface. Deeper within the slab down-dip tension and slab-normal compression dominate. The slab dip changes less than that in the FNF, by about 2^o (see Fig.3.12c).

Chapter 4

Dynamics of continental collision: Influence of the plate contact

Observations shows that continental collision may evolve in different ways, resulting in a wide range of tectonic responses. In search of the controlling conditions and parameters, we start from the results of our previous work which demonstrated that the properties of the plate contact are important for the overall dynamics of convergent plate margins. Two fundamental types of subduction plate contact can be distinguished: one based on a fault and the other based on a weak subduction channel. In this study, we investigate how the plate contact affects the initial stage of continental collision. We use a finite element method to solve the heat and the time dependent momentum equations for elastic, (power law) viscous and plastic rheologies. For the same rheological properties and driving forces, varying the nature of the plate contact leads to three types of responses. The presence of a subduction channel promotes coherent and, when the boundary conditions allow it, plate-like subduction of the continental margin. In models with a subduction fault, coherent subduction of the incoming continental lithosphere occurs when the colliding passive margin has a gentle slope. The approaching continental sliver starts to subduct and the subduction is characterized by a non-plate-like behavior, slower subduction velocity than in channel models and strong slab deformation. If the continental margin is steep and the strength of the incoming continental crust is high, fault models result in locking of the trench, eventually leading to slab break-off. If the crustal strength is relatively low, shear delamination of part of the crust is expected. In the channel model this

This chapter has been submitted for publication in *Geophysical Journal International* as: R. De Franco, R. Govers and R. Wortel, Dynamics of continental collision: Influence of the plate contact, [Manuscript evaluated as ”minor revision”]

type of delamination never occurs. The tectonic setting does not significantly influence the nature of the model response. We conclude that initial stages of continental collision are strongly affected by whether the subduction contact is a fault or a channel. Neither the slab pull magnitude nor the tectonic setting is very important to the overall geodynamics at this stage. The plate contact type, along with the slope of the incoming passive margin and the rheology of the continent, controls whether the incoming crust 1) subducts entirely, 2) separates partially or entirely from the lithospheric mantle, or 3) blocks the trench, likely leading to slab break-off.

4.1 Introduction

Continental collision, following oceanic subduction, plays a key role in connecting plate motion and orogenic events. In general, due to its thick and light crust, continental lithosphere is positively buoyant and will resist subduction, while cold and dense subducted oceanic lithosphere generates a large downward force (slab pull). Consequently, continental crust is subducted with difficulty, if at all, whereas most oceanic crust is subducted easily at an oceanic trench. In a subduction process, the collision between a continental fragment or terrane and a continental overriding plate may result in different modes: 1) the incoming continental material arrives at the trench and is subducted, 2) all or part of the continental buoyant crust is separated from the lithospheric mantle and is accreted to the overriding plate, allowing continuation of plate convergence, 3) the approaching continental margin locks the trench, eventually resulting in slab break-off (slab detachment). All these processes appear to be possible and which of these scenarios takes place or has taken place in a certain region, depends on several factors: large scale tectonic setting of the two plates involved and more local factors such as the rheological parameters, the geometry of the continental margin and the buoyancy.

Subduction of continental crust, together with the lithospheric mantle, results in a positive buoyancy force opposing the negative buoyancy force of the dense mantle part of the lithosphere. Nevertheless, deep subduction of continental crust is possible if, for example, the crust becomes denser because of phase transformations (Austrheim, 1987; Le Pichon et al., 1992; Dewey et al., 1993). In nature, there is ample evidence that continental crust may have experienced pressure of about 30-35 kbar. The evidence comes from ultra-high pressure metamorphic minerals (e.g., coesite, diamond) revealing subduction of continental crust to mantle depth and subsequent exhumation (e.g. Chopin, 2001; Smith, 1984; Liou et al., 2000; Yang et al., 2003). Numerical studies supported the idea that the upper crust can reach a burial depth varying between 50 and 450 km if the crust is tightly welded to the subducting mantle by a strong rheology and if slab break-off does not occur (Ranalli et al., 2000;

Regard et al., 2003; Toussaint et al., 2004). Another mechanism affecting subduction of the continental crust is the inter-plate pressure between the overriding and the subducting plate. Chemenda et al. (1996) showed that a low inter-plate pressure allows the continental crust to subduct to a depth of 200 km without failure. They found that the subducting continental crust reaches a maximum depth that is proportional to the strength of the crust and inversely proportional to the inter-plate pressure.

The whole crust, or part of it, may separate from the lithospheric mantle and remain at the surface (Cloos, 1993; Kerr & Tarney, 2005; Vos et al., 2007). This implies that when crust and mantle lithosphere subduct, their speed and direction can be different. This process, known as delamination, was proposed originally by Bird (1978) to explain some of the tectonic features in the Himalayas and it is, indeed, a suitable mechanism to facilitate continuation of subduction. Delamination is only possible if there is a layer of weak material within the continental crust, e.g. the lower crust (Ranalli et al., 2000; Toussaint et al., 2004). Chemenda et al. (1996) showed that continental crust delamination occurs in front of the subduction zone when the inter-plate pressure between overriding and subducting plate is high. For several regimes progressive separation of the lithospheric mantle from the buoyant continental crust has been proposed, e.g., the Colorado Plateau (Bird, 1979), the Barbados Ridge (Westbrook et al., 1988).

Another possibility is that the incoming continental material may lock the trench, possibly resulting in break-off of the slab if the slab is not sufficiently strong (Davies & von Blanckenburg, 1995; Wong A Tong & Wortel, 1997; Wortel & Spakman, 2000; Boutelier et al., 2004; Faccenna et al., 2006). Alternatively, the continental lithosphere thickens until it drips into the deeper mantle as a result of a Rayleigh-Taylor thermal instability (Houseman et al., 1981; Houseman & Molnar, 1997; Pysklywec et al., 2000). Whether and at which depth slab break-off occurs is a function of temperature and convergence velocity (Davies & von Blanckenburg, 1995; Wong A Tong & Wortel, 1997; Sobouti & Arkani-Hamed, 2002; Toussaint et al., 2004). Strong slabs preserve their integrity against the increase of the integrated crustal buoyancy with the amount of subducted crust. The feasibility of slab detachment started to be investigated in the early seventies. Some studies suggested that the gaps in seismic activity as a function of depth might be explained by the existence of detached slabs (Isacks & Molnar, 1971; Barazangi et al., 1973). Subsequently, seismic tomography allowed for the identification of real gaps in slab structure (e.g., Spakman, 1990; Blanco & Spakman, 1993). Slab break-off has been used to explain the upper mantle structure and tectonic deformation in many regions, e.g. the Mediterranean-Carpathian region, the New Hebrides, Turkey (Chatelain et al., 1992; Wortel & Spakman, 1992, 2000; Parlak et al., 2006; Lei & Zhao, 2007). Understanding the factors controlling the three different modes of continental collision is important for unraveling the tectonic

evolution of convergent plate boundary regimes.
At convergent plate boundaries, the properties of the plate contact are important for the overall dynamics. Two fundamental physical states of the subduction contact can be distinguished: one based on a fault and the other based on a subduction channel. A subduction zone may evolve from one state to another, e.g., through a variation in sediment supply. For normal oceanic lithosphere subduction, De Franco et al. (2007a) (Chapter 3 of this thesis) have illustrated that the type of plate contact (i.e., channel or fault) changes the way in which the stresses are transmitted from one plate to the other, and affects the velocity of subduction and the magnitude of the inter-plate pressure. The fact that these are also taken to be governing factors in the evolution of continental collision (see above) motivates us to assess for the first time the role of the plate contact in this process.
In the present study we show that critical differences develop during initial stages of the collision. Through numerical modeling we illustrate how, for the same rheological properties and driving forces, a variation of plate contact type results in different modes of continental collision: subduction of the continental material, delamination or break-off. Here we focus on two tectonic settings. In the first scenario the subducting plate is pushed into the subduction zone by virtue of the plate tectonic setting (e.g., Himalayas). This is in contrast with the second setting of a land-locked basin, where there is no net convergence between the surface plates, so that subduction must occur through roll-back (e.g., the Apennine and Hellenic arc systems in the Mediterranean region).

4.2 Numerical method and model setup

In this study we do not make predictions for any real continental subduction zone, but we are interested in understanding the physical process involved. For this reason, we choose to analyze a generic subduction zone in which a passive margin arrives at the plate contact after the oceanic lithosphere has been subducted beneath a continental overriding plate. In our models the subduction zone is represented by a two dimensional cross section (Fig. 4.1). Although continental collision processes have important three-dimensional features, the first order effects of convergence can be appreciated by analyzing a characteristic cross section normal to the trench. With this simplification we assume that the continent extends infinitely in the out-of-plane direction.
Because the numerical method and the model setup used in this study are very similar to De Franco et al. (2007a), we refer to their study for more detailed aspects. The dynamics of the lithosphere and upper mantle is governed by the momentum equation. Using the plane strain approximation, we solve this partial differential equation for

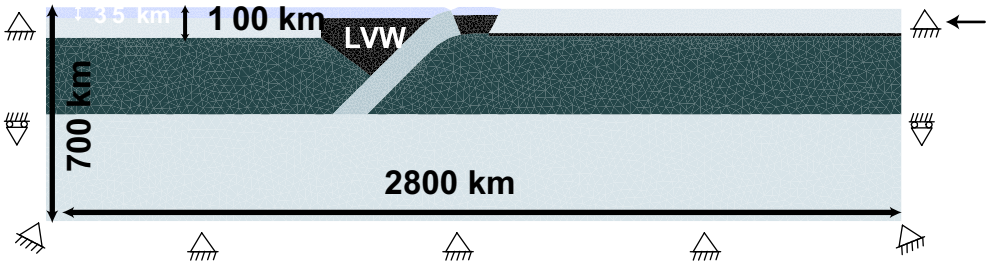

Figure 4.1: Model setup. On the left the continental plate with the continental crust on top, on the right the oceanic plate. Boundary conditions: on the bottom no displacement; on the left: the lithosphere is locked, in the mantle horizontal displacement is allowed; on the right: the lithosphere is locked or a velocity of 5 cm/yr is applied. In the mantle horizontal displacement is allowed.

instantaneous velocities and stresses. We use the G-TECTON finite element code to solve the momentum equation (http://www.geo.uu.nl/Research/Tectonophysics) (Melosh & Raefsky, 1983; Govers, 1993), and the steady state diffusion-advection equation (Govers & Wortel, 1993; De Franco et al., 2007a). Constitutive laws in the model represent elastic, viscous and plastic deformation. Viscosity is taken to be strongly temperature dependent, in accordance with rock mechanical experiments in both the power-law and diffusion creep regime (e.g., Kohlsteldt & Zimmerman, 1996). Density also depends on temperature and is expressed by a linear equation of state in our model.

We adopt two different ages for the surface oceanic lithosphere at the right hand model boundary: one of 33 My and one of 25 My. Here, the initial geotherms are defined using a half space cooling model. Using a spreading rate of the oceanic lithosphere of 4 cm/yr, the oceanic age at the trench is about 70 My and 40 My, respectively. Temperatures in the continental overriding plate are based on a representative steady state geotherm with a surface heat flow of 65 mW/m^2 (Ponko & Peacock, 1995, Table 4.1). In the sub-lithospheric mantle, we use an adiabatic gradient of 0.3 ^0K/km (Ponko & Peacock, 1995). The imposed surface temperature is 0 ^0C for both models. The initial temperature field for the first model is displayed in Figure 4.2a. Temperatures at the right and left side of the model correspond to the two geotherms plotted in Figure 4.2b. These geotherms represent the side boundary conditions used to solve the diffusion-advection equation.

Figure 4.1 displays the model domain. It is characterized by a depth of 700 km and a horizontal extension of 2800 km. The subducting oceanic plate with a continental

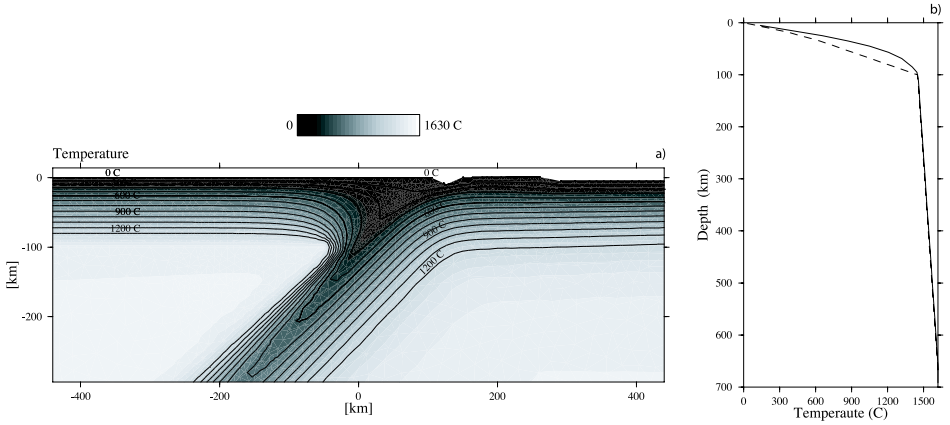

Figure 4.2: a) Total temperature distribution. b) Geotherm at the sides of the model domain. Solid curve: temperature boundary condition at the right side of the model; dashed curve: temperature boundary condition at the left side of the model.

block embedded is on the right, the overriding plate is on the left. The incoming continental margin is located at the plate contact. We adopt two inclination angles of 3^o and 15^o for the incoming margin continental slope. These values are derived from our analysis of the current global distribution of slope inclination angles of passive margins representing the most common and the maximum slope inclination angle, respectively (see Figure 4.3). The histogram is obtained from the analysis of a global 5-minute latitude/longitude topography data set (ETOPO5). The crustal thickness of the continental fragment is assumed to be 26 km. The continent is in isostatic equilibrium. The shape of the curved portion of slab is defined by an error function (Govers and Wortel, 2005); we adopt a radius of curvature R of $1.6L$ ($L = 80$ km being the thickness of the oceanic lithosphere in our models) and final dip angle θ of 45^o. The slab initially extends to 350 km depth. In some models, we also use a shorter slab that extends to 175 km depth. The overriding plate is 100 km thick, which represents the lithospheric mechanical thickness defined by the viscosity structure, and has a crustal thickness of 35 km.

The rheology of our model is elastic, viscous, or plastic and depends on composition, temperature, pressure and effective stress (Table 4.1). Model viscosities follow from either steady state dislocation creep or steady state diffusion creep. We choose model parameters following Karato & Wu (1993) for the mantle, where the parameters are chosen to be intermediate between their wet and dry values since they concluded

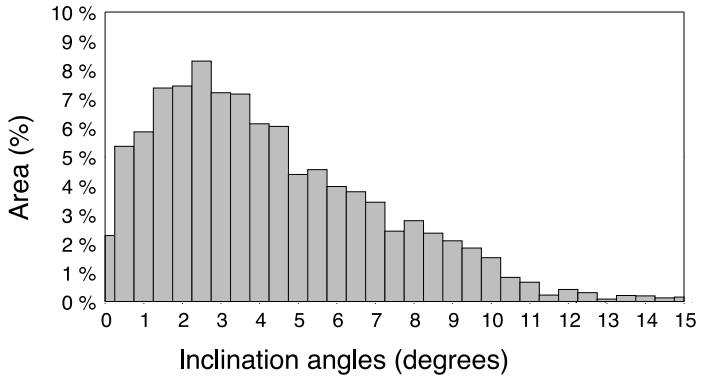

Figure 4.3: Global distribution of inclination angles of continental slopes at passive margins.

Thermal properties	k conductivity	H heat production	C_p specific heat	
continental crust	2.8 $W\ m^{-1}K^{-1}$	$6.81 \cdot 10^{-7}\ W/m$	$1.24 \cdot 10^{3}\ J\ kg^{-1}\ K^{-1}$	
lithosph. mantle	3.14 $W\ m^{-1}K^{-1}$	0	$1.17 \cdot 10^{3}\ J\ kg^{-1}K^{-1}$	
sub-lithosph. mant.	3.14 $W\ m^{-1}K^{-1}$	0	$1.17 \cdot 10^{3}\ J\ kg^{-1}K^{-1}$	
Elastic properties	*E Young's modulus*	*ν Poisson's modulus*		
continental crust	$5 \cdot 10^{10}$ Pa	0.3		
lithosph. mantle	$1 \cdot 10^{11}$ Pa	0.25		
sub-lithosph. mant.	$1 \cdot 10^{11}$ Pa	0.25		
Creep properties	*A pre-exponent*	*Q activ. energy*	*V activation volume*	*n*
continental crust	$8.3 \cdot 10^{-26}\ Pa^{-n}\ s^{-1}$	163 $kJ/mole$	$17 \cdot 10^{-6}\ m^3/mole$	3.1
mantle $<$ 350 km	$9.18 \cdot 10^{-16}\ Pa^{-n}\ s^{-1}$	485 $kJ/mole$	$25 \cdot 10^{-6}\ m^3/mole$	3.25
mantle $>$ 350 km	$1.54 \cdot 10^{-11}\ Pa^{-n}\ s^{-1}$	270 $kJ/mole$	$6 \cdot 10^{-6} m^3/mole$	1

Table 4.1: Thermal (Ponko, 1995), elastic (Dziewonski,1981) and creep model parameters. n is the stress power exponent

that the rheology of the upper mantle is between that of dry (water-free) and wet (water-saturated) olivine. For continental crust of both the overriding plate and the fragment we use rheological parameters from Freed & Burgmann (2004) (see Table 4.1). Dislocation creep is assumed to prevail at a depth shallower than 350 km, whereas diffusion creep dominates within the transition zone (Karato & Wu, 1993).

In the region of the mantle lithosphere and asthenosphere above the subducting slab (Figure 4.1), the low viscosity mantle wedge (LVW) reduces the dynamic downwarping of the overriding plate in the arc/back-arc region (Billen & Gurnis, 2001).

In our model, we assume a uniform viscosity of $5 \cdot 10^{19}$ Pa·s in the mantle wedge. Following Billen & Gurnis (2001), this value has been chosen 10 times smaller than the minimum asthenosphere viscosity. We apply an isotropic Von Mises criterion to limit deviatoric stresses in accordance with Byerlee's law (Byerlee, 1978) with hydrostatic fluid pressure and horizontal compression.

We use two descriptions for the active plate contact: a subduction fault and a subduction channel, with the following characteristics:

1) A subduction channel separates the subducting and the overriding plate. The channel width is assumed to be approximately 6 km, similar to what have been used in previous model studies (Shreve & Cloos, 1986; Beaumont et al., 1999) and in agreement with seismic studies that have shown the presence of inter-plate sedimentary channel-like units of about 1-8 km (Eberhart-Phillips & Martin, 1999; Oncken et al., 2003; Abers, 2005; Tsuru et al., 2002). Channel viscosity is taken to be Newtonian, with a value of $7{\cdot}10^{18}$ Pa·s (Shreve & Cloos, 1986; England & Holland, 1979). We name this class of models CM (channel models).

2) A deformable subduction fault is described via updated slippery nodes, in which the fault slip is locally kept parallel to the fault (Buiter et al., 2001). Fault friction is negligible. We name this class of models FM (fault models).

We separate model densities into a 1D reference density profile and the remaining density anomalies (Govers & Wortel, 2005). Reference densities are used to initialize hydrostatic pressures which initially do not contribute to the forcing. The remaining density anomalies (i.e., slab pull forces) are used to drive model deformation and are instantaneously applied at the beginning of the model calculation. Bending stresses would be expected to exist in the initially curved portion of the slab. We do not include these initial bending stresses. However, bending stresses do develop as the slab deforms during the model evolution. The continental fragment is positively buoyant and its density anomaly varies between 100-400 kg m^{-3} (Ranalli et al., 2000).

During the numerical experiments, we perform a remeshing procedure of the deformed grid. The reason is that in our Lagrangian approach the finite element mesh becomes so distorted that integrals and derivatives needed in the finite element problem cannot be properly approximated. Our remeshing method consists of updating the connectivity between Lagrangian node positions. Taking particular care to preserve material boundaries and physical boundaries, we adopt a Delauney triangulation using "Triangle" (Shewchuk, 2002) to define new elements. Subsequent to mapping element quantities from the old to the new grid, we compute (artificial) forces resulting from the inaccuracies of the procedure and update stresses to re-enforce mechanical balance. This procedure results in very limited artificial diffusion of momentum (see Chapter 2).

First, we concentrate on models in an "open" tectonic setting in which we impose ve-

locity boundary conditions of 5 cm/yr on the lithospheric right-hand side of the model and we fix the lithosphere at the left-hand side of the overriding plate. The Himalayan plate boundary is a classical example for this type of setting. Second, we study models for a land-locked basin setting, an example of which is the Mediterranean basin (Le Pichon, 1982); a zero or very small relative motion between continents that surround an oceanic basin has as a consequence that basin-internal subduction needs to be accompanied by back-arc extension. Thus, our lithospheric boundary conditions do not allow relative motion between the far field plates. We ignore convective motions beneath the lithosphere that are not driven by the sinking slab or plate motions, since our focus is on the subduction zone. This has one immediate consequence for the boundary conditions acting on the sub-lithospheric part of the side boundaries: these boundaries are far enough from the central down-welling region to result in horizontal in and out-flow only beneath the lithosphere. We assume a significantly higher viscosity in the lower mantle beneath the lower domain boundary (Mitrovica & Forte, 1997); in our model this is represented by no slip boundary conditions at the bottom of the model.

4.3 Results

In the experiments described below we applied two types of boundary conditions. First, the open subduction setting where we impose a velocity of 5 cm/yr at the right-hand side of the subducting plate and we fix the left-hand side of the overriding plate. Second, we use a land-locked basin setting in which there is no net convergence between the surface plates. We also investigate two different types of geometries for the incoming continental sliver; one with a continental slope inclination angle of 3^0 and a steeper one with a continental slope inclination angle of 15^0.
The results are displayed from Figure 4.4 to Figure 4.7. Figures 4.4 and 4.6 show the surface expressions of the models in the open subduction setting and land-locked basin setting, respectively. Figures 4.4a and 4.6a display the horizontal velocity of the free surface for the entire model domain at 0.56 My. At this time model initialization signatures have decayed. The trench is visible as a step change at horizontal coordinate 100 km. Figures 4.4b and 4.6b show the evolution with time of the ratio obtained dividing the slab velocity magnitude by the velocity magnitude of the horizontal part of the oceanic plate after the initial spin-up period of the model. The ratio is one if the plate has a plate-like behavior. A value greater than one indicates that the slab moves faster than the horizontal part of the plate, suggesting that plate thinning occurs somewhere in between the two points where the velocities are taken (red and blue circles in Fig. 4c). When the ratio is less than one, the slab moves slower than the surface plate, resulting in plate thickening.

Figures 4.5a1-a5 display the total strain rate distribution for the open subduction model at 0.56 My, while Figures 4.5b1-b5 show the evolution of the strain rate with time in two areas: the solid black line corresponds to the area in the black circle in Figures 4.5a1-a5, the red curve corresponds to the strain rate in the crust of the incoming continental margin (red circle in Figure 4.5a1-a5). The curves represent the average strain rate value of the two regions. Figure 4.7a-b shows the horizontal stress at the surface of the model domain for the open and land-locked basin setting.

4.3.1 Channel models (CM)

In this setup the plate contact is described by a low viscosity channel that extends to a depth of 100 km. The viscosity of the channel is $\eta = 2 \cdot 10^{18}$Pa·s.

Channel model with open subduction boundary conditions and 3^0 continental slope inclination angle ($\mathbf{CMO_3}$)

The horizontal velocity of the subducting plate varies from 5 cm/yr at the right-hand side to 5.6 cm/yr in correspondence of the continental fragment (Fig. 4.4a black solid curve). This is due to the response of the plate to buoyancy and slab pull. Close to the plate contact, the overriding plate is characterized by a negative velocity, indicating the overriding plate retreats from the trench with a speed of about 5 mm/yr. In Figure 4.4b, the velocity ratio is represented by the black solid curve and is equal to a constant value close to one, denoting that the velocity along the subducting plate is uniform and it remains uniform as a function of time.
The strain rate distribution is displayed in Figure 4.5a1 at 0.56 My. The strain rate in the slab and in the continental crust of the incoming fragment has a small magnitude of about $1{\cdot}10^{-15}\ s^{-1}$. In the entire model domain, the highest value of the strain rate is in the subduction channel and below the horizontal subducting plate. These two regions represent relative thin layers of rapidly deforming material. In Figure 4.5a1, the deformed geometry of the model shows that the continent has been dragged down with the subducting plate to a depth of about 30 km. In Figure 4.5b1, the average value of the strain rate in the slab shows a nearly stationary behavior as a function of time. The strain rate is not affected by the subduction of the buoyant continental crust. On the other hand, the crustal strain rate slightly increases with time.

Channel model with open subduction boundary conditions and 15^0 continental slope inclination angle ($\mathbf{CMO_{15}}$)

In this model, the continental slope of the margin is inclined at an angle of 15^0. The steeper geometry of the continental fragment results in a similar response of the

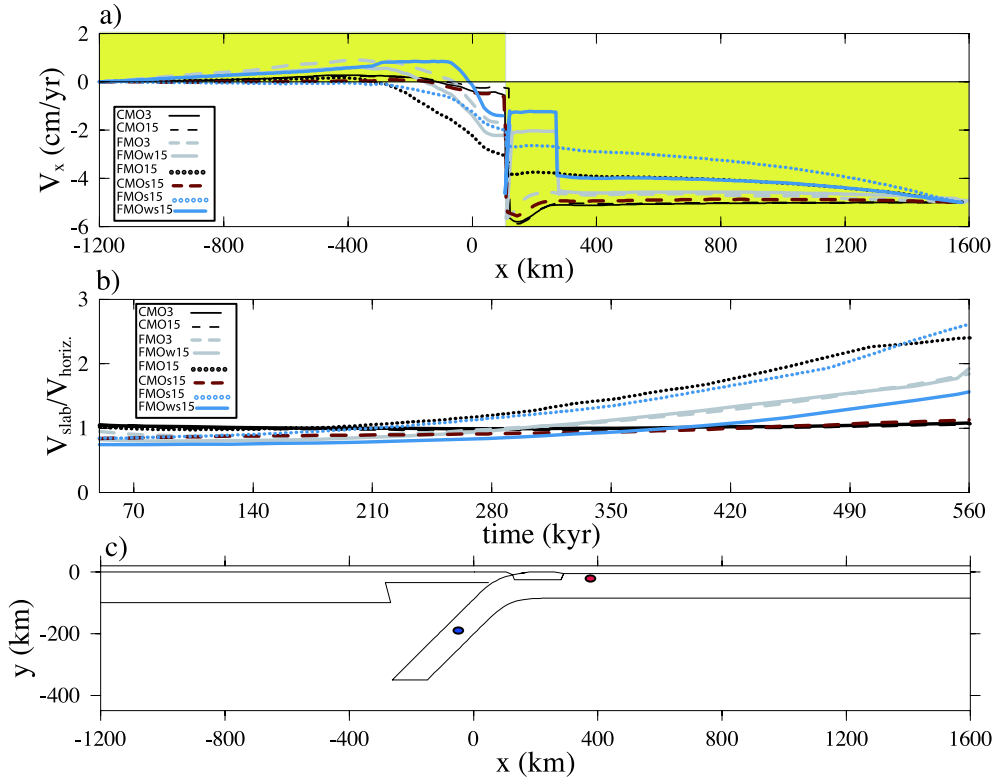

Figure 4.4: Surface expression for models with open subduction boundary conditions. a) Horizontal velocity at the surface of the model for the entire domain at 0.56 My. Velocities in the yellow areas are directed towards the trench, at horizontal coordinate of about 100 km. b) Ratio obtained by dividing the slab velocity (V_{slab}) by the velocity of the horizontal part of the oceanic plate ($V_{horiz.}$) versus time. c) The colored circles indicate the region in which the velocities used to calculate the ratio in b have been taken.

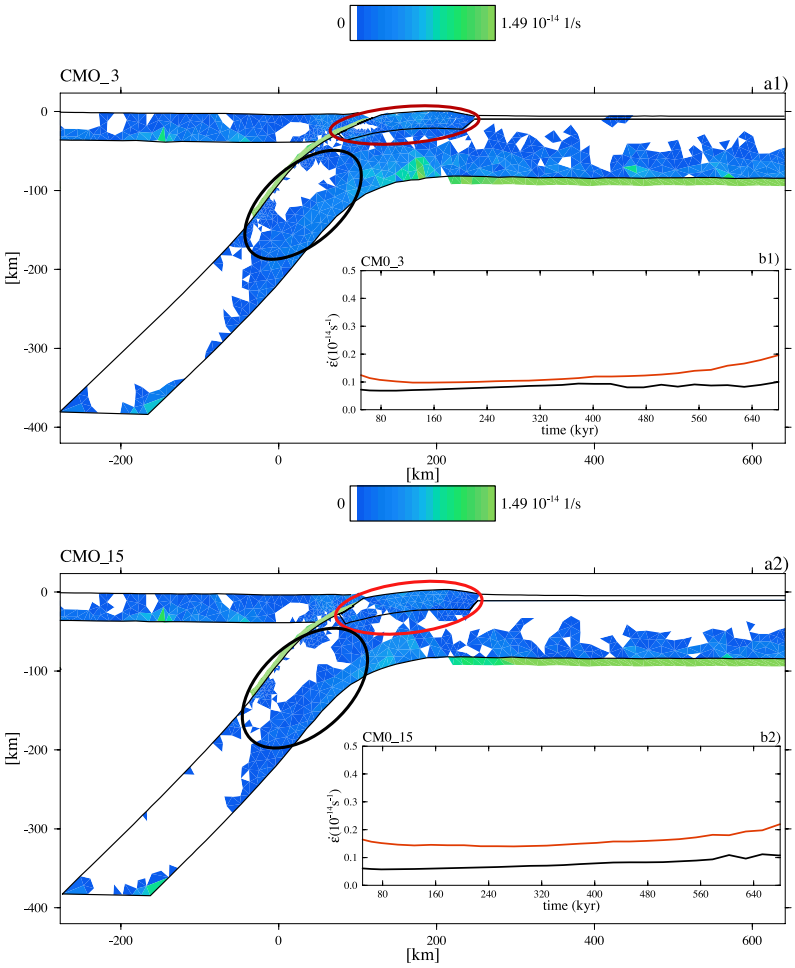

Figure 4.5: a) Effective strain rate distribution at 560 kyr and b) average effective strain rate evolution. Solid black curve corresponds to the region in the solid black circle in a, red curve corresponds to the red circle in a. a1 and b1 show the strain rate for CMO_3, a2 and b2 show the strain rate for CMO_{15}.

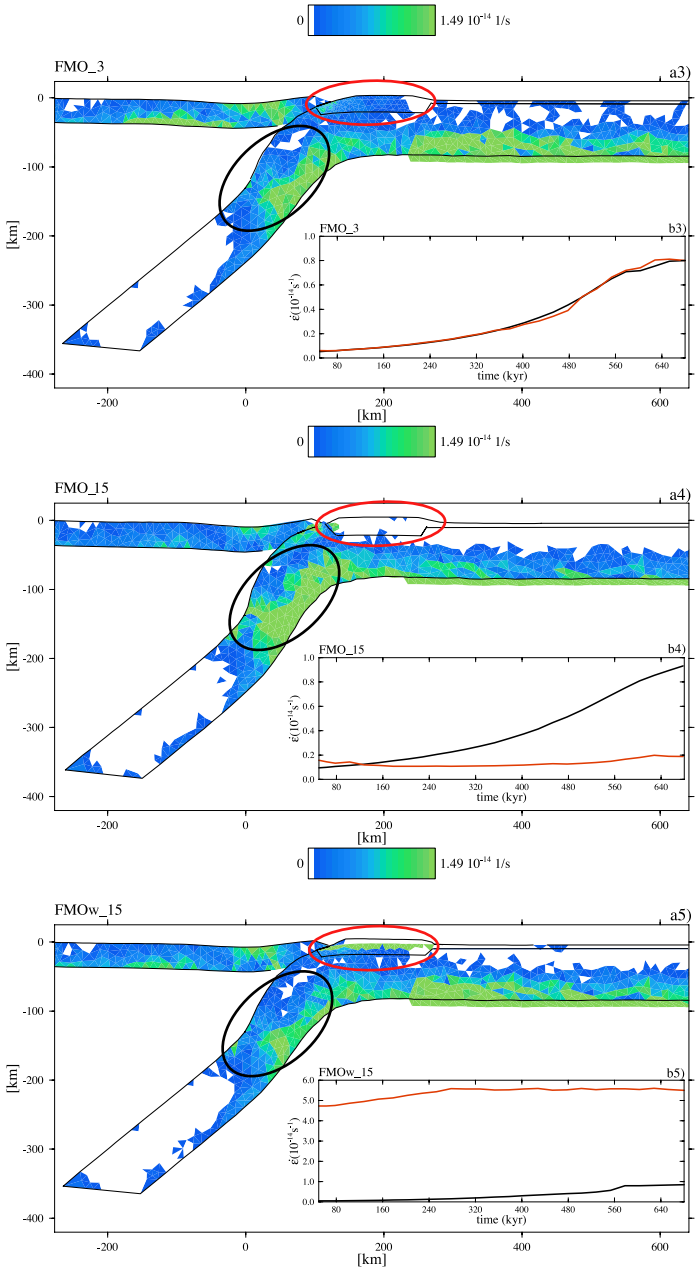

Figure 4.5: (Continued). Effective strain rate at 560 kyr (a) and average effective strain rate evolution (b). Solid black curve corresponds to the region in the black circle in a, red curve corresponds to the red circle circle in a. a3 and b3) show the strain rate for FMO_3, a4 and b4 for FMO_{15} and a5 and b5 for $FMOw_{15}$.

model as CMO_3.

The subducting plate moves with a speed of about 5 cm/yr and, close to the plate contact increases to a value of about 5.6 cm/yr (Fig. 4.4a black dashed curve). The overriding plate velocity is nearly zero, except close to the plate contact where the velocity is negative: this region of the overriding plate moves towards the left with a speed of about 4 mm/yr.

Like in the previous model, the velocity ratio is equal to one. This means that the velocity along the subducting plate is uniform and that this plate-like behavior is not perturbed in time (Fig. 4.4b black dashed curve).

Like in CMO_3, the strain rate within the subducting plate is small (Fig. 4.5a2). Strain rate is high in the channel and beneath the oceanic surface plate. The deformed geometry of the model displays that the incoming continental fragment is subducted to a depth of about 30 km. In Figure 4.5b2 the average value of the strain rate shows a nearly stationary behavior. This curve displays a response very similar to the previous model. The continental crust is characterized by a slightly higher strain rate than in the slab.

We performed an experiment in which the lower crust of the continental margin is characterized by a low strength of about 30 MPa ($CMOw_{15}$). The results are very similar to those of CMO_{15}, for this reason we decide not to show them.

Channel model with land-locked-basin boundary conditions (CML_3, CML_{15})

Here we impose land-locked basin boundary conditions. We adopt two inclination angles, 3^0 and 15^0, of the incoming continental margin.

In Figure 4.6a, the black solid line represents the velocity of CML_3 at 0.56 My. The speed of the oceanic plate increases linearly towards the trench with a maximum value of about 2 cm/yr. The overriding plate moves towards the right with a maximum speed of 1 cm/yr. The dashed black line shows the velocity of CML_{15}. Like before, the velocity increases towards the plate contact. The velocity magnitude is slightly smaller than in CML_3. The overriding plate is characterized by the same behavior as CML_3.

In Figure 4.6b the black solid curve and the black dashed curve represent the velocity ratio of CML_3 and CML_{15}, respectively. They are characterized by a constant value equal to 1.3. Different from CMO, velocities in CML are not plate-like.

The strain rate distribution for these models is very similar to that of CMO_3 and CMO_{15}. Therefore, we will subsequently show these results in the Appendix D.

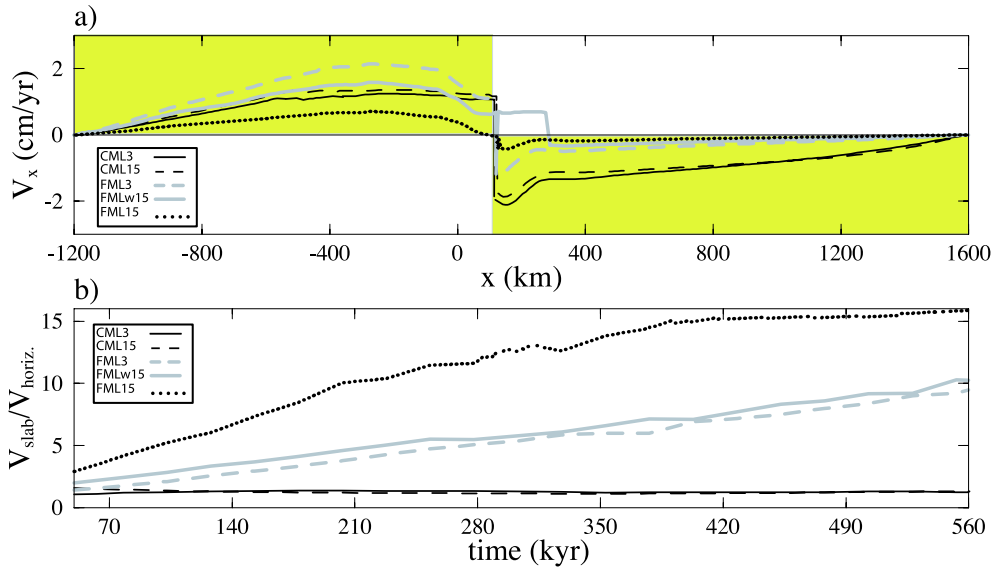

Figure 4.6: Surface expression for models with land-locked subduction boundary conditions. Velocities in the yellow areas are directed towards the trench, at horizontal coordinate of about 100 km. a) Horizontal velocity component (V_x) at the surface of the model for the entire domain at 0.56 My. b) Ratio obtained by dividing the slab velocity magnitude (V_{slab}) by the velocity magnitude of the horizontal part of the oceanic plate ($V_{horiz.}$) versus time.

4.3.2 Fault Models (FM)

In these models the plate contact is described by a frictionless fault that extends to a depth of 100 km.

Fault model with open subduction boundary conditions and 3^0 continental slope inclination angle (FMO_3)

In Figure 4.4a, the grey dashed curve shows the horizontal velocity at the surface at 0.56 My. The convergence velocity is 5 cm/yr and it decreases towards the plate contact, to increase again in correspondence of the continental fragment. The overriding plate, close to the plate contact moves away from the trench with a maximum value of 1.5 cm/yr. In this region the velocity is higher than in the CM.
The grey dashed curve in Figure 4.4b shows the velocity ratio as function of time. This velocity ratio increases with time. This indicates that the horizontal part of the oceanic plate moves slower than part of the slab and that the velocity difference between the two regions enlarges with time. Down-dip extension thus occurs somewhere within the region between the two points indicated in Figure 4.4c.
Figure 4.5a3 displays the total strain rate distribution at 0.56 My. The strain rates in the slab, in the continental crust and in the overriding plate are higher than those in the CM. The slab significantly deforms at a depth of about 150 km, where the strain rate is localized. The deformed geometry of the domain shows that the incoming continental crust is subducted to a depth of about 15 km. The depth reached by the subducting continent is shallower than in the CM. The overriding plate is characterized by high strain rate and marked down-welling. In Figure 4.5b3 the black and the red curves show that the average strain rate in the slab and in the crust of the incoming fragment increases with time, reaching higher values than the previous models. Strain rate is high beneath the oceanic surface plate.

Fault model with open subduction boundary conditions and 15^0 continental slope inclination angle (FMO_{15})

The black dotted curve in Figure 4.4a shows that the velocity jump at the trench is strongly reduced with respect to FMO_3. The horizontal velocity shows that the speed of the subducting plate decreases from the right-hand side towards the plate contact to less than 4 cm/yr. The overriding plate moves in the same direction as the subducting plate in the region between the plate contact and the horizontally projected tip of the slab end. The rate of retreat of the overriding plate from the trench is faster than in all previous models. The rest of the overriding plate has velocity magnitude equal to zero.

In Figure 4.4b black dotted line, the velocity ratio increases with time faster than in all the models so far. Such a behavior shows that the horizontal part of the oceanic plate moves slower than the slab.

The strain rate in the slab and in the overriding plate is higher than in the CM and in FMO_3 (Fig. 4.5a4). From the deformed geometry of the model it is evident that the incoming continent locks the trench and does not subduct with the oceanic material. The slab deforms more than in FMO_3 at a depth of about 150 km. The strain rate in the slab is higher than in FMO_3. Figure 4.5b4 shows the average strain rate in more detail: the strain rate in the slab increases with time more than in FMO_3 reaching a maximum value of about $1 \cdot 10^{-14} s^{-1}$. In the crust the strain rate is stationary and lower than in FMO_3. Strain rate is high beneath the oceanic surface plate.

Fault model with open subduction boundary conditions, 15^0 continental slope inclination angle, and weak crustal layer ($FMOw_{15}$)

In this model, the strength of the weak crustal layer of the incoming continental fragment is 30 MPa, about 50 $\%$ lower than FMO_{15}. The subducting plate moves at a speed of 5 cm/yr, and jumps to 2 cm/yr in the continental fragment (Fig. 4.4a solid grey curve). The part of the overriding plate that is closest to the plate contact moves towards the left-hand side, while the rest of the overriding plate advances towards the plate contact. The continental fragment moves with the same velocity and in the same direction as the near-trench part of the overriding plate. The velocity jump along the subducting plate is an expression of shear delamination of the upper crust from the rest of the lithosphere.

The velocity ratio (grey solid curve in Figure 4.4b) increases with time similar to FMO_3. However, it increases less than in FMO_{15} indicating that crustal delamination decreases down-dip extension.

The strain rate distribution in the slab and in the overriding plate is very similar to the one of FMO_3 (Fig. 4.5a5). The strain rate maximizes in the slab at a depth of about 150 km; at that depth the slab is strongly deformed. A high strain rate region is visible in the crust of the continental margin. This is the expression of the shear delamination process, in which the upper crust separates from the lower one. The lower crust continues to subduct reaching a depth of about 15 km during the modeled period. The detailed representation of the strain rate in Figure 4.5b5, indicates that the average strain rate in the slab increases with time but less than in FMO_{15}. In the crust, the strain rate is one order of magnitude higher than in the slab and higher than in all the other models.

Fault models with land-locked-basin boundary conditions (FML_3, FML_{15}, $FMLw_{15}$)

The following experiments are characterized by land-locked basin boundary conditions. We adopt two inclination angles of the incoming continental margin of 3^0 and 15^0, FML_3 and FML_{15} respectively. In $FMLw_{15}$ (w=weak), we use the same geometry as in FML_{15} but the strength at the transition between lower and upper crust of the incoming passive margin is lower and its value is about 30 MPa.
In FML_3, the surface velocity of the subducting plate is lower than in either of the channel models (CML_3 and CML_{15}); it increases towards the trench with a maximum value of 1 cm/yr (Fig. 4.6a grey dashed curve). In the overriding plate the velocity increases towards the trench with a maximum speed of 2 cm/yr. The black dotted curve shows the surface horizontal velocity of FML_{15}. The subduction rate is a few mm/yr and it is smaller than in FML_3. The overriding plate moves at a maximum speed of about 0.5 cm/yr which is slower than in all the previous models. The subduction velocity of $FMLw_{15}$ is a bit lower than the velocity of FML_3 but higher than in FML_{15} (Fig. 4.4a solid grey curve). The main difference between FML_{15} and $FMLw_{15}$ is that the upper crust of FML_{15} hardly moves, and that $FMLw_{15}$ shows substantial movement towards the right. There is no relative motion across the trench in FMLw15, and the upper crust of the continental fragment moves along with the crust of the overriding plate at a speed of 1 cm/yr.
In Figure 4.6b the grey dashed curve shows the velocity ratio of FML_3. The ratio increases with time. This means that the horizontal part of the oceanic plate moves more slowly than the slab. Such a difference increases with time. The black dotted line, represents the velocity ratio of FML_{15}, while the grey solid curve is the ratio of $FMLw_{15}$. The FML_{15} velocity ratio increases faster than in all other subduction models. The $FLMw_{15}$ velocity ratio is only slightly higher than in FML_3 ratio. In both cases, the horizontal part of the oceanic plate moves slower than the slab, indicating down-dip extension of the subducting plate. The detailed description of the strain rate distribution for these models is displayed in Appendix A. We performed some tests with stronger rheology of the plates; since the main characteristics of our results do not change, we decided not to show these results.

4.3.3 Short slab models ($CMOs_{15}$, $FMOs_{15}$, $FMOws_{15}$)

In the next models we want to estimate the importance of the slab pull in the evolution of our experiments. In order to reduce the slab pull, we diminish the length of the slab, that in the following experiments reaches an initial depth of 175 km. In these experiments we only use the continental margin with slope inclination angle of 15^0. We impose a velocity of 5 cm/yr at the right lithospheric boundary of the models and we fix the left side of the overriding plate.

The results are summarized in Figure 4.4. In Figure 4.4a the red dashed curve represents the horizontal velocity for $CMOs_{15}$ at 0.56 My. The only difference with respect to CMO_{15} is that the velocity magnitude is slightly reduced. The velocity ratio of $CMOs_{15}$ also is similar to CMO_{15} (Fig. 4.4b). The velocity of the slab is initially slower than in the horizontal part of the plate (curve value lower than one). With time it increases until the ratio reaches a constant value equal to one. This suggests that the continental margin is pushed coherently into the subduction zone with the oceanic lithosphere in a steady plate-like fashion.
For the same type of geometry, we further reduce the density anomaly of the slab (we do not show these curves in Figure 4.4), and even in this case the behavior of the model does not change much. In the extreme case, in which the slab pull due to the negatively buoyant oceanic lithosphere is zero, the subducting plate continues to be driven into the mantle and slowly tends to reach the same tectonic state of the previous CM.
In the FM, reducing the slab length has a stronger impact than in the CM. The blue dotted curve in Figure 4.4 shows results of $FMOs_{15}$; the horizontal velocity of the plate is lower than in FMO_{15}. The horizontal velocity of $FMOws_{15}$ (Fig. 4.4 blue curve) is higher than in $FMOs_{15}$, but slower than in $FMOw_{15}$. Reducing the slab pull even further does not lead to a further decrease of the surface velocity. The velocity ratio does however change in this case; a slab pull results in a smaller slab velocity, making it more similar to the velocity of the surface oceanic plate.

4.3.4 Horizontal surface stress

In this section we summarize the horizontal stress response at the surface of the previous models (Fig.4.7a and Fig. 4.7b) after 0.56 My. Away from the plate boundary zone, there is an overall tendency for the fault models to be more compressive than the channel models. In CMO_3 and CMO_{15} the subducting plate and the terrane are in tension, while in FMO_3 and $FMOw_{15}$ subducting plate the stress state is more variable; between $x = 1600$ km and $x = 350$ km the surface stress increases from more compressive to somewhat tensile. The stresses are compressive in the ocean plate near the terrane, and tensile in the continental fragment itself. In FMO_{15}, where the delamination of the upper crust does not develop, the stresses in the overriding plate are strongly compressive. In Figure 4.7 the overriding plate is divided in three regions. Region C extends from the left edge of the plate to the vertically projected left side of the LVW, region B extends from the vertically projected left side of the LVW to the vertically projected intersection of the slab with the Moho of the overriding plate; region A extends from there to the plate contact. Most of the channel models are largely in tension in region C in the open subduction setting. Also, tensile stresses dominate in region C of FMO3 and FMOw15. In the same region, the stress

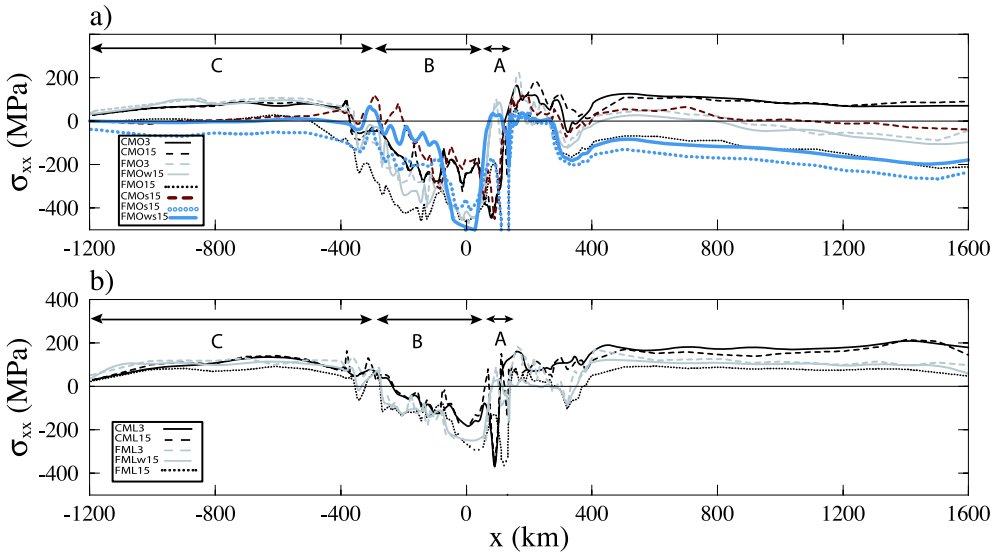

Figure 4.7: Horizontal stress (σ_{xx}) at 0.56 Myr. Compression is negative. The overriding plate is divided in three regions: region C extends from the left edge of the plate to the vertically projected left side of the LVW, region B extends from the vertically projected left side of the LVW to the vertically projected intersection of the slab with the Moho of the overriding plate; region A extends from there to the plate contact. a) Open subduction setting. b) Land-locked basin subduction

of FMO_{15} is nearly zero, indicating a more compressive tectonic system. Region C in the land-locked basin setting is mostly in tension, irrespective of the plate contact type. In region B, compressional regime prevails for all the models. Fault models in the open subduction setting tend to show more compression than channel models. In region A, horizontal stresses show a positive excursion towards more tensile stresses in the fault models. Channel models in region A do not show such behavior.
When we reduce the slab pull using the short slab model, the subducting plate experiences less tension than in the long slab models ($CMOs_{15}$ and CMO_{15} in Figure 4.7a). Horizontal stresses in region C show to be rather insensitive to the slab pull for these models. The stress change in region B of Figure 4.7a is largely brought by the fact that the slab is shorter in $CMOs_{15}$, with the consequence that the upward projection of the slab tip occurs closer to the plate contact. A reduction of the slab pull in the fault models results in a more compressive oceanic subducting plate and region C ($FMOws_{15}$). Stresses at the continental terrane becomes neutral. A simultaneous decrease of slab pull and terrane crustal strength ($FMOws_{15}$) results in a similar stress in the surface oceanic plate as in the FMO_{15}. Within region C, these models show approximately the same surface stresses too. Differences between FMO_{15} and $FMOws_{15}$ are substantial only within region B.
In the land-locked basin setting, the horizontal stress along the surface oceanic plate becomes more tensile than in the open subduction setting, for both channel and fault models. The same holds for region C of the overriding plate. The most relevant difference with respect to the open subduction is in region B, where the compressive regime is drastically reduced. Nevertheless, FM and in particular FML_{15} are characterized by the most compressive stress in that area. Table 4.2 summarizes all the models used in the experiments.

4.4 Model analysis

Our experiments are divided in two main categories: channel models (CM) and fault models (FM). In both groups we vary some of the characteristic parameters: the geometry of the incoming continental sliver, the tectonic setting, the rheology and the length of the sinking oceanic lithosphere.
In a previous study we established that the nature of plate contact affects the response of the subduction process (De Franco et al., 2007a). We found that CM are characterized by faster subduction velocities, less compression in the overriding plate, less dynamic subsidence of the upper plate, more plate-like behavior and lower inter-plate pressure than FM. We refer to this paper for a detailed explanation of the physical process that causes the differences between subduction channel and fault. These results are also valid in the present study.

Model name	Plate contact type	Boundary conditions	Continental slope angle
CMO_3	channel model	open subduction	3^0
CMO_{15}	channel model	open subduction	15^0
CML_3	channel model	land-locked basin	3^0
CML_{15}	channel model	land-locked basin	15^0
FMO_3	fault model	open subduction	3^0
FMO_{15}	fault model	open subduction	15^0
$FMOw_{15}$	fault model	open subduction	15^0, weak crust
FML_3	fault model	land-locked basin	3^0
FML_{15}	fault model	land-locked basin	15^0
$FMLw_{15}$	fault model	land-locked basin	15^0, weak crust
$CMOs_{15}$	channel model	open subduction, short slab	15^0
$FMOs_{15}$	fault model	open subduction, short slab	15^0
$FMOsw_{15}$	fault model	open subduction, short slab	15^0, weak crust

Table 4.2: Summary of the models used in this study

In the CM of the present study, the very nature of the subduction channel, with its weak material, reduces the coupling between the plates and inter-plate pressure, promoting in this way continental subduction, as already shown by Chemenda et al. (1996). As a consequence, the incoming continental fragment is subducted coherently with the oceanic lithosphere without perturbing the subduction process, at least during the initial stage of the collision. This is expressed by the fact that in the CMO the subducting plate shows a steady state plate-like behavior (solid and dashed black curves in Fig. 4.4). In CML, as a consequence of the boundary conditions, the slab moves faster than the horizontal part of the plate, but in such a way that the two velocities are constantly proportional to each others. This results in the fact that in both settings, the continental sliver is coherently subducted without localization of high strain rate in the slab (Fig. 4.5a1, a2, 4.10a1, a2).

On the other hand, FM result in a very different response. First of all, FM do not show plate-like behavior for any kind of boundary conditions and the horizontal part of the subducting plate moves always slower than part of the sinking slab (solid and dashed grey curves and black dotted curve in Fig 4.4b), moreover these differences increase with time. Such a response implies that the plate deforms with time. In all FM, the strain rate strongly differs from the cases of the corresponding CM-series. The magnitude of the strain rate is higher than in CM and localizes between -100 and -200 km depth. The slab visibly deforms (e.g., Fig. 4.5a3,b3, 4.5a4,b4, 4.5a5,b5). These features are explained by two factors. First, the high inter-plate pressure and high normal coupling between lower and upper plate in the FM hampers the subduction of the continent, while the gravitational force in the slab pulls the plate down, causing

deformation of the slab. Second, the strong flow generated in the wedge below the overriding plate (see De Franco et al. (2007a)) contributes to deformation of the slab and promotes localization of strain rate. FMO_{15} shows the highest strain rate and the most pronounced deformation of the slab. This occurs because the continental fragment, with the steep geometry and the high-strength crust, completely locks the trench, preventing subduction of the incoming continent. Since in FMO_{15} the strain rate in the slab increases with time (Fig. 4.5b4 black curve), while the strain rate in the crust is nearly constant (Fig. 4.5b4 red curve), slab break-off will possibly take place.

A general result, true for all the tectonic settings, is that the geometry of the passive continental margin of the terrane does not strongly affect the response of CM. On the other hand, the slope inclination angle of the incoming passive margin plays a very important part in FM. While in FMO_3 and FML_3 the continent starts to subduct (Fig. 4.4a, 4.6a dashed grey curve), in FMO_{15} and FML_{15} the subduction stops (see Fig.4.4a and 4.6a black dotted). The surface oceanic plate surface decreases with time. When the crustal rheology of the continental fragment permits shear delamination (i.e. $FMOw_{15}$ and $FMLw_{15}$), the response of the models becomes similar to the one of FMO_3 or FML_3.

The progressive separation of the upper crust from the lower crust occurs only in the FM when the crustal strength at the contact between lower and upper crust is low with a value of about 30 MPa (e.g. Fig.4.4a, 4.6a solid grey curve and Fig. 4.5a5, 4.10a5). The upper crust moves with a different velocity and sometimes different direction than the lithospheric mantle. Through shear deformation, the upper crust remains at the surface, while the lithospheric mantle continues to subduct. The strong overriding plate and the high inter-plate pressure hamper the subduction of the upper crust, whereas the weak strength of the lower crust allows the separation of the two units. When delamination occurs, the horizontal state of stress of the overriding plate changes: the far field plate becomes tensile (Fig 4.7a region C) as well as the region immediately close to the plate contact (Fig 4.7a region A), while in FMO_{15} the state of stress in the overriding plate is neutral or compressive. In the subducting plate compressive stresses decrease as soon as delamination takes place and subduction again starts to accommodate the convergence. In the land-locked basin setting, the state of stress of FML_{15} and $FMLw_{15}$ is not much different since the total convergence is limited by the boundary conditions. In CM, delamination of the crust does not take place, for any geometry and strength of the incoming continental material. This is due to the fact that the channel flow facilitates subduction of the continental sliver and does not act as a chisel on the incoming continental material. Moreover, the lower inter-plate pressure helps making subduction of the continental margin possible.

To understand the role of the slab pull during the initial stage of continental collision, we reduce the net pull force through the reduction of the slab length, and we keep the velocity on the right side of the subducting plate equal to 5 cm/yr. In the CM, slab pull does not significantly affect the response of the model. In CMs, after a spin up period, the subduction velocity reaches the same value as in the model with a long slab (Fig.4.4a red dashed curve). The velocity along the subducting plate becomes uniform with time (Fig.4.4b red dashed curve), meaning that the incoming continental sliver is subducted with the oceanic lithosphere without perturbing the process. However, the horizontal stress at the surface domain becomes more compressive in the subducting plate and in region C of the overriding plate, while in region B it is less compressive (see Fig. 4.7a). The higher compressive stress in region C of the upper plate and in the subducting plate is caused by the reduction of the slab pull that increases the inter plate pressure. The lower compressive stress in region B is due to the fact the tip of the slab does not anymore lie below that region, causing down-welling and compression in that part of the overriding plate. The slab velocity is fast like in the long slab experiments, because the horizontal velocity applied on the right side of the subducting plate is the same as in the long slab experiments and is strongly transmitted along the plate. The low viscosity channel reduces the transmission of such a velocity to the overriding plate. Moreover, the short length of the slab reduces the frictional forces in the mantle that opposes to the sinking of the slab.

In FM with short slabs (FMs), the subduction velocity becomes slower than in the other FM, and the overriding and subducting plate are in a more compressive regime. This is due to the fact that the horizontal velocity applied at the right side of the subducting plate is strongly transmitted through the fault to the overriding plate and that the inter-plate pressure increases (inter-plate pressure is inversely proportional to the slab pull). In FMOs_{15}, where the delamination of the crust of the continental margin does not develop, the subduction velocity is reduced even more than in the FMO_{15}. As a consequence, even though the net slab pull is less the slab moves faster than the horizontal part of the plate (Fig. 4.4b blue dotted curve). The same holds for the case in which delamination develops (FMOsw_{15}). We can conclude that a reduction of the slab pull does not affect the general response of the models.

In our models we considered different tectonic settings, in which the right-hand side of the subducting plate is pushed towards the trench and the left-hand side of the overriding plate is fixed or in which there is no net convergence between subducting and overriding plate. In this way, we consider some important possible settings present in nature. From our results we conclude that even though the tectonic setting can change some of the features of the models, the imprint due to the different plate contacts remains the same.

The results of our models are plotted as data points in Figure 4.8. The black curves

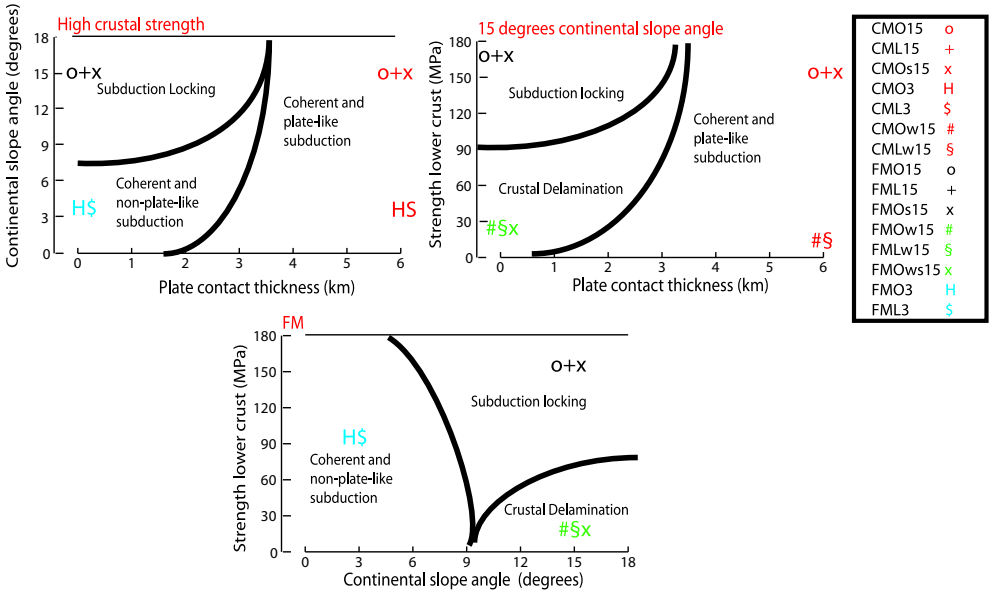

Figure 4.8: Qualitative-quantitative description of the influence of different parameters on the modes of continental collision. CM are represented by red symbols. FM with 15 degrees slope inclination angle are represented by black symbols. FM with 15 degrees slope inclination angle and a weak lower crust are represented by green symbols. FM with 3 degrees slope inclination angle are represented by blue symbols.

that divide the panels in the different mode domains are qualitatively drawn. In summary, on the basis of our numerical experiments, we support the initial idea that three modes of continental collision can develop:

1) Coherent subduction of the continental sliver. This mode is subdivided in plate-like continental subduction and non-plate-like continental subduction.

2) Crustal delamination of the upper crust of the incoming continental margin. Subsequent continuation of subduction in a non-plate-like fashion.

3) Locking of the subduction zone and possibly leading to slab break-off.

The three modes are illustrated in Figure 4.9. In the upper panel, CM_3/CM_{15} are characterized by plate-like subduction of the incoming continental margin for any type of geometry and strength of the continental fragment; in FM_3 the continental material is coherently subducted but the velocity along the slab is not plate-like and the slab deforms; in FM_{15} the passive margin locks the trench and does not subduct,

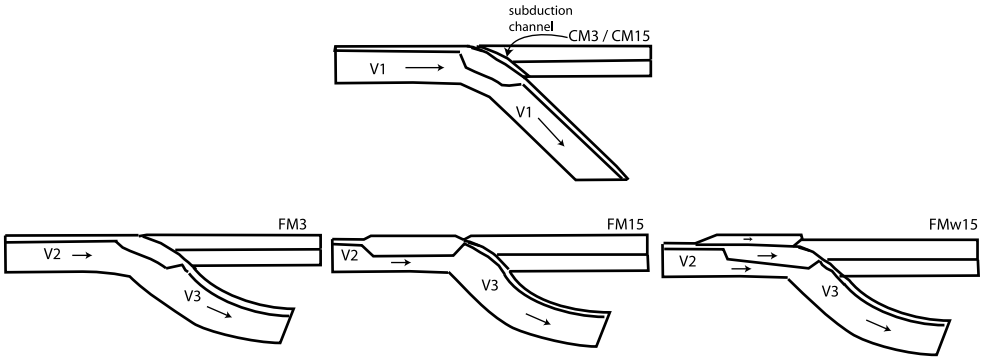

Figure 4.9: Illustration of the modes of continental collision: CM always allows coherent subduction. FM3 is characterized by coherent and non-plate-like subduction, FM15 is characterized by subduction locking, FMw15 results in shear delamination. Arrows indicate velocity.

causing even more pronounced deformation of the slab; in FMw_{15} the upper crust is separated from the lower crust in a shear mode and it remains at the surface, while the lithospheric mantle descends in the asthenosphere in a non-plate-like fashion.
We conclude that the plate contact type is critical in controlling the different modes of continental collision during the initial stage of the process. The plate contact plays a more relevant role than the magnitude of slab pull and than the tectonic setting.

4.5 A link between short and long time scale continental collision models

In previous studies, buoyancy (Ranalli et al., 2000; Sobouti & Arkani-Hamed, 2002), rheological properties of the continental and oceanic material (strength, temperature) (Wong A Tong & Wortel, 1997; van de Zedde & Wortel, 2001; Sobouti & Arkani-Hamed, 2002; Li & Liao, 2002; Toussaint et al., 2004), subduction velocity (Davies & von Blanckenburg, 1995; Li & Liao, 2002; Toussaint et al., 2004) and inter-plate pressure (Chemenda et al., 1996) have been indicated as the main variables controlling the evolution of continental collision. In our study we took a step in direction of establishing which are the parameters that dominate the behavior of continental collision during the initial stage of the process and we do not study the entire evolution of it. There are two main differences between our study and the previous ones: 1) the earlier studies did not take in consideration the nature of the plate contact, 2) we do not analyze long time scale processes.
It is likely that some of the parameters that do not play an important role in our

experiments, become relevant during a second stage of the process developing. In the following sections we make some connections between our findings and the results of other studies.

4.5.1 Deep burial of continental material and slab break-off

In our CMO, continental lithosphere starts to subduct in a coherent and plate-like fashion, indicating the possibility of deep ($>$ 30 km) subduction of the passive margin. Many numerical studies and geological data suggest that the entire continental lithosphere may be taken to even greater depths.
Ranalli et al. (2000) concluded that subduction stops when the total slab buoyancy, calculated from the summation of positive and negative density anomalies, is zero. The maximum depth reached by the continental material is a function of dip angle, geometry of sliver and convergence velocity. If the imposed velocity at the edge of the subducting plate continues to drive the plate, continental subduction can also carry on when the system is neutrally or slightly positively buoyant, as shown in our short slab experiments. This is in agreement with Regard et al. (2003), who suggested that subduction will terminate when the subducting system reaches a significant positive buoyancy. This finding indicates that a small piece of continental crust can be taken to considerable depth and that buoyancy is not very important until it reaches a certain threshold value. As a consequence, the amount of positive buoyancy of the continental crust is not a dominant parameter during the initial stage of collision. In our model, the width of the incoming continent is not crucial, whereas on a long time scale the volume of the subducted continental fragment controls the total amount of buoyancy. The depth to which continental crust can be subducted coherently decreases as the crustal thickness of the subducting continental plate increases (van den Beukel, 1992).
Nevertheless, it is plausible that a relevant change in buoyancy due to the subducting crust may cause slab break-off. Eventually slab break-off is likely to occur in collision zones in which a passive continental margin is involved, since the increasing tensional stresses generated by continued continental subduction makes extensional deformation inevitable and slab break-off probable. To estimate where and when the break-off takes place Davies & von Blanckenburg (1995) compared the integrated strength of the slab with the variation in buoyancy that results in extensional force. When this force overcomes the integrated strength, slab break-off takes place. The extensional force is proportional to the subduction depth of the continental crust and is controlled by its composition. They found that the integrated strength is strongly affected by the convergence velocity. A slow subduction is likely to promote break-off and at shallower depth than for fast subduction; for a velocity of 1 cm/yr break-off might occur between 50 and 120 km depth. This last result is common to most of the continental

collision models (e.g., Toussaint et al., 2004; Wong A Tong & Wortel, 1997; Sobouti & Arkani-Hamed, 2002). In summary, we have learned from the previous numerical studies that the parameters governing slab break-off are: strength/temperature of the slab, convergence velocity and buoyancy variation. In the light of our experiments another parameter must be added to this list: the nature of the plate contact.

4.5.2 Delamination

Another way in which subduction of the continental crust may evolve is through delamination of the entire crust or part of it. In our models we excite delamination of the upper crust in that part of the model parameter space where the inclination angle of the continental slope is unusually steep, the strength of the lower crust is low and the plate contact is described by a fault. Delamination occurs through the removal of the upper crust in a shear mode; the upper crust remains at the surface and subsequently is accreted to the upper plate. In nature this process may take place in essentially two ways: 1) by terrane or block accretion; 2) by thrusting of the delaminated upper crust over the adjacent margin of the upper plate. The latter may be accompanied by intense deformation of the over-thrust units (Willet et al., 1993). We note, however, that there are other ways in which delamination can take place. Bird (1978) proposed that the previously subducted oceanic lithosphere with its excess density could result in a large tension in the upper slab if it were prevented from sinking at its terminal velocity (Forsyth & Uyeda, 1975). This force would tend to vertically separate the sub-crustal lithosphere from the already subducted crust. This kind of delamination may generate a so-called nappe stack that consists of a series of slices of continental crust left at the plate contact by the incoming subducting plate. The last process would require subduction of the continental crust to a certain depth like, for example, in our coherent subduction models (CM and FM_3). Since from observations and model studies we know that the upper crust may reach a considerable depth ($>>$ 50 km) before being exhumed, we envisage that in models like CM and FMO_3 delamination may occur at a later stage than what we show in our models. Chemenda et al. (1996) and Toussaint et al. (2004) showed the feasibility of this process. After a period of subduction, the upper crust may separate from the rest of the plate and because of its positive buoyancy it may return to the surface. This process depends on the rheology of the lower crust -that has to be relatively weak- and of course on the buoyancy. Ellis et al. (1999) investigated a small continental terrane entering the subduction zone after a period of sediment subduction. In their model (their experiment 5) the plate contact is described by a subduction channel with an initial thickness of 5 km. The continental terrane is dragged down beneath the upper plate. This finding is in agreement with our results, even though the rheological properties and the forces used in their experiment differ from ours. In their model they

investigate a larger amount of convergence than in our experiments: after 400 km convergence the weak upper crust of the terrane separates from the lithosphere and creates a large fold nappe. Chemenda et al. (1996) introduced inter-plate pressure as a pertinent parameter in the process of continental crust subduction. If the inter-plate pressure is low, the continental crust can be subducted to a depth of about 200 km and relatively easily exhumed. When the inter-plate pressure is high, failure of the crust occurs at shallower depth and exhumation is not so easy and not so fast. This finding has some similarity with our experiments: in our FMOw$_{15}$, where the inter-plate pressure is high and crustal strength weak, the continental crust fails, while the in CM, where the inter-plate pressure is low the crust is subducted. In FM, subduction of the upper crust is more difficult than in CM or does not take place at all. In conclusion, even though our models differ from Chemenda et al. (1996)'s analog experiments, the physical process behind them is very similar. Chemenda et al. (1996) vary the inter-plate pressure through the variation of the slab pull; in our modeling this is achieved through the variation of the plate contact type.
The previous studies pointed out which are the main parameters governing the evolution of continental subduction. The range in which these parameters vary is wide; continental collision can not be explained by a unique combination of parameters. With our models we show that the initial phase of the process is important and may control what will happen at longer time scales. The plate contact type is one of the variables to take into account. During the initial stage of continental collision the plate contact is more important than slab strength, subduction velocity and buoyancy. In the later stage of the process these last variables become important.

4.6 Discussion

4.6.1 Do subduction channel and fault plate contacts exist?

One of the questions arising from our models is whether it is possible to establish where, in nature, the plate contact is characterized by a fault or a channel. Several seismic observations have shown a low velocity layer at the plate interface, which in general is few km thick (Eberhart-Phillips & Martin, 1999; Oncken et al., 2003; Abers, 2005; Tsuru et al., 2002). This is interpreted in term of a subducting sediment channel. However, a subduction channel cannot be a proper description of all subduction zones. First, great subduction earthquakes suggest that the subduction interface cannot be weak everywhere (Davies & Brune, 1971; Kanamori, 1977; Ruff & Kanamori, 1983; Tichelaar & Ruff, 1993). Most inter-plate seismicity occurs in the depth range of 0-50 km (Tichelaar & Ruff, 1993), implying that at least the shallow part of the subduction zone has a finite shear strength. Second, sediment supply

varies from site to site as indicated by accretionary wedge dimensions and erosive margin observations (Clift & Vannucchi, 2004). This might suggest that when the amount of sediments is small, the subduction channel becomes so thin that a more appropriate description of the plate contact is by one or several faults. In general, when a continental margin approaches the trench a high quantity of sediments arrives at the subduction zone, increasing the possibility of a channel-like plate contact. On the other hand, erosion, that produces sediments, is influenced by tectonics, topography and climate. These factors change in time and as a consequence the amount of sediment changes, resulting in the possibility that subduction plate contacts evolve from one type into the other.
We could speculate that some tectonic settings may facilitate the creation of a subduction channel, e.g. in a land-locked basin setting in which it is easier to accumulate sediments. On the other hand, an open subduction setting, in which the subducting plate is pushed towards the trench, is likely to be represented by a fault. Unfortunately, we must conclude that for many subduction zones relevant information on the nature of the plate contact is lacking so far.

4.6.2 Comparison between our models and natural systems

The application of our numerical results to a natural system is restricted by the simplifications we made in our models. However, these idealized convergent systems yield some expressions that are similar to those observed in some continental collision systems. For instance, examples of the type of delamination we produce in our models (block/terrane accretion) may be represented by the Chugach terrane delaminated and accreted to the cratonic North America (e.g., Coney et al., 1980; Clift et al., 2005) or the accretion of the Hanshan and Xilin Hot micro-continents, part of the Turkestan ocean, to the Dongqiyishan arc. According to Kusky et al. (2007) this collision resulted in the formation of the North China Craton. An example of delamination and thrust accretion is the Qinling-Dabie Shan orogenic belt east of the Tanlu fault. The upper crust of the South China block thrust over the crust of the North China block followed by continuous subduction of the lower crust and upper mantle of the South China block underneath the North China block (Li, 1994). A similar process occurs in the Alps: the European plate subducts, while the Adriatic plate acts as a chisel scraping off the upper from the lower crust (Schmid et al., 1996).
In a general sense, understanding the possible variations in convergent plate boundaries evolution, as addressed in this study, helps interpreting observational data from such a setting. For example, in the nappe stacking of the continental basement of the Rhodope, there is ample evidence of ultra-high pressure metamorphism, suggesting that continental upper crust was dragged down to a depth of 70-80 km before being exhumed (Liati et al., 2002) . At least 900 km of continental lower crust and upper

mantle have been subducted without resulting in break-off (van Hinsbergen et al., 2005). This region is characterized by extension in the back-arc region. The CML seem to be a good setting to generate a Rhodope-type geological structure: the crust can be easily subducted and exhumed because of the low inter-plate pressure. The low inter-plate pressure helps both processes and promotes continuation of subduction. Moreover, in the land locked basin setting, the state of stress in the back arc region is compressive, but the compression is strongly reduced compared to the FM. We argue that an increase in channel thickness or a decrease in the viscosity value in the channel may result in extension in the back-arc region.
The fact that most of the above cited regions are characterized by the presence of ultra-high pressure rocks -that generally indicates the presence of a subduction channel- may be explained by taking into consideration that the nature of the plate contact may change in time, going from a channel to a fault and vice-versa.
Continental collision is highly three dimensional: the size of the continent in the out-of-plane direction affects the response of the process. However, we can infer three dimensional aspects from our 2D models. For instance, if in our models we predict subduction of the incoming continental margin or delamination of the upper crust, we can then infer that if the out-of-plane dimension of the incoming continent is small compared to that of the subducting plate, the subduction of the buoyant material or the removal of the upper crust is facilitated.

4.7 Conclusion

From a consistent comparison of channel and fault models, we find:
i) Channel models always promote coherent and steady state subduction of the continental fragment, irrespective of the geometry and strength of the continental crust of the incoming continent. In fault models, coherent subduction of the incoming continental material occurs if the continental rise of the colliding terrane is gentle. In this case, the approaching continental sliver starts to subduct and subduction is characterized by a non-plate-like behavior and strong deformation of the slab.
ii) Fault models result in locking of the trench and likely in subsequent slab break-off, if the margin of the terrane is steep and if the strength of its lower crust is high.
iii) The combination of a strong plate contact (i.e. fault), a steep slope angle and a low crustal strength of the incoming continental margin results in efficient shear delamination of the upper crust. The remaining lower crust and lithospheric mantle of the continental fragment continue to subduct. The subducting plate is characterized by a non-plate like behavior and strong deformation of the slab.
In summary our results indicate that the following types of responses can occur by solely varying the plate contact type:

1) Coherent subduction of the continental sliver. This mode is subdivided in two groups: plate-like continental subduction and non-plate-like continental subduction.
2) Shear crustal delamination of the upper crust of the incoming continental margin. Subsequent continuation of subduction in a non-plate-like fashion.
3) Locking of the subduction zone and possible development of slab break-off.
We conclude that initial stages of continental collision are strongly affected by whether the subduction contact is a fault or a channel. Neither the slab pull magnitude or tectonic setting is very important to the overall geodynamics at this stage. The plate contact type, along with the slope of the incoming passive margin and the rheology of the continent, decides whether the incoming crust (partially) overthrusts, subducts entirely, or blocks the trench leading to slab break-off.

4.8 APPENDIX D: Models for a land locked basin setting

In this section we show the strain rate distribution for the experiments in the land-locked basin setting in which there is no net convergence between the surface plates. We again use two different geometries to describe the incoming continental sliver: one with a continental slope inclination angle of 3 degrees and a steeper one with a continental slope inclination angle of 15 degrees. Figures 4.10a1-a5 display the total strain rate distribution, while Figures 4.10b1-b5 show the evolution of the average strain rate with time in two areas: solid black line corresponds to the solid circle in Figures 4.10a1-a5, red curve corresponds to the average crustal strain rate (red circle in Figures 4.10a1-a5).

4.8.1 Channel models (CM)

In this setup the plate contact is described by a low viscosity channel that extends to a depth of 100 km. The viscosity of the channel is $\eta = 2 \cdot 10^{18}$Pa·s.

Channel model with land-locked basin subduction boundary conditions and 3^0 continental slope inclination angle ($\mathbf{CML}_3$)

The strain rate distribution is displayed in Figure 4.10a1 at 0.64 My. The strain rate in the slab and in the continental crust of the incoming fragment has a small magnitude of about $1{\cdot}10^{15}\ s^{-1}$. The horizontal part of the subducting plate is characterized by a higher strain rate than in CMO (channel models with open subduction setting). In the entire model domain, the highest value of the strain rate is in the subduction channel and below the horizontal subducting plate. These two regions represent relative thin layers of rapidly deforming material. In Figure 4.10a1 the deformed geometry of the model shows that the continent has been dragged down with the subducting plate to a depth of about 12 km. In Figure 4.10b1, the average value of the strain rate shows a nearly stationary behavior as a function of time with a value of about $1{\cdot}10^{-15}\ s^{-1}$. The same holds for the crustal strain rate. However, in this region the strain rate is higher than in the slab. This is a consequence of the fact that the crust deforms while entering the trench.

Channel model with land-locked basin subduction boundary conditions and 15^0 continental slope inclination angle ($\mathbf{CML}_{15}$)

In this model, the continental slope of the margin is inclined at an angle of 15 degrees. The different geometry of the sliver slightly affects the behavior of the subduction process and the results are very similar to the previous model.

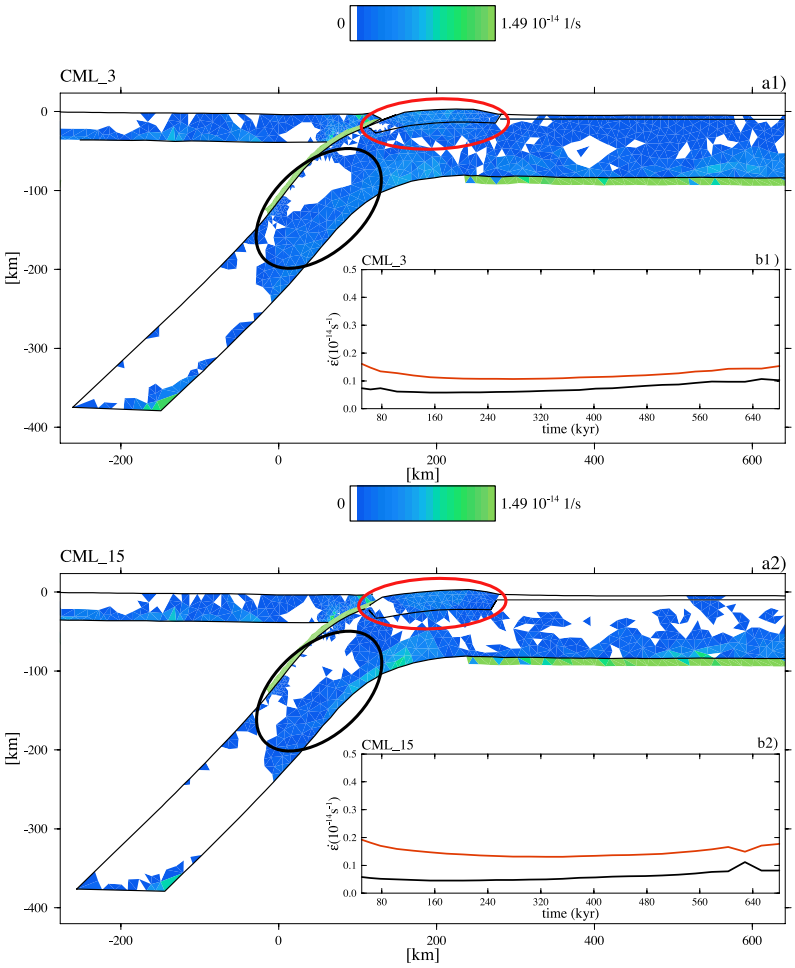

Figure 4.10: Effective strain rate at 640 kyr (a) and Effective strain rate evolution in time (b). Solid black curve corresponds to the region in the solid black circle in a, red curve corresponds to the red circle in a. a1 and b1 show strain rate for CML_3, a2 and b2 show the strain rate for CML_{15}.

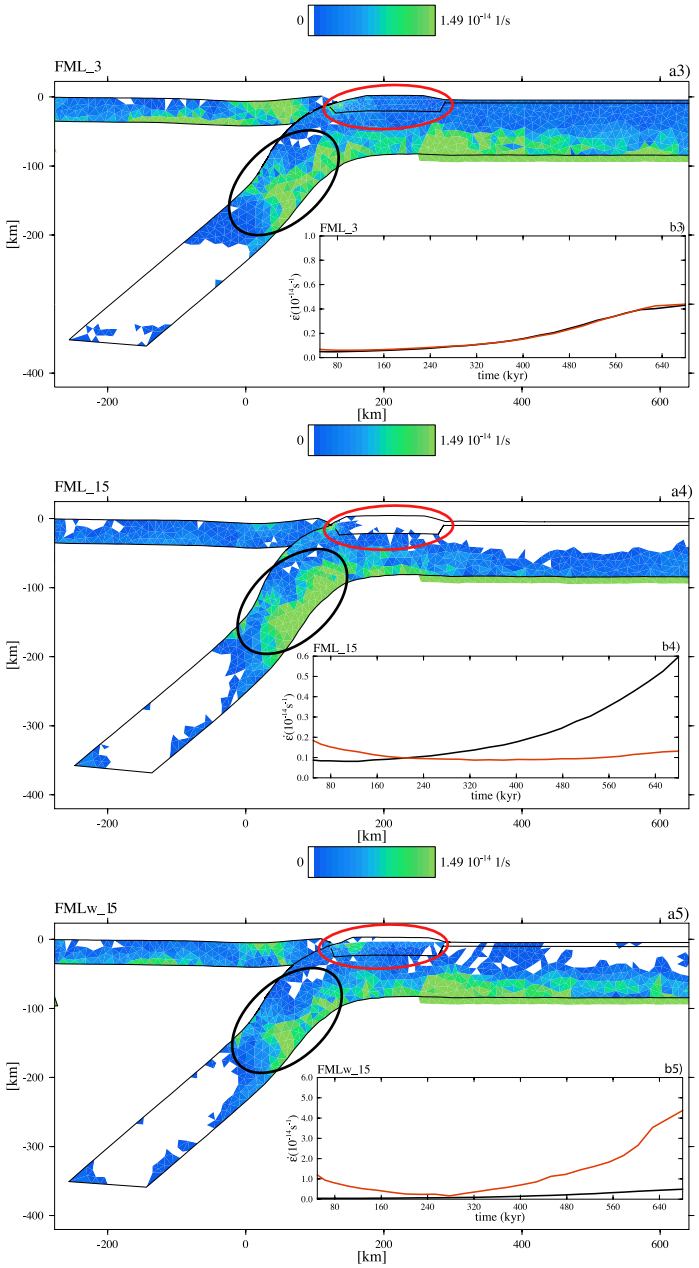

Figure 4.10: (Continued). Effective strain rate at 640 kyr (a) and Effective strain rate evolution in time (b). Solid black curve corresponds to the region in the black circle in a, red curve corresponds to the red circle circle in a. a3 and b3 show strain rate for FML_3, a4 and b4 for FML_{15} and a5 and b5 for $FMLw_{15}$.

Like in CML_3, the strain rate within the subducting plate is small (Fig. 4.10a2). Strain rate is high in the channel and beneath the oceanic surface plate. The deformed geometry of the model displays that the incoming continental fragment has been subducted to a depth of about 12 km. In Figure 4.10b2 the average value of the strain rate shows a nearly stationary behavior. The black curve in Figure 4.10b2 displays a response very similar to the previous model. In the crust the strain rate magnitude is slightly higher than in the slab. The fact that the average strain rate in the crust is higher than in CML_3 suggests that the continental crust experiences more deformation than the in previous model.
We performed an experiment in which the lower crust of the continental margin is characterized by low strength of 30 MPa ($CMLw_{15}$). Because the results are very similar to those the CML_{15}, we decided not to show them.

4.8.2 Fault Models (FM)

In this model the plate contact is described by a frictionless fault that extends to a depth of 100 km.

Fault model with land-locked basin subduction boundary conditions and 3^0 continental slope inclination angle (FML_3)

Figure 4.10a3 displays the total strain rate distribution at 0.64 My. The strain rate that develops in the slab, in the continental crust and in the overriding plate is higher than in the CML. The slab significantly deforms at a depth of about 150 km, where the strain rate is localized, but less than in FML_3. The deformed geometry of the domain shows that the incoming continental crust is subducted to a depth of about 4 km. The depth reached within the integration time by the subducting continent is shallower than in the CML. The overriding plate is characterized by high strain rate and marked down-welling. In Figure 4.10b3 the black and the red curves show that the average strain rate in the slab and in the crust of the incoming fragment increases with time, reaching higher values than in the previous models. Strain rate is high beneath the oceanic surface plate.

Fault model with land-locked basin subduction boundary conditions and 15^0 continental slope inclination angle (FML_{15})

The strain rate in the slab and in the overriding plate is higher than in the CML and in FML_3 (Fig. 4.10a4). From the deformed geometry of the model we notice that the incoming continent locks the trench and does not subduct with the oceanic material. The slab deforms more than in FML_3 at a depth of about 150 km, but less than in

FMO_{15}. The strain rate is higher than in FML_3. Figure 4.10b4 shows the average strain rate in more detail: the strain rate in the slab increases with time more than in FML_3 reaching a maximum value of about $0.6 \cdot 10^{-14}\ s^{-1}$. In the crust the strain rate is stationary and lower than in FML_3. Like in FML_3, the strain rate is high beneath the oceanic surface plate.

Fault model with land-locked basin subduction boundary conditions and 15^0 continental slope inclination angle and weak crustal layer ($FMLw_{15}$)

The strain rate distribution that develops in the slab and in the overriding plate is very similar to FML_3 (Fig. 4.10a5). The strain rate maximizes in the slab at a depth of about 150 km; at that depth the slab is deformed. A high strain rate region is visible in the crust of the continental margin. This is the expression of the shear delamination process, in which the upper crust separates from the lower one. The lower crust continues to subduct reaching a depth of about 4 km, during the modeled period. The detailed representation of the strain rate in Figure 4.10b5 indicates that the average strain rate in the slab increases with time but less than in FML_{15}. In the crust, the strain rate is one order of magnitude higher than in the slab and higher than in all other land-locked basin models.

Chapter 5

Nature of the plate contact and subduction zones diversity

We highlight the nature of the plate contact as an important physical feature of subduction zones and find that it is significantly correlated to the back-arc state of stress/strain as well as to the maximum seismic moment magnitude. We identify four classes of subduction zones. The first two classes follow directly from our numerical experiments in combination with a re-analysis of published observations. In class 1 subduction zones are characterized by a plate contact that is largely fault like with an accretionary margin. In class 2 the plate contacts are largely channel-type and have an erosive margin. The third class, where the plate contact is a channel entirely, consists of accretionary margins with a high sediment supply. Subduction zones of class 4, mostly characterized by an erosive convergent margin (northern Chili, Peru, Honshu and Kuril), are more complicated; however, they can be explained by incorporating regional observations.

5.1 Introduction

Earthquake intensity, back-arc state of stress, subduction velocity and sediment supply vary greatly from one subduction zone to the other. Understanding the mechanics and dynamics of the subduction process in view of these observed features represents a challenging problem of plate tectonics. Uyeda & Kanamori (1979) made one of the first attempts in subdividing subduction zones, classifying them in Marianas or in

This chapter has been submitted for publication to *Earth and Planetary Science Letters* as: R. De Franco, R. Govers and R. Wortel, Nature of the plate contact and subduction zones diversity

Chilean types. In the first case, the back-arc region shows extension, while in the second case compression prevails. Chilean types are characterized by very strong thrust earthquakes, while Marianas types are not. Uyeda & Kanamori (1979) suggested that different subduction types result from different levels of coupling between the subducting and the overriding plate. The idea of Uyeda & Kanamori (1979) was confirmed by Conrad et al. (2004); subduction zones that produce great earthquakes, such as those in Chile or Alaska, typically exhibit significant back-arc compression while those that are seismically uncoupled, such as Marianas, typically display back-arc spreading.

Convergent margins can be roughly classified into accretionary margins and erosive margins (e. g., Von Huene & Scholl, 1991, 1993; Clift & Vannucchi, 2004). Accretion transfers material from the subducting plate to the forearc wedge and plate boundary zone. It enlarges the accretionary prism and is accompanied by sediment subduction. Accretion can be more or less active depending on the sediment delivery rate and material subduction rate and it is favored at low subduction rates (Le Pichon et al., 1993). Subduction erosion is defined as the process that causes a net loss of material from the hanging wall. In this case the wedge volume is stationary or decreases with time (Lallemand et al., 1994). Lallemand et al. (1994) classified subduction erosion in two types, frontal and basal tectonic erosion. Frontal erosion takes place near the trench, and is thought to be due to the grabens or to ridges and seamounts. Basal tectonic erosion occurs at the base of the upper plate in a low friction environment, and might be due to a fast convergence rate that results in hydrofracturing by overpressuring. Such a first order classification into convergent and erosive margins neglects some of the observed variability of individual subduction plate contacts; a margin can evolve from one type into the other, or the plate contact may vary laterally. Accretion at the toe and erosion may occur simultaneously like, for example, in Japan and Peru (Von Huene & Lallemand, 1990).

Trying to explain the dichotomy between the seismically active Chilean and the aseismic Marianas subduction zones, Cloos & Shreve (1996) suggested that Chilean-type margins typically have thick trench fills and that the plate boundary zone thins arcwards, while Marianas type margins have a thin or non-existent accretionary prism and the plate contact zone thickens with depth. They suggest that sea-mounts are subducted entirely to become seismogenic asperities in the Chilian type margin, while in the Marianas type just a truncated part of the sea-mount enters the subduction. This truncation, in combination with the thick subduction channel, precludes subducted seamounts from becoming seismogenic asperities. Erosional margins are thus seismically quiescent, and accretionary margins exhibit high seismic moment release rates. Observational backup of this idea is good, although there exist some exceptions.

Over the years several data sets have been systematically compiled and analyzed in order to understand the dynamics of subduction zones and to reveal the relation between different observables (e.g., Jarrard, 1986; Clift & Vannucchi, 2004; Lallemand et al., 2005; Sdrolias & Muller, 2006). Seismic studies became more accurate, able to show new features at the subduction zones like the presence of inter-plate channel-like units of about 1-8 km thickness (Eberhart-Phillips & Martin, 1999; Oncken et al., 2003; Abers, 2005; Tsuru et al., 2002). Through inversion of arrival times from local earthquakes, these authors found an anomalous zone of low velocity at the interface between the plates. However, the arrival-time inversion can not resolve the thickness and the character of the layer independently. Investigation of the crustal fore-arc structures with wide-angle seismic data showed narrow, low velocity zones at the base of the fore-arc wedge, suggesting the existence of subduction channels in Costa Rica, Makran, Nankai, Chile, Peru (Christeson et al., 1999; Kopp et al., 2000; Takahashi et al., 2003; Patzig et al., 2002). These data do not have the resolution to identify accurate subduction-channel geometries. Reflection seismic profiles from some of these fore-arcs give more accurate results; the disadvantage of these experiments is that they trace the subduction channel just to shallow depth (e.g., Von Huene et al., 2004; Ranero & von Huene, 2000).

The increasing evidence for variability of the plate contact motivated us to study its imprints on the overall subduction process (De Franco et al., 2007a, Chapter 3 of this thesis). Through geodynamic numerical modeling we demonstrate that the overall plate contact nature has a dominant control. In these models the entire plate contact is considered. We further investigated the role of the plate contact on the dynamic evolution following the arrival of a terrane at the trench (De Franco et al., 2007b, Chapter 4 of this thesis).

In this study we shed new light on the geodynamics of subduction, based on the physical insights from our numerical experiments (De Franco et al., 2007a, 2007b) in combination with a re-analysis of published observations (Abers, 2005; Lallemand et al., 2005; Clift & Vannucchi, 2004). Our synthesis elucidates relations between back-arc state of stress, maximum seismic moment magnitude, and the nature of the all subduction plate contact, that affects the coupling level between overriding and subducting plate. Building on this, we identify four classes of subduction zones using observed back arc strain, nature of the convergent margin (erosive or accretionary) and maximum seismic moment magnitude. In doing this, we combine large scale features of subduction zones, following the approach of Uyeda & Kanamori (1979), with more regional observations as proposed by Cloos & Shreve (1996).

5.2 Data and correlations

The mean shallow (depths between 0-125 km) and the mean deep (depths greater than 125 km) dip angle are correlated with other characteristic parameters like the back-arc deformation and the nature of the plate contact. Recently it has been established that the size of the low velocity anomaly at the top of the slab, correlates well with the average slab dip angle (Abers, 2005). Bodywave speeds decrease with increasing subduction angle at seven subduction zones: Aleutian (Ale), Alaska (Ala), Hokkaido-South Kurile (Hok-S.Kur), North Honshu (N. Hon), Marianas (Mar), Nicaragua (Nic), North Kurile-Kamchatka (N. Kur-Kam). Waveguide thicknesses vary between 2-8 km with large uncertainties. The velocity anomaly is as large as 14 $\%$, indicating that the waves within this layer propagate much more slowly than in the surrounding mantle. Between different subduction zones, the velocity anomaly varies by a factor of 2-3 down to 150 km depth.

The low velocities may be explained by either metastable gabbro, that represents an essential part of the oceanic crust, or low temperature hydrated mafic rocks that represent subduction channel-type rocks. This last hypothesis is plausible because slabs seem to dewater constantly during subduction (Rupke et al., 2004). Quantitative experimental studies on rheology show that plastic deformation of upper mantle minerals is significantly intensified by the presence of water (e.g., Karato et al., 1986; Mei & Kohlstedt, 2000), suggesting that at higher water fugacity conditions weakening effects may be quite pronounced. In this way it is possible to relate the low velocity to the rheology of the material. Numerical modeling experiments support also a correlation between viscosity reduction in the subduction channel and increasing slab dip angle (Manea & Gurnis, 2007). Note however, that the thickness of the subduction channel trades off with the seismic velocity anomaly: a thicker subduction channel with a relatively low velocity anomaly is analogous to a thinner channel with a higher velocity anomaly.

In addition to the correlation between nature of the plate contact and dip angle, a strong correlation between back-arc deformation and subduction dip angle has been inferred (Lallemand et al., 2005). Back-arc spreading is observed for deep dip angles larger than 51°, whereas back-arc shortening occurs for deep dip angles smaller than 31°.

When taken together, these correlations suggest that there is also a correlation between back-arc strain state and the rheological properties of the plate contact (see Fig. 5.1a and see also Chemenda et al. (2000)). In order to quantify this relation we calculate the correlation coefficient between the nature of the plate contact and the back-arc strain (Abers, 2005). The plate contact nature is parameterized by the velocity anomaly $dlnV_p = \frac{V_p - V_0}{V_0}$, where V_p is the P wave velocity and V_0 is the reference

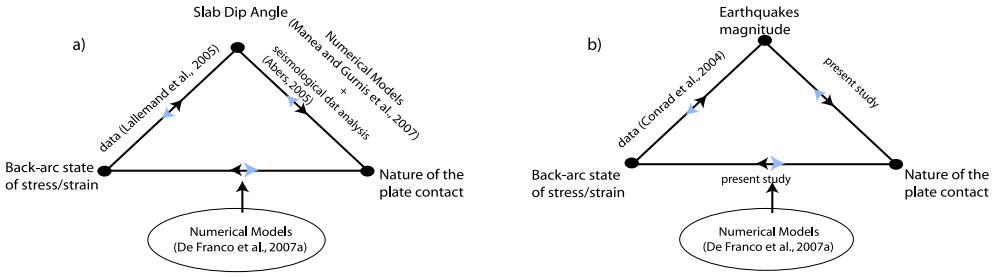

Figure 5.1: a) Schematic representation of the relations between back-arc state of strain, slab dip angle and nature of the plate contact. b) Schematic representation of the relations between back-arc state of strain, earthquakes magnitude and nature of the plate contact.

P wave velocity). Nicaragua is not included because the back-arc state of strain is not provided by Lallemand et al. (2005). The correlation coefficient for the data points shown in Figure 5.2 is $R = -0.83$. However, the seismic velocity anomalies have uncertainties (see Abers (2005)). Therefore we test the robustness of the correlation by simply adding random noise (see the error bars) to the data points and evaluate the correlation coefficient for 1000 possible realizations. From the resulting distribution of correlation coefficients we compute the cumulative probability distribution (Fig. 5.2 b). 83 $\%$ of the 1000 correlation coefficients have a value lower than $R = -0.8$, indicating that the velocity jump is negatively correlated with the back arc state of strain (see Fig. 5.2 b). We conclude that the weaker the rheology of the subducting channel the more extensive the back-arc region.

Our numerical experiments show a similar correlation (De Franco et al., 2007a). In these geodynamic models, we link the nature of the plate contact and the back-arc state of stress (tensional stress corresponds to extensional strain). The type of plate contact controls the dynamic response of the upper plate, drives the displacement of the overriding plate and, as a consequence, the stress distribution. In Figure 5.3 we show the horizontal stress at the surface of five different models. A clear trend from high compressive to low compressive back-arc stress is visible moving from a fault model (black curve) to a weak subduction channel model (red curve). These four models are taken from (De Franco et al., 2007a) whereas the yellow curve represents a new model in which the thickness of the channel is increased, while the viscosity is the same as in the model shown by the red curve. The effect of the increased thickness is to ulteriorly reduce the back-arc compression. We extrapolate that further increasing the thickness of the channel or further decreasing the viscosity in the channel will eventually lead to a tensile back-arc state of stress. In all these models a low viscosity wedge (LVW) is adopted above the subducting slab (e.g., Billen & Gurnis, 2001; Kelemen et al., 2004; Currie et al., 2004). The LVW is likely due to

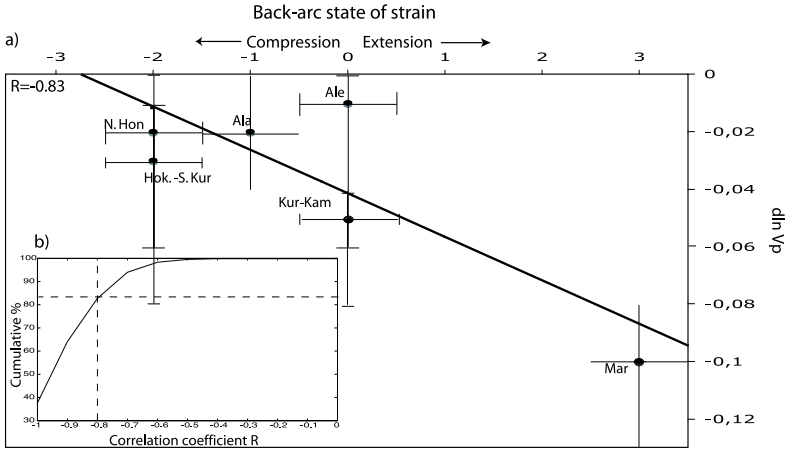

Figure 5.2: a) Best fitting line in the least square sense between the back-arc state of strain (Lallemand et al.,2005) and the relative velocity variation within the plate contact (dlnVp, Abers, 2005). b) Cumulative probability distribution of R computed from 1000 noisy data points, showing that 85 $\%$ of the 1000 correlation coefficients have a value less than or equal to -0.8.

the presence of water released from the subducting slab or to melting processes at the base of the arc crust.

In the last part of this section we investigate the relation between the nature of the plate contact and seismicity. Recently, Conrad et al. (2004) found that there is a positive correlation between back-arc state of strain and the maximum seismic moment release, meaning that strong earthquakes are characteristic for subduction zones with a compressive back-arc. This correlation, in combination with the relation between back-arc deformation and the nature of the plate contact, suggests that the nature of the plate contact and the maximum seismic moment are linked (see Fig. 5.1 b). In order to show this relation, we analyze 7 subduction zones for which the velocity anomaly is given by Abers (2005). We use the maximum seismic moment magnitude for each of these subduction zones between 1904 and 2007 taken from the USGS catalog. The resulting data points are shown in Figure 5.4a together with the best fitting line. The correlation coefficient is $R = 0.92$. Repeating the same procedure as before we compute the cumulative probability distribution of the correlation coefficient from 1000 noisy realizations. We find that 80 $\%$ of the 1000 correlation coefficients have a value higher than $R = 0.82$, indicating that the velocity anomaly is robustly correlated with the greatest moment release (see Fig. 5.4b). Note that these correlations display a basic trend that expose a relationship between two parameters. We do not expect perfect correlation because of the complexity of the subduction process

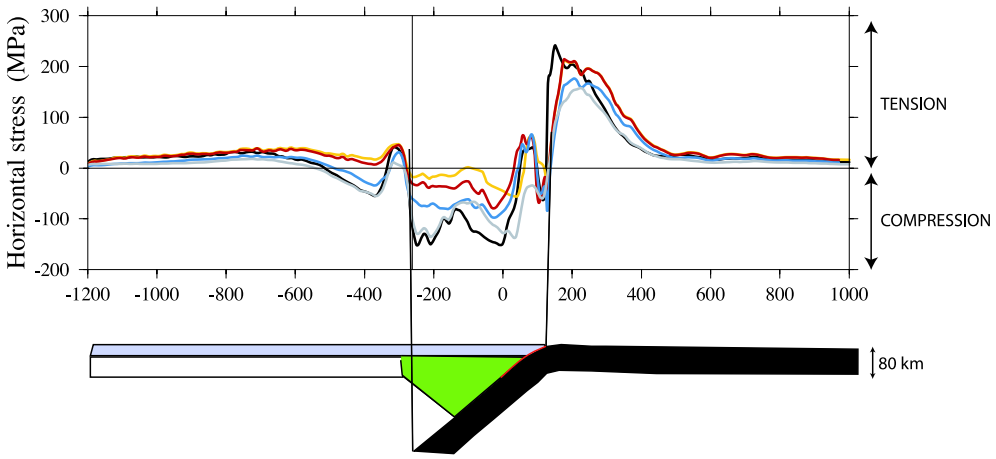

Figure 5.3: Horizontal stress at the free surface of five subduction models. Compression is negative. The solid black line represents frictionless fault model, the grey line a fault model with friction, the blue line a high viscosity channel model, the red line low viscosity channel model and the yellow line a low viscosity channel with a greater thickness. Bottom: subduction geometry used in the numerical experiments. The green region represents a low viscosity wedge. The plate contact reaches 100 km depth for both channel and fault models (red line). This is in agreement with Kneller et al. (2005). On the basis of heat flow data, seismic attenuation, and velocity tomography, they conclude that the fully coupling point cannot be shallower than 70 km.

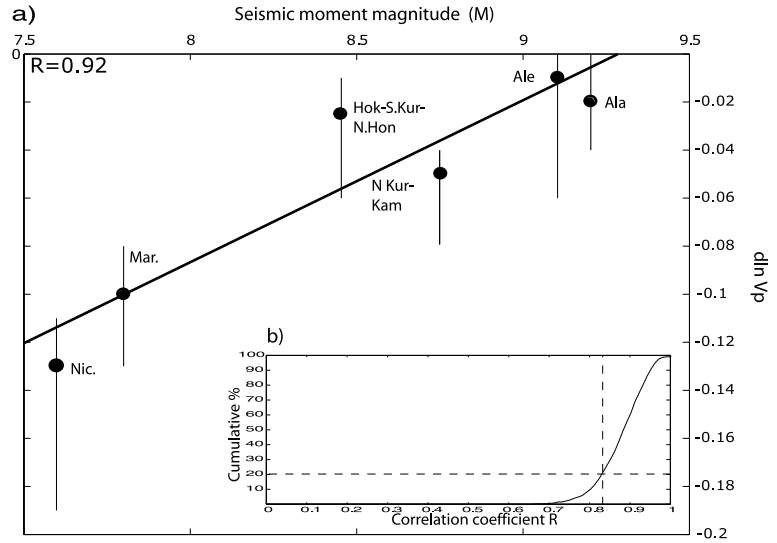

Figure 5.4: a) Best fitting line in the least square sense between the greatest seismic moment (M) and the relative velocity variation within the plate contact (dlnVp, Abers, 2005). dlnVp value of point Hok-S.Kur-N.Hon is an average between the value given for Hokkaido-S. Kurile and N. Honshu. b) Cumulative probability distribution of R computed from 1000 noisy data points, showing that 80 $\%$ of the 1000 correlation coefficients have a value greater than or equal to 0.82.

and the small amount of data.

In summary, compression in the back-arc region and strong earthquakes prevail for a high viscosity subduction channel or for a very thin channel (represented by a fault) in which the body wave velocity anomaly is small. Lower compression or eventually tension and weak earthquakes prevail for a weak or wide channel with relative weak material fill, where the body wave velocity anomaly is more pronounced.

5.3 A new subduction zone classification

In a global view of subduction zones, another key discriminating physical feature is the accretionary or erosive nature of the margin. Accretionary and erosive margins have characteristic shallow features which we aim to link with the deeper part of the plate contact. Cloos & Shreve (1996) suggested that in accretionary margins, characterized at shallow depth by thick trench fills, tall sea mounts are subducted entirely. In erosive margins, characterized at shallow depth by thin trench fills, only

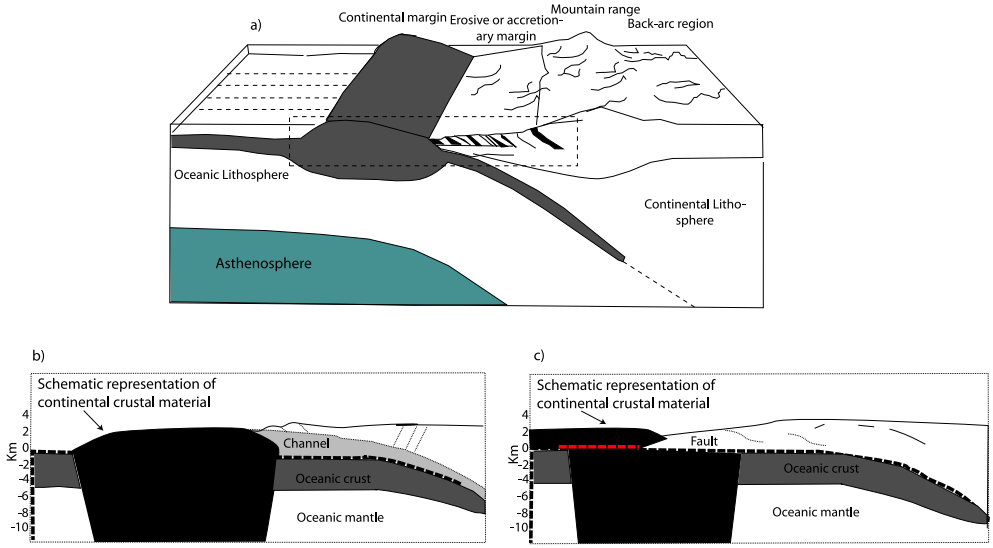

Figure 5.5: a) General representation of a topographic feature approaching a subduction zone. The dashed rectangle is shown enlarged in b and c. b) Schematic representation of an approaching topographic feature in a subduction channel-type model: subduction of the entire continental crust takes place. c) Approaching topographic feature in a subduction fault-type: truncation of part of the continental crust takes place.

truncated sea-mounts are subducted.

Our numerical models (De Franco, 2007b) also shed light on the behavior of sea mounts upon subduction. A topographic feature (in the numerical model it is represented as a continental fragment) approaching the trench is entirely subducted in the presence of a wide and weak subduction channel (see Fig 5.5b). In a fault type model, subduction of a steep topographic feature does not occur without previous delamination of the upper part of the incoming fragment (see Fig 5.5c and De Franco et al. (2007b)). Our models confirm the idea of Cloos and Shreve (1996) if we equate the shallow subduction channel in the model to an accretionary margin, and if we interpret the shallow part of the model subduction fault as an erosive margin.

According to Cloos & Shreve (1996), as we move deeper down along the plate contact, the shear zone becomes thinner in accretionary margins, while in erosive margins the shear zone thickens. Using the correlation between the back-arc state of stress and the nature of the plate contact found in the previous section, we infer that the back-arc state of stress is compressive in accretionary margins and tensional in erosive margins. To investigate the validity of such an interpretation we link the type of convergent margins and the back-arc state of strain of several subduction zones using the

a)

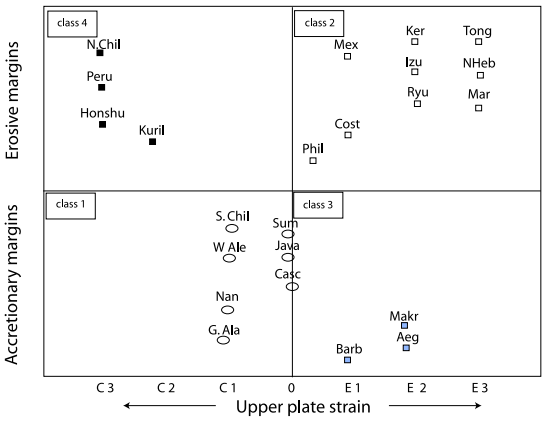

b)

Subduction zone	Seismic moment magnitude	Class
SChile (S.Chil)	9.5	1
Alaska (Ala)	9.2	
Aleutians (W.Ale)	9.1	
Sumatra (Java-Sum)	9.1	
Cascadia (Casc)	9.0	
Japan (Nan)	8.4	
Central America (Mex-Cost)	8.1	2
New Hebrides (NHeb)	7.9	
Marianas (Mar)	7.8	
Izu-Bonin (Izu)	7.2	
Philippines (Phil)	7.9	
Tonga (Tong)	8.0	
Kermadec (Ker)	7.4	
Ryukyus (Ryu)	8.0	
Lesser Antilles (Barb)	7.5	3
Aegean arc (Aeg)	7.1	
Makran (Mak)	8.0	
Peru (Peru)	8.4	4
Japan (Honshu)	8.4	
Kurile (Kur)	8.5	
N.Chile (N.Chil)	8.5	

Figure 5.6: a) Level of back-arc strain for different types of convergent margins. On the horizontal axis C means compression, 0 means neutral E means extension. The scale from strong back-arc compression to strong back-arc spreading is according to Lallemand et al.,2005 C3, C2, C1, 0, E1, E2, E3, with the exception of the Aegean arc and Makran taken from Jarrard (1986) and McCall (1997) b) A list of subduction zones with their maximum seismic moment magnitude.

data of Clift & Vannucchi (2004) and Lallemand et al. (2005) (see Fig. 5.6a). We identify four different classes, in which the margins are either accretionary or erosive, in combination with either extension or compression in the back-arc region (see Fig. 5.6). As expected, most of the accretionary margins are characterized by back-arc compression (class 1), while the erosive margins mostly have an extensive back-arc state of strain (class 2). These two classes directly follow from our numerical results and from the previously established correlation between back-arc state of strain and nature of the plate contact. We show cartoons of these two types of margins in Figure 5.7 a and Figure 5.7 b, respectively, in which the entire plate contact is shown.

Not all the accretionary margins show the same behavior and there are some evident exceptions (see Fig. 5.6). For instance, Aegean arc, Makran and Barbados are characterized by extension (class 3). Albeit less straightforwardly than for the first two classes, the results of the previous section and of De Franco et al. (2007a, 2007b) also account for the behavior of subduction zones of class 3. Our results imply that a weak and wide subduction channel characterizes the entire plate contact. For the margins of class 3, the fact that the sediment delivery rate and the material subduction rate

are higher than for the other margins (the sediment delivery rate is between 131 and 179 km^3/yr and the subduction material rate is between 109 and 150 km^3/yr (Clift & Vannucchi, 2004)), accounts for the presence not only of an accretionary wedge at the inlet, but also of a thick sedimentary channel that decouples the two plates along the entire plate contact (Figure 5.7 c).

Class 4 represents a more complicated case. In order to offer a possible explanation we need to supplement our results with additional information from various regional observational studies. The erosive margins of this class, contrary to the ones of class 2, are characterized by very strong compression (Fig. 5.6 a). As a consequence we would expect the deeper part of the plate contact to be described by a fault or, alternatively, by a channel with a small velocity anomaly (equivalent to a high viscosity channel). In the past, this kind of erosive margins has been envisaged as strongly coupled subduction zones where the erosion is due to high frictional abrasion. For instance, in the North Chile subduction zone, characterized by the downgoing plate covered with less than 100 m of pelagic sediment, a sediment starved trench, and earthquakes of $M_w = 8.0$ was indicated as a typical example of such highly frictional margins. However, recent studies on North Chile have shown that some water is incorporated in the sediments at the plate contact. Despite sediment starvation, a frontal prism, constructed of debris, elevates pore pressure to reduce interplate friction. Therefore, processes other than high frictional abrasion are required to explain subduction erosion along northern Chile (e.g. hydrofracturing) and as a consequence a thick plate contact is expected. Therefore, the presence of strong back-arc compression instead of extension might be due to a change of the physical properties along the subduction channel: the material becoming stronger with depth due to dewatering, results in a strong coupling between the plates. We propose, based on our model results (De Franco et al., 2007a, 2007b) and the correlation between back-arc state of strain and nature of the plate contact, that the North Chile-type plate contact can be described by a subduction fault at shallow depth, followed deeper down by a subduction channel in which the viscosity increases with depth (Fig. 5.7 d).

We propose another possibility that explains the anomalous behavior of class 4. In Peru and North Japan, accretion and erosion are simultaneously occurring (Von Huene & Lallemand, 1990). Accretion at the toe is active and erosion consumes the overriding plate generating subsidence further back. High friction erosional mechanisms generally proposed for these margins are not sufficient to explain the measured amount of eroded material (Von Huene & Lallemand, 1990). As a consequence, frontal erosion -due to the Nazca Ridge for Peru and the Daiichi Kashima seamount for Japan- and basal hydrofracturing are invoked. Subduction of a seamount or of a ridge is indicated as one of the reasons that can make an accretionary margin erosive. Since accretion is still active, part of the incoming sediments are used to create the accre-

tionary wedge, decreasing the already low percentage of subducted sediments. We may speculate that in these cases the plate contact is characterized by a relatively wide inlet (accretionary margin) in which topographic features are subducted, followed at shallow depth by a thin plate contact where the coupling between the plates results in back-arc compression; deeper down, the plate contact enlarges again as a consequence of the sediment produced by basal erosion. Based on our numerical results (De Franco et al., 2007a, 2007b), we suggest that the Peru type of margin can best be described as changing with increasing depth from a subduction channel to a fault (that couples the plates), back to a subduction channel (Fig. 5.7 e).

From the previous section, we know that strong earthquakes correlate with a thin or wide-and-strong plate contact and back-arc compression, whereas small earthquakes correlate with a wide-and-weak plate contact and back-arc extension. Therefore we expect to have big earthquakes in classes 1 and 4, and small earthquakes in classes 2 and 3. In order to confirm this theory, we compile a list of the greatest seismic moment magnitudes for the considered subduction zones (Fig. 5.6 b). The results substantiate our predictions: class 1 has $9.0 \leq M \leq 9.5$ with the only exception of Japan , class 2 has $7.2 \leq M \leq 8.1$, class 3 has $7.1 \leq M \leq 8$ and class 4 has $8.4 \leq M \leq 8.5$.

According to Cloos & Shreve (1996), class 1 is characterized by strong earthquakes, since the subducted seamounts become seismogenic asperities when they enter in contact with the upper plate. In class 2 the subducted truncated sea-mounts generate small earthquakes, since they do not touch the roof of the wide channel (see Fig. 5.7 a and b).

In the North Chilean subduction zone (class 4), Sallares & Ranero (2005) propose the release of elastic energy stored in the high viscosity channel as an explanation for the strong earthquakes. In the Peru/Japan type margin (class 4), the strong earthquakes are possibly caused by the nucleation of seamounts where the plate contact becomes thinner, in a similar fashion than in the accretionary margins. This can even happen at very shallow depth resulting in shallow earthquakes that cause tsunamis.

5.4 Conclusions

We highlight the nature of the plate contact as an important physical feature of subduction zones and find that the nature of the plate contact is correlated to the back-arc state of stress/strain as well as to the maximum seismic moment. We identify four subduction zone classes. The first two classes directly follow from our numerical results and the established correlations in combination with the observed nature of the convergent margin (accretionary or erosive). Although less straightforwardly than for the first two classes, our results also account for the behavior of subduction zones of

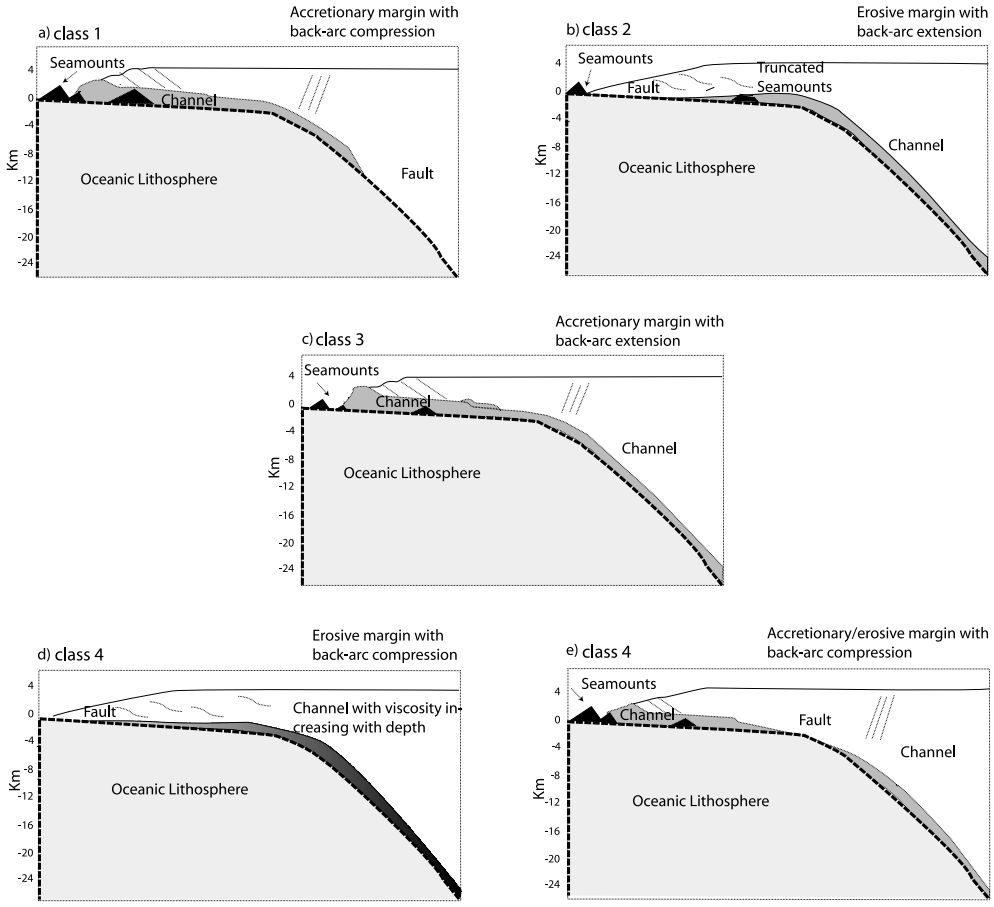

Figure 5.7: Classification of subduction (1-4), with two alternatives for class 4. The cartoons represent the enlargement of the dashed rectangle in Fig.5.5 a. a) accretionary margin with back-arc compression. b) erosive margin with a back-arc in extension. c) accretionary margin with back-arc extension. d) erosive margin with back-arc compression and increasing viscosity in the channel e) erosive margin with back-arc compression and active accretion process.

class 3. Class 4 represents a more complicated case. The main characteristics of each class are listed below:
Class 1: The entire plate contact is well described by a wide channel at shallow depth and a fault at greater depth. This class is formed by accretionary margins mostly in back-arc compression with very strong earthquakes.
Class 2: The entire plate contact is a combination of a fault (at shallow depth) and a subduction channel (at greater depth). This class is formed by erosive margins generally characterized by back-arc extension and small earthquakes.
Class 3: The entire plate contact is represented by a weak subduction channel. This class is formed by accretionary margins that exhibit back-arc extension and small earthquakes. These margins are characterized by a high sediment subduction rate.
Class 4: We propose two explanations for these kinds of margins. One possibility is that the eroded material at the plate contact becomes stronger with depth, due to dewatering. In this case the plate contact is represented by a fault at shallow depth followed by a subduction channel characterized by an increasing viscosity with depth. Alternatively, in case accretion is active together with erosion (e.g., Peru and North Japan), we suggest that the plate contact can best be described as changing with increasing depth from a subduction channel to a fault (that couples the plates), back to a subduction channel. This class is formed by erosive margins that show back-arc compression and strong earthquakes.

REFERENCES

Abers, G. A., 2005. Seismic low-velocity layer at the top of subducting slabs: observations, predictions, and systematics, *Phys. Earth Planet. Inter.*, **149**(1-2), 7–29.

Austrheim, H., 1987. Eclogitiziation of lower crust granulites by fluid migration through shear zones, *Earth Planet. Sci. Lett.*, **81**, 221–232.

Barazangi, M., Isacks, B. L., Oliver, J., Dubois, J., & Pascal, G., 1973. Descent of lithopshere beneath New Hebrides, Tonga Fiji and New Zeland: Evidence for detached slabs, *Nature*, **242**(5393), 98–101.

Beaumont, C., Ellis, S., & Pfiffner, A., 1999. Dynamics of sediment subduction-accretion at convergent margins: Short-term modes, long-term deformation, and tectonic implications, *J. Geophys. Res.*, **104**(B8), 17573–17601.

Becker, L. E., Mckinley, G. H., Rasmussen, H. K., & Hassanger, O., 1994. The unsteady motion of a sphere in a viscoelastic fluid, *J. Rheol.*, **38**, 377–403.

Billen, I. B. & Gurnis, M., 2001. A low viscosity wedge in subduction zones, *Earth Planet. Sci. Lett.*, **193**(1-2), 227–236.

Bird, P., 1978. Initiation of intracontinental subduction in the Himalya, *J. Geophys. Res.*, **83**, 4975–4987.

Bird, P., 1979. Continental delamination and the Colorado Pateau, *J. Geophys. Res.*, **84**, 7561–7571.

Blanco, M. J. & Spakman, W., 1993. The p-wave velocity structure of the mantle below the iberian peninsula - evidence for subducted lithosphere below southern spain, *Tectonophysics*, **221**(1), 13–34.

Bodart, C. & Crochet, M. J., 1994. The time dependent flow of a viscoelastic fluid around a sphere, *J. Non-NewtonianFluid Mech.*, **54**, 303–329.

Bott, M. H. P., Waghorn, G. D., & Whittaker, A., 1989. Plate boundary forces at subduction zones and trench-arc compression, *Tectonophysics*, **170**, 1–15.

Boutelier, D., Chemenda, A., & Jorand, C., 2004. Continental subduction and exhumation for high-pressure rocks: insights frim thermo-mechanical laboratory modelling, *Earth Planet. Sci. Lett.*, **222**, 209–216.

Braun, J. & Sambridge, M., 1994. Dynamical Lagrangian Remeshing (DLR): A new algorithm for solving large strain deformation problems and itsapplication to the fault-propagation folding, *Earth Planet. Sci. Lett.*, **124**, 211–220.

Brooks, A. N. & Hughes, T. J. R., 1982. Streamline upwind/Petrov-Galerkin formulations for convection dominated flows with particular emphasis on the incompressible Navier-Stokes equations, *Computer Methods in Applied Mechanics and Engineering*, **32**, 199–259.

Buiter, S., Govers, R., & Wortel, M. J. R., 2001. A modelling study of vertical surface displacements at convergent plate margins, *Geophys. J. Int.*, **147**, 415–427.

Byerlee, J., 1978. Friction of rocks, *Pageoph*, **116**, 615–626.

Chase, C. G., 1978. Extension behind island arcs and motions relative to hotspots, *J. Geophys. Res.*, **83**, 5380–5387.

Chatelain, J. L., Molnar, P., Prevot, R., & Isacks, B., 1992. Detachment of part of the downgoing slab and uplift of the New Hebrides (Vanatau) islands, *Geophys. Res. Lett.*, **19**(14), 1507–1510.

Chemenda, A., Lallemand, S., & Bokun, A., 2000. Strain partitioning and interplate friction in oblique subduction zones: Constraints provided by experimental modeling, *J. Geophys. Res.*, **105**(B3), 5567–5581.

Chemenda, A. I., Mattauer, M., Malavieille, J., & Bokun, A. N., 1996. A continental subduction and mechanism for exhumation of high-pressure rocks: new modelling and field data from Oman, *Earth Planet. Sci. Lett.*, **143**, 173–182.

Chopin, C., 2001. Coesite and pure pyrote in high-grade blueshists of the western Alps: a first record and some consequences, *Contribution to Mineralogy and Petrology*, **86**, 107–118.

Christeson, G. L., McIntosh, K. D., Shipley, T. H., Flueh, E. R., & Goedde, H., 1999. Structure of the Costa Rica convergent margin, offshore Nicoya Peninsula, *J. Geophys. Res.*, **104**(B11), 25443–25468.

Clift, P. & Vannucchi, P., 2004. Controls on tectonic accretion versus erosion in subduction zones: Implications for the origin and recycling of the continental crust, *Rev. Geophys.*, **42**(2), RG2001.

Clift, P. D., Pavlis, T., DeBari, S. M., Draut, A. E., Rioux, M., & Kelemen, P. B., 2005. Subduction erosion of the jurassic talkeetna-bonanza arc and the mesozoic accretionary tectonics of western north america, *Geology*, **33**(11), 881–884.

Cloos, M., 1993. Lithospheric buoyancy and collision orogenesis: Subduction of oceanic plateaus, continental margins, island arcs, spreading ridges and seamounts , *Geol. Soc. Am. Bull.*, **86**, 715–737.

Cloos, M. & Shreve, R. L., 1988. Subduction channel model of prism accretion, melange formation, sediment subduction, and subduction erosion at convergent plate margins: 2. Implications and discussion, *Pageoph.*, **128**, 501–545.

Cloos, M. & Shreve, R. L., 1996. Shear zone thickness and the seismicity of Chilean- and Mariana-type subduction zones, *Geology*, **24**(2), 107–110.

Conder, J. A., 2005. A case for hot slab surface temperatures in numerical viscous flow models of subduction zones with an improved fault zone parameterization, *Phys. Earth Planet. Inter.*, **149**(1-2), 155–164.

Coney, P. J., Jones, D. L., & Monger, J. W. H., 1980. Cordilleran suspect terranes, *Nature*, **288**(5789), 329–333.

Conrad, C., Bilek, S., & Lithgow-Bertelloni, C., 2004. Great earthquakes and slab pull: interaction between seismic coupling and plate-slab coupling, *Earth Planet. Sci. Lett.*, **218**(1-2), 109–122.

Currie, C. A., Wang, K., Hyndman, R. D., & He, J. H., 2004. The thermal effects of steady-state slab-driven mantle flow above a subducting plate: the cascadia subduction zone and backarc, *Earth Planet. Sci. Lett.*, **223**(1-2), 35–48.

Davies, G. F. & Brune, J. N., 1971. Regional and global fault slip rates from seismicity, *Nature*, **229**, 101–107.

Davies, J. H. & von Blanckenburg, F., 1995. Slab breackoff: A model of lithosphere detachment and its test in the magmatism and deformation of collision orogens, *Earth Planet. Sci. Lett.*, **129**, 85–102.

De Franco, R., Govers, R., & Wortel, R., 2007a. Numerical comparison of different convergent plate contacts: subduction channel and subduction fault, *Geophys. J. Int.*, **271**(1), 435–450. Chapter 3 of this thesis.

De Franco, R., Govers, R., & Wortel, M. J. R., 2007b. Dynamics of continental collision: Influence of the plate contact, *Geophys. J. Int.*, **submitted**, Chapter 4 of this thesis.

Dewey, J. F., Ryan, P. D., & Andersen, T. B., 1993. Orogenic uplift and collapse, crustal thickness, fabrics and metamorphic phase changes: The role of eclogies, in *Magmatic processes and plate tectonics*, edited by H. M. Prichard, T. Alabaster, N. B. W. Harris, & C. R. Neary, no. 76 in Geol. Soc. Spec. Publ, pp. 325–343, Geol. Soc. of London.

Eberhart-Phillips, D. & Martin, R., 1999. Plate interface properties in the northeast Hikurangi subduction zone, New Zeland, from converted seismic waves, *Geophys. Res. Lett.*, **26**(16), 2565–2568.

Ellis, S., Beaumont, C., & Pfiffner, O. A., 1999. Geodynamic models of crustal-scale episodic tectonic accretion and underplating in subduction zones, *J. Geophys. Res.*, **104**(B7), 15169–15190.

Elsasser, W. M., 1971. Seafloor spreading as thermal convection, *J. Geophys. Res.*, **76**, 1101–1112.

England, P. & Wortel, R., 1980. Some consequences of the subduction of young slabs, *Earth Planet. Sci. Lett.*, **47**, 403–415.

England, P. C. & Holland, T. J. B., 1979. Archimeded and Tauren eclogites: the role of buoyancy in the preservation of exotic eclogite blocks, *Earth Planet. Sci. Lett.*, **44**, 287–294.

Faccenna, C., Funiciello, F., Giardini, D., & Lucente, P., 2001. Episodic back-arc extension during restricted mantle convection in the central Mediterrean, *Earth Planet. Sci. Lett.*, **187**, 105–116.

Faccenna, C., Bellier, O., Martinod, J., Piromallo, C., & Regard, V., 2006. Slab detachment beneath eastern Anatolia: A possible cause for the formation of the north Anatolia fault., *Earth Planet. Sci. Lett.*, **242**, 85–97.

Feng, J., Huang, P. Y., & Joseph, D. D., 1996. Dynamic simulaton of sedimentation of solid particles in an Olgg, *J. Non-Newtonian Fluid Mech.*, **187**, 63–88.

Forsyth, D. & Uyeda, S., 1975. On the relative importance of the driving forces of plate, *Geophys. J. Roy. Astron. Soc.*, **43**(1), 163–200.

Freed, A. M. & Burgmann, R., 2004. Evidence of power-law flow in the Mojave desert mantle, *Nature*, **430**, 548–551.

Funiciello, F., Morra, G., Regenauer-Lieb, K., & Giardini, D., 2003. Dynamics of retreating slab: 1. insights from two-dimensional numerical experiments, *J. Geophys. Res.*, **108**(B4), doi:10.1029/2001JB000898.

Gerya, T. V., Stockhert, B., & Perchuck, A. L., 2002. Exhumation of high-pressure metamorphic rocks in a subduction channel: a numerical simulation, *Tectonics*, **21**(6), 227–236.

Giunchi, C., Sabadini, R., Boschi, E., & Gasperini, P., 1996. Dynamic models of subduction: geophysical and geological evidence in the Tyrrhenian Sea, *Geophy. J. Int*, **126**, 555–578.

Govers, R., 1993. *Dynamics of lithospheric extension: A modeling study*, Ph.D. thesis, Utrecht University.

Govers, R. & Wortel, M. J. R., 1993. Initiation of asymmetric extension in continental lithosphere, *Tectonophysics*, **223**, 75–96.

Govers, R. & Wortel, M. J. R., 1995. Extension of stable continental lithosphere and the initiation of lithospheric scale faults, *Tectonics*, **14**(4), 1041–1055.

Govers, R. & Wortel, M. J. R., 2005. Lithosphere tearing at STEP faults: Response to edges of subduction zones, *Earth Planet. Sci. Lett.*, **236**, 505–523.

Hall, R., Gurnis, M., Sdrolias, M., Lavier, L. L., & Muller, R. D., 2003. Catastrophic initiation of subduction following forced convergence across fracture zones, *Earth Planet. Sci. Lett.*, **212**, 15–30.

Hamilton, W. B., 1969. Mesozoic California and the underflow of teh mantle, *Geol. Soc. Am. Bull.*, **80**, 2409–2430.

Hampel, A. & Pfiffner, A., 2006. Relative importance of trenchward upper plate motion and friction along the plate interface for the topographic evolution of subduction-related mountain belts , *Geological Society of London, Special Publications*, **253**, 105–115.

Heuret, A. & Lallemand, S., 2005. Plate motions, slab dynamics and back-arc deformation , *Phys. Earth Planet. Inter.*, **149**, 31–52.

Hilde, T., 1983. Sediment subduction versus accretion around the Pacific, *Tectonophysics*, **99**, 381–397.

Houseman, G. A. & Molnar, P., 1997. Gravitational (Rayleigh-Taylor) instability of a layer with non-linear viscosity and convergence thinning of continental lithosphere, *Geophys. J. Int.*, **128**, 125–150.

Houseman, G. A., McKenzie, D. P., & Molnar, P., 1981. Convective instability of a thickened boundary layer and its relevance for the thermal evolution of continental convergent belts., *J. Geophys. Res.*, **86**(B7), 6115–6132.

Isacks, B. L. & Molnar, P., 1971. Distribution of stresses in the descending lithosphere from a global survey of focal mechanism solutions of mantle earthquakes, *Rev. Geophys. Space Phys.*, **9**, 103–174.

Jacoby, W. R. & Schmeling, H., 1982. On the effects of the lithosphere on mantle convection and evolution, *Phys. Earth Planet. Inter.*, **29**, 305–319.

Jarrard, R. D., 1986. Relation among subduction parameters, *Rev. Geophys.*, **24**(2), 217–284.

Kanamori, H., 1977. The energy realized in great earthquakes, *J. Geophys. Res.*, **82**, 2981–2987.

Kapitzke, U., 1979. Finite element convection models: comparison of shallow and deep mantle convection, and temperatures in the mantle, *J. Geophys. Res.*, **46**, 97–121.

Karato, S. & Wu, P., 1993. Rheology of the upper mantle: a synthesis, *Science*, **260**, 771–778.

Karato, S., Paterson, M. S., & Fitzgerald, J. D., 1986. Rheology of synthetic olivine aggregates: influence of grain size and water, *J. Geophys. Res.*, **91**, 8151–8176.

Karig, D. E. & Sharman, G. F., 1975. Subduction and accretion in trenches, *Geol. Soc. Am. Bull.*, **86**, 377–389.

Kelemen, P. B., Rilling, J. L., Parmentier, E., L., M., & Hacker, B. R., 2004. Thermal structure due to solid-state flow in the mantle wedge beneath arcs, in *Inside the Subduction Factory, Geophysical Monograph*, edited by J. M. Eiler, vol. 138, American Geophysical Union, Washington, DC.

Kerr, A. C. & Tarney, J., 2005. Tectonic evolution of the caribbean and northwestern south america: The case for accretion of two late cretaceous oceanic plateaus, *Geology*, **33**(4), 269–272.

Kincaid, C. & Hall, P. S., 2003. Role of back arc spreading in circulation and melting at subduction zones, *J. Geophys. Res.*, **108**(B5), 1025–1928.

Kneller, E. A., van Keken, P. E., Karato, S., & Park, J., 2005. B-type olivine fabric in the mantle wedge: Insights from high-resolution non-Newtonian subduction zone models, *Earth Planet. Sci. Lett.*, **237**(3-4), 781–797.

Kohlsteldt, D. L. & Zimmerman, M. E., 1996. Rheology of partially molten mantle rocks, *Annu. Rev. Earth Planet. Sci.*, **24**, 41–62.

Kopp, C., Fruehn, J., Flueh, E. R., Reichert, C., Kukowski, N., Bialas, J., & Klaeschen, D., 2000. Structure of the Makran subduction zone from wide-angle and reflection seismic data, *Tectonophysics*, **329**(1-4), 171–191.

Kusky, T. M., Windley, B. F., & Zhai, M.-G., 2007. Tectonic evolution of the North China Block: from orogen to craton to orogen, in *Mesozoic Sub-Continental Lithospheric Thinning Under Eastern Asia*, edited by M.-G. Zhai, B. F. Windley, T. M. Kusky, & Q. R. Meng, vol. 280, pp. 1–34, Geol. Soc. of London Spec. Publ.

Lallemand, S., Schnurle, P., & Malavieille, J., 1994. Coulomb theory applied to accretionary and nonaccretionary wedges: Possible causes for tectonic erosion and/or frontal accretion, *J. Geophys. Res.*, **99**(B6), 12033–12055.

Lallemand, S., Heuret, A., & Boutelier, D., 2005. On the relationships between slab dip, back-arc stress, upper plate absolute motion, and crustal nature in subduction zones, *Geochem. Geophys. Geosyst*, **6**(9), Art. No. Q09006.

Le Pichon, X., 1982. Land-locked oceanic basins and continental collision: The Eastern Mediterranean as a case example., in *In Mountain Building Processes*, edited by K. Hsu, pp. 201–211, Academic Press.

Le Pichon, X., Fournier, M., & Jolivet, L., 1992. Kinematics, topography, shortening and extrusion in the India-Eurasia collision, *Tectonics*, **11**, 1085–1098.

Le Pichon, X., Henry, P., & Lallemand, S., 1993. Accretion and erosion in subduction zones - the role of fluids, *Annu. Rev. Earth Planet. Sci.*, **21**, 307–331.

Lei, J. S. & Zhao, D. P., 2007. Teleseismic evidence for a break-off subducting slab under Eastern Turkey, *Earth Planet. Sci. Lett.*, **257**(1-2), 14–28.

Li, L. & Liao, X., 2002. Slab break-off depth: A slowdown subduction model, *Geophys. Res. Lett.*, **29**(3), doi:10.1029/2001GL013420.

Li, Z. X., 1994. Collision between the north and south China blocks - a crustal-detachment model for suturing in the region east of the Tanlu fault, *Geology*, **22**(8), 739–742.

Liati, A., Gebauer, D., & Wyscoczansky, R., 2002. U-Pb SHRIMP-dating of zircon domains UHP garnet-rich mafic rocks and late pegmatoids in the Rhodope zone (N Greece); evidence for Early Cretaceous crystallisation and Late Cretaceous matamorphism., *Chemical Geology*, **184**, 281–299.

Liou, J. G., Hacker, B. R., & Zhang, R. Y., 2000. Geophysics - Into the forbidden zone, *Science*, **287**(5456), 1215–1216.

Manea, V. & Gurnis, M., 2007. Subduction zone evolution and low viscosity wedges and channels, *Earth Planet. Sci. Lett.*, **doi: 10.1016/j.epsl.2007.08.030**.

McCall, G. J. H., 1997. The geotectonic history of the Makran and adjacent areas of southern Iran, *Journal of Asian Earth Sciences*, **15**(6), 517–531.

Mei, S. & Kohlstedt, D. L., 2000. Influence of water on plastic deformation of olivine aggregates 1. diffusion creep regime, *J. Geophys. Res.*, **105**(B9), 21457–21469.

Melosh, H. J. & Raefsky, A., 1980. The dynamical origin of subduction topography, *Geophys*

J. R. astr. Soc., **60**, 333–354.

Melosh, H. J. & Raefsky, A., 1983. A realistic response of the earth to dip slip earthquakes, *J. Geophys. Res.*, **88**, 515–526.

Mitrovica, J. X. & Forte, A. M., 1997. Radial profile of mantle viscosity: results from the joint inversion of convection and postglacial rebound observables, *J. Geophys. Res.*, **102**, 2751–2769.

Mizukami, A., 1985. An implementation of streamline upwind, Petrov-Galerkin method for triangular elements, *Comp. Meth. Appl. Mech. Eng*, **49**, 357–364.

Molnar, P. & Atwater, T., 1978. Interact spreading and Cordillera tectonics as alternatives related to the age of the subducted oceanic lithosphere, *Earth Planet. Sci. Lett.*, **41**, 330–340.

Oncken, O., Sobolev, S., & Sitller, M., 2003. Seismic imaging of a convergent continental margin and plateau in the central Andes (Andean Continental Research Project 1996 (ANCORP' 96)), *J. Geoph. Res.*, **108**(B7), Art. No. 2328.

Parlak, O., Yilmaz, H., & Boztug, D., 2006. Origin and tectonic significance of the metamorphic sole and isolated dykes of the divrigi ophiolite (sivas, turkey): Evidence for slab break-off prior to ophiolite emplacement, *Turkish Journal of earth sciences*, **15**(1), 25–45.

Patankar, S. V., 1980. Computational Methods In Mechanics and Thermal Sciences, in *Numerical heat transfer and fluid flow*, Hemisphere Publishing Corporation, New York.

Patzig, R., Shapiro, S., Asch, G., Giese, P., & Wigger, P., 2002. Seismogenic plane of the northern Andean Subduction Zone from aftershocks of the Antofagasta (Chile) 1995 earthquake, *Geophys. Res. Lett.*, **29**(8), Art. No. 1264.

Ponko, S. C. & Peacock, S. M., 1995. Thermal modeling of the southern alaska subduction zone - insight into the petrology of the subducting slab and overlying mantle wedge, *J. Geophys. Res.*, **100**(B11), 22117–22128.

Pysklywec, R. N., Beaumont, C., & Fullsack, P., 2000. Modeling the behavior of the continental mantle lithosphere during plate convergence, *Geology*, **28**(7), 655–658.

Ranalli, G., Pellegrini, R., & D'Affizi, S., 2000. Time dependent of negative buoyancy and the subduction of continental lithosphere, *J. Geodyn.*, **30**, 539–555.

Ranero, C. R. & von Huene, R., 2000. Subduction erosion along the Middle America convergent margin, *Nature*, **404**(6779), 748–752.

Regard, V. ad Faccenna, C., Martinod, J., Belier, O., & Thomas, J. C., 2003. From subduction to collision: Control pf deep processes on the evolution of convergent plate boundary, *J. Geophys. Res.*, **108**(B4), doi: 10.1029/2002JB001943.

Renner, J., Stockhert, B., Zerbian, A., K., R., & Rummel, F., 2001. An experimental study into the rheology of synthetic polycrystalline coesite aggregates, *J. Geophys. Res.*, **106**, 19411–19429.

Ristov, H. R., 1996. Wall correction factor for sinking cylinders in fluid, *Physical Review E*, **5**(3), 2808–2813.

Royden, L., 1993. The tectonic expression slab pull at continental convergent margin, *Tectonics*, **12**(2), 303–325.

Ruff, L. J. & Kanamori, H., 1983. Seismic coupling and uncoupling at subduction zones, *Tectonophysics*, **99**, 99–117.

Rupke, L. H., Morgan, J. P., Hort, M., & Connolly, J. A. D., 2004. Serpentine and the sub-

duction zone water cycle, *Earth Planet. Sci. Lett.*, **223**(1-2), 17–34.

Sallares, V. & Ranero, C. R., 2005. Structure and tectonics of the erosional convergent margin off Antofagasta, north Chile (23 degrees 30 ' S), *J. Geophys. Res.*, **110**(B6), 113–136.

Schellart, W. P., Jessel, M. N., & Lister, G. S., 2003. Asymmetric deformation in the back arc region of the Kuril Arc, northwest Pacific: New insights from numerical modeling, *Tectonics*, **22**(5), 1047 doi:10.1029/2002TC001473.

Schmeling, H. & Jacoby, W. R., 1981. On modelling the lithosphere in mantle convection with non linear rheology, *J. Geophys. Res.*, **50**, 89–100.

Schmid, S. M., Pfiffner, O. A., Froitzheim, N., Schonborn, G., & Kissling, E., 1996. Geophysical-geological transect and tectonic evolution of the swiss-italian alps, *Tectonics*, **15**(5), 1036–1064.

Scholl, D. W., Marlow, M. S., & Cooper, A. K., 1977. Sediment subduction and offscraping at Pacific margins, in *Island Arcs, Deep Sea Trench and Back-Arc Basins*, edited by M. Talwani & W. C. Pitman III, vol. 1, pp. 199–210, AGU, Washinton D. C. Maurice Ewing.

Scholz, C. H. & Campos, J., 1995. On the mechanism of the seismic decoupling and back-arc spreading at subduction zone, *J. Geophys. Res.*, **100**, 22103–11115.

Sdrolias, M. & Muller, R. D., 2006. Controls on back-arc basin formation, *Geochem. Geophys. Geosyst*, **7**, Q04016.

Seely, D. R., Vail, P. R., & Walton, G. G., 1974. Trench slope model, in *Geology of continental Margins*, edited by C. A. Burk & C. L. Drake, pp. 249–274, Spinger-Verlag, New York.

Segal, A., 1993. Finite elements methods for advection-diffusion equations, in *Numerical methods for advection diffusion problems, Series in Notes on Numerical Fluid Mechanics*, edited by C. B. Vreugdenhil & B. Koren, pp. 195–214, Braunschweig/Wiesbaden.

Shemenda, A. I., 1993. Subduction of the lithosphere and Back arc dynamics: insights from physical modeling, *J. Geophys. Res.*, **98**(B9), 16167–16185.

Shewchuk, J. R., 2002. Delaunay refinement algorithms for triangular mesh generation, *Computational Geometry-Theory and Applications*, **22**(1-3), 21–74.

Shreve, R. L. & Cloos, M., 1986. Dynamics of sediment subduction, melange formation, and prism accretion, *J. Geophys. Res.*, **91**(B10), 10299–10245.

Smith, D. C., 1984. Coesite in clinopyroxene in the Caledonides and its implications for geodynamics, *Nature*, **310**, 641–644.

Sobouti, F. & Arkani-Hamed, J., 2002. Thermo-mechanical modeling of subduction of continental lithosphere, *Phys. Earth Planet. Inter.*, **131**, 185–203.

Spakman, W., 1990. Tomographic-images of the upper mantle below central-europe and the mediterranean, *Terra Nova*, **2**(6), 542–553.

Stockhert, B., 2002. Stress and deformation in subduction zones- insight from record of exhumed high pressure metamorphic rocks, *Geol. Soc. spec. Publ.*, **200**, 255–274.

Tackley, P. J., 2000. Mantle convection and plate tectonics: Toward an integrated physical and chemical theory, *Science*, **288**, 2002–2007.

Takahashi, N., Kodaira, S., Park, J. O., & Diebold, J., 2003. Heterogeneous structure of western Nankai seismogenic zone deduced by multichannel reflection data and wide-angle seismic data, *Tectonophysics*, **364**(3-4), 167–190.

Tichelaar, B. W. & Ruff, L. J., 1993. Mantle convection and plate tectonics: Toward an

integrated physical and chemical theory, *J. Geophys. Res.*, **98**(B2), 2017–2037.

Toussaint, G., Burov, E., & Jolivet, L., 2004. Continental plate collision: Unstable vs stable dynamics, *Geology*, **32**(1), 33–36.

Tsuru, T., Park, J. O., Miura, S., Kodaira, Y., & Hayashi, T., 2002. Along-arc structural variation of the plate boundary at the Japan Trench margin: Implication of intraplet coupling, *J. Geophys. Res.*, **107**(B12), Art. No 2357.

Uyeda, S. & Kanamori, H., 1979. Back-arc opening and the mode of subduction, *J. Geophys. Res*, **84**(B3), 1049–1061.

van de Zedde, D. M. A. & Wortel, M. J. R., 2001. Shallow slab detachment as a transient source of heat at midlithospheric depths, *Tectonics*, **20**(6), 868–882.

van den Beukel, J., 1992. Some thermomechanical aspects of the subduction of continental lithosphere, *Tectonics*, **11**(2), 316–329.

van Hinsbergen, D. J. J., Hafkenscheid, E., Spakman, W., Meulenkamp, J. E., & Wortel, R., 2005. Nappe stacking resulting from continental lithosphere below subduction of oceanic and greece, *Geology*, **33**(4), 325–328.

van Hunen, J., van den Berg, A., & Vlaar, N. J., 2000. Subduction erosion and basal friction along the sediment-starved convergent margin off Antofagasta, Chile, *Earth Planet. Sci. Lett.*, **182**, 157–169.

van Thienen, P., van den Berg, A. P., de Smet, J. H., van Hunen, J., & Drury, M. R., 2003. Interaction between small-scale mantle diapirs and continental root, *Geochem. Geophys. Geosyst.*, **4**(2), 8301, doi:10.1029/2002GC000338.

Von Huene, R. & Lallemand, S., 1990. Tectonic erosion along the japan and peru convergent margins, *Geol. Soc. Am. Bull.*, **102**(6), 704–720.

Von Huene, R. & Scholl, D. W., 1991. Observations at convergent margins concerning sediment subduction, subduction erosion, and the growth of continental-crust, *Rev. Geophys.*, **29**(3), 279–316.

Von Huene, R. & Scholl, D. W., 1993. The return of sialic material to the mantle indicated by terrigeneous material subducted at convergent margins, *Tectonophysics*, **219**(1-3), 163–175.

Von Huene, R., Ranero, C. R., & Vannucchi, P., 2004. Generic model of subduction erosion, *Geology*, **32**(10), 913–916.

Vos, I. M. A., Bierlein, F. P., & Phillips, D., 2007. The Palaeozoic tectono-metallogenic evolution of the northern Tasman Fold Belt System, Australia: Interplay of subduction rollback and accretion, *Ore Geology Reviews*, **30**(3-4), 277–296.

Walters, K. & Tanner, R. I., 1992. The motion of a sphere through an elastic fluid, in *Transport Process in Bubbles, Drops and Particles*, edited by P. R. Chaabra & D. De Kee, pp. 73–86, Hemisphere.

Westbrook, G. K., Ladd, J. W., Buhl, P., Bangs, N., & Tiley, G. J., 1988. Cross-section of an accretionary wedge - barbados ridge complex, *Geology*, **16**(7), 631.

Whittaker, A., Bott, M. H. P., & Waghorn, G. D., 1992. Stress and plate boundary force associated with subduction, *J. Geophys. Res.*, **97**(B8), 11933–11944.

Willet, S., Beaumont, C., & Fullsack, P., P., 1993. Mechanical model for the tectonics of doubly vergent compressional orogensnt compressional orogens, *Geology*, **21**(4), 371–374.

Wong A Tong, S. Y. M. & Wortel, M. J. R., 1997. Slab detachment in continental collision zones: An analysis of controlling parameters, *Geophys. Res. Lett.*, **24**, 2095–2098.

Wortel, M. J. R. & Spakman, W., 1992. Structure and dynamics of subducted lithosphere in the mediterranean region, *Proc. Kon. Nederlandse Akad. van Wetenschappen*, **95**(3), 325–347.

Wortel, M. J. R. & Spakman, W., 2000. Subduction and slab detachment in the Mediterranean-Carpathian region, *Science*, **290**, 1910–1917.

Yang, J. S., Xu, Z. Q., Dobrzhinetskaya, L. F., Green, H. W., Pei, X. Z., Shi, R. D., Wu, C. L., Wooden, J. L., Zhang, J. X., Wan, Y. S., & Li, H. B., 2003. Discovery of metamorphic diamonds in central china: an indication of a ¿ 4000-km-long zone of deep subduction resulting from multiple continental collisions, *Terra Nova*, **15**(6), 370–379.

Zhong, S. & Gurnis, M., 1994. Controls on trench topography from dynamic models, *J. Geophys. Res.*, **99**(B8), 15683–15695.

Zhong, S. & Gurnis, M., 1994b. Role of plates and temperature-dependent viscosity in phase change dynamics, *J. Geophys. Res.*, **99**(B8), 15903–15917.

Zhong, S., Gurnis, M., & Moresi, L., 1998. Role of faults, nonlinear rheology, and viscosity structure in generating plates from instantaneous mantle flow models, *J. Geophys. Res.*, **103**(B7), 15255–15268.

Summary

In plate tectonics, subduction zones are regions where convergence of lithospheric plates is accommodated: convergent plate boundaries. One plate, generally oceanic, slides underneath the other and moves downwards into the Earth mantle. Along convergent plate boundaries seismic activity and several key geological processes, such as volcanism and mountain building, are concentrated. Well-known examples are western South America (Andes), central America, Japan and Indonesia. Understanding the dynamics of the subduction process in the light of observed features represents a major challenge. The aim of this thesis is to investigate the influence of some specific aspects of subduction zones, in particular the type of plate contact in a subduction zone, on the overall dynamics of the process and their link with surface observations. To this purpose numerical methods (Finite Element methods) are used.

Two fundamental types of the plate contact are investigated: one based on a fault and the other based on a subduction channel. The latter one represents a layer of weak material at the interface of the two plates, similar to the lubricant material in a bearing. Upon further decreasing the channel width, a fault will represent the plate contact. One of the conclusions of this study is that the type of plate contact plays a decisive role in controlling the back-arc extension of the overriding plate. Back-arc spreading is the process in which arcs gradually separate from continents, like for instance in the case of Japan, and Crete.

Subsequently, the influence of the plate contact on continental collision processes has been investigated. Continental collision represents a special type of subduction, where continental material - that is lighter (lower average density) than oceanic lithosphere - attempts to sink into the mantle, often resulting in very high mountains ranges (e.g., the Alps and the Himalayas).

Observations show that continental collision may evolve in different ways, causing a wide range of tectonic responses (e.g., breaking-off of the subducting plate, progressive separation of the crust from the denser lower part of the lithosphere or simply continuation of subduction). The plate contact type, along with the slope of the incoming passive margin and the material properties of the continent, controls whether the incoming crust 1) subducts entirely, 2) separates partially or entirely from the lithospheric mantle, or 3) blocks the trench, likely leading to a break-off of the plate.

Convergent margins are part of one of two categories, accretionary or erosive margins. The first category is characterized by an overriding plate with thick sequences of oceanic and trench rocks that have been off-scraped from the subducting plate during convergence. At erosive margins, the sediments are subducted along with fragments

of the crust removed from the overriding plate. Since the nature of the convergent margin (erosive or accretionary) influences the amount of weak material present at the plate contact, it is an important problem to understand its relation with the nature of the plate contact itself. One of the aims of this thesis is to find differences and similarities between these two main categories and to relate them to the nature of the plate contact.

My research leads me to identify four classes of subduction zones. In class 1, subduction zones are characterized by a plate contact that is largely fault-like with an accretionary margin. In class 2, the subduction zones have plate contacts which are largely channel-type and have an erosive margin. Class 3, where the plate contact is a channel entirely, consists of subduction zones with accretionary margins, with a high sediment supply. The results of the modelling studies described in this thesis account for the specific combination of subduction zone properties within each of the these classes. Subduction zones of class 4, mostly characterized by an erosive convergent margin (northern Chile, Peru, Honshu and Kuril), are more complicated; however, by incorporating regional observations also these can be understood.

The general conclusion of this thesis is that the properties of the plate contact play a decisive role in the subduction process of both oceanic and continental lithosphere. Recognizing the role of the plate contact contributes to understanding the great diversity of the world's subduction zones

Samenvatting (Summary in Dutch)

Mijn onderzoek heeft geleid tot het identificeren van vier klasses van subductiezones: Klasse 1, met subductiezones waarvan het plaatcontact voornamelijk de vorm heeft van een breuk, en met een aangroeiende plaatrand. Klasse 2 subductiezones hebben voornamelijk een subductiekanaal als plaatcontact en een erosieve plaatrand. In klasse 3 subductiezones is het plaatcontact volledig van het kanaal-type, met een aangroeiende plaatrand en een hoge sedimenttoevoer. De resultaten van mijn model-experimenten verklaren de specifieke combinaties van eigenschapppen in ieder van deze drie klasses. Subductiezones in klasse 4, meestal gekarakteriseerd door een erosieve plaatrand (Noord-Chili, Peru, Honshu , Kurielen) zijn complex. Door regionale observaties in de analyse te betrekken zijn ook hun eigenschappen goed te verklaren.

De algehele conclusie van het in dit proefschift beschreven onderzoek is dat het type plaatcontact (breuk of subductiekanaal) een doorslaggevende rol speelt in het subductieproces van oceanische en continentale lithosfeer. Door onderkenning van deze rol is de grote diversiteit in subductiezones beter te verklaren.

Acknowledgments

This thesis would not have been possible without the help, guidance, stimulation, distraction and support offered by many people in the last years of which the following I would like to mention in particular.
First of all, I would like to thank my promotor Prof. Dr. M. J. R. Wortel for his patient guidance, help and enthusiasm, especially during the later stage of my PhD. I also appreciate very much the help offered by my co-promotor Dr. R. Govers that gave me the possibility to start this project and supported my research with pertinent and excellent advises.
I wish to acknowledge the reading committee: S Lallemand, A. M. Marotta, R. Vissers, S.A.P.L. Cloetingh and C. Langereis. Chapter 3 benefited from reviews by Claudio Faccenna and an anonymous reviewer. Thanks to Ueli Meier for proofreading, comments and advises.
Most figures in this thesis were created with p a plotting tool developed by Wim Spakman, Mark de Jonge, Rob Govers and Marteen Remkes. I thank Theo van Zessen and Joop Hoofd for helping me with computer related matters.
A dear world of thanks goes to all my colleagues and friends that largely contributed to the success of my PhD especially Karin, Joost, Maisha, Siska, Mariene, Ebru, Celine, Xavier, Pasha, Bahjat, Peter, Marzieh, Gabriela, Christian, Edith and of course my two paranimfen Thomas and Simona. They have been helpful and a precious support in the moments I needed friends.
I would like to thank my old friends in Italy for always being a close presence. Un particolare ringraziamento va ai miei genitori ed alle mie zie che in questi anni mi hanno sempre sostenuto e mi sono stati vicini. My last thanks go to Ueli who has always been at my side taking care of me.

Curriculum Vitae

30 November 1976	Born in Verona, Italy
1990 - 1995	Secondary school, Liceo Classico Pitagora, Crotone, Italy
1995 - 2001	Master in Physics, Milano University, Italy
2002	Researcher, Dipartimento di Scienze della Terra Ardito Desio, Milano University, Italy
2003 - 2008	Ph.D. Student, Tectonophysics research group, Faculty of Geosciences, Utrecht University, the Netherlands